The Crystallization and Nucleation of Stearic Acid Containing Molecules Under Non-Isothermal Cooling Conditions

A Thesis Submitted to the College of

Graduate Studies and Research

in Partial Fulfillment of the Requirements

for the Degree of Master of Science

in the Department of Food and Bioproduct Sciences

University of Saskatchewan

Saskatoon, SK

By

Ricky Sze Ho Lam

PERMISSION TO USE

In presenting this thesis/dissertation in partial fulfillment of the requirements for a Post graduate degree from the University of Saskatchewan, I agree that the Libraries of this University may make it freely available for inspection. I further agree that permission for copying of this thesis/dissertation in any manner, in whole or in part, for scholarly purposes may be granted by the professor or professors who supervised my thesis, work or, in their absence, by the Head of the Department of the Dean of the College in which my thesis work was done. It is understood that any copying or publication or use of this thesis or parts thereof for financial gain shall not be allowed without my written permission. It is also understood that due recognition shall be given to me and to the University of Saskatchewan in any scholarly use which may be made of any material in my thesis.

Requests for permission to copy or to make other uses of materials in this thesis in whole or part should be addressed to:

Head of the Department of Food and Bioproduct Sciences
University of Saskatchewan
Saskatoon, Saskatchewan S7N 5A8
Canada

ABSTRACT

Crystallization is commonly used in the production of many products such as ice cream, butter and chocolates. Due to the practical limits of the equipment, crystallization in the industry occurs non-isothermally. Currently, there are a limited number of models which can characterize the crystallization behaviour under such conditions. Crystallization under non-isothermal cooling conditions was studied by using molecules with a stearic acid moiety. These stearic acid containing molecules were selected for their different dimensional crystal growths. 12-hydroxystearic acid (12HSA) was selected to represent one-dimensional crystal growth, stearic acid for two-dimensional crystal growth and trihydroxystearin for three-dimensional crystal growth.

In study 1, the modified Avrami model was experimentally validated to model crystallization using non-isothermal cooling conditions. Four techniques were tested which included: small deformation rheology, differential scanning calorimetry, polarized light microscopy and Fourier transform infrared spectroscopy (FT-IR). The experimental validation of the model was done by accurately fitting the parameters of the modified Avrami model; such as induction time, maximal phase change and the Avrami exponent; to the data. FT-IR was the most accurate method because the data collected fitted well to the modified Avrami model. The Avrami exponent obtained from FT-IR was the only technique to be sensitive to both the mode of nucleation as well as the dimensionality of crystal growth. By using the modified Avrami model to characterize crystallization under non-isothermal cooling conditions, the apparent rate constant obtained from the model gave further insights to the kinetics of crystallization under these conditions.

Study 2 investigated the nature of crystallographic mismatches in 12HSA fibres which causes branching due to the imperfect incorporation of 12HSA molecules into the crystal lattice. FT-IR was used to monitor the changes during crystallization in the 1700 cm^{-1} and 3200 cm^{-1} peaks which corresponded to the dimerization of carboxylic acid monomers and the formation of non-specific hydrogen bonding, respectively. When FT-IR data was fitted to the modified Avrami model, the rate constants obtained increased linearly with the cooling rate for hydrogen bonding while the dimerization of carboxylic

acid monomers plateaued at cooling rates above 5 °C/min. Therefore at cooling rates above 5 °C/min, 12HSA does not effectively dimerize when incorporating into the crystal lattice which causes crystal imperfections leading to branching in 12HSA fibres.

In study 3, the activation energy for nucleation under non-isothermal cooling conditions was determined using a statistical method. The activation energies for stearic acid, 12HSA, trihydroxystearin and triglycerides were 1.52 kJ/mol, 5.40 kJ/mol (Rogers & Marangoni, 2009), 7.87 kJ/mol and 24.8 kJ/mol (Marangoni, Tang, & Singh, 2006); respectively. The activation energy for nucleation for a molecule is partially affected by its polarity relative to the solvent such that an increase in polarity would result in a decrease in activation energy. However, this was not always observed as the activation energy for stearic acid was less than that for 12HSA. Since the polarity of the molecule does not fully explain the activation energy, a specific interaction was used to account for the larger activation energy observed in 12HSA. The specific interaction describes how molecules are arranged in a nucleus and its ability to hide the polar groups away from the crystal-solvent interface. When the polar groups were not effectively hidden, an increase in the activation energy for nucleation was observed.

ACKNOWLEDGEMENTS

This thesis is dedicated to my family and especially my parents (Danny Kam Wah Lam and Jennifer Kam Woon Lam) for their love, hard work, support and guidance over me throughout my life.

My research would not have been possible without the continual guidance and mentoring from my supervisor Dr. Michael A. Rogers. I would like to thank him for his mentorship and friendship which began while I was an undergraduate student. I would like to thank him also for his constant support and encouragement throughout my thesis and his advice has been invaluable to me. I would also like to thank my committee members Drs. Michael Nickerson, Takuji Tanaka, Phyllis Shand, Robert Tyler and my external Ian Burgess.

This body of work was done, in part, at the Canadian Light Source (CLS) Mid-IR Beamline (beamline 01 B1-01, Canadian Light Source, Saskatoon, SK). I would not have been able to accomplish this work without the friendly, helpful guidance of the staff at the CLS. Furthermore, I would like to give special thanks to Ferenc Borondics, Tor Pedersen, Tim May, and Luca Quaroni for their patience and help throughout the time spent on the beamline.

I would like to thank the professors and staff in the Department of Food and Bioproduct Sciences for their friendship, support and guidance throughout my studies.

I am grateful for the financial assistance provided by the University of Saskatchewan and the NSERC Discovery Grant which funded my research.

I would also like to thank my friends both within the department and those I have come to know in Saskatoon for their friendship and support which had made my studies such an enjoyable time.

TABLE OF CONTENTS

PERMISSION TO USE i
ABSTRACT ii
ACKNOWLEDGEMENTS iv
TABLE OF CONTENTS v
LIST OF TABLES viii
LIST OF FIGURES ix
LIST OF ABBREVIATIONS xii
1. Introduction 1
2. Literature Review 4
2.1 Crystallization 4
2.2 The Structure of Fats 5
2.3 Health Implications of Diets High in Saturated and *Trans*- Fats 6
2.4 The Use of Organogelators to Replace Fats 8
2.5 Stearic Acid Containing Molecules with Different Dimensionalities of Crystal Growth 8
2.5.1 Trihydroxystearin and 12-Hydroxystearic Acid 9
2.5.2 Stearic Acid 10
2.6 The Crystallization Process 11
2.6.1 Supercooling 11
2.6.2 Nucleation 12
2.6.3 Crystal Growth 14
2.7 The Avrami Model 14
2.8 The Differences between Cooling Conditions Used to Crystallize Products 16
2.8.1 Isothermal Cooling Conditions 16
2.8.2 Non-Isothermal Cooling 16
3. Study 1: Experimental Validation of the Modified Avrami Model for Non-Isothermal Crystallization Conditions[1] 20
3.1 Abstract 20
3.2 Introduction 20
3.3 Derivation of the Modified Avrami Model from Fick's First Law of Diffusion 24

3.4 Materials and Methods 27
3.4.1 Synchrotron Fourier Transform-Infrared Spectroscopy (FT-IR) 27
3.4.2 Differential Scanning Calorimetry 29
3.4.3 Small Deformation Rheology 30
3.4.4 Polarized Light Microscopy 30
3.4.5 Fitting the Modified Avrami Model 31
3.5 Results and Discussion 31
3.6 Conclusions 44
3.7 Study 1 in context of this thesis 45
4. Study 2: A Molecular insight into the nature of crystallographic mismatches in self-assembled fibrillar networks under non-isothermal crystallization conditions.[2] 46
4.1 Abstract 46
4.2 Introduction 46
Fundamental research on molecular gels, capable of self-assembling into fibrillar 46
4.3 Methods 50
4.3.1 Sample Preparation 50
4.3.2 Polarized Light Microscopy 50
4.3.3 Small deformation Rheology 50
4.3.4 Synchrotron Fourier Transform Infrared Spectroscopy 51
4.4 Results and Discussion 51
4.5 Conclusions 60
4.6 Study 2 in context of this thesis 60
5. Study 3: Activation Energy of Crystallization for Stearic Acid Containing Molecules under Non-Isothermal Cooling Conditions 61
5.1 Abstract 61
5.2 Introduction 62
5.3 Materials and Methods 66
5.3.1 Polarized Light Microscopy 66
5.3.2 Differential Scanning Calorimetry 67
5.4 Results and Discussion 67
5.5 Conclusion 77

5.6 Study 3 in context of this thesis.....78
6. General Discussion 79
7. Conclusions.....83
8. References.....86

LIST OF TABLES

Table 2.1: Values for the Avrami exponent, n, for different types of nucleation and crystal growth (Taken from Sharples, 1966)…….. 16

Table 3.1: Possible forms of the Avrami model for the different modes of nucleation and their associated dimensionality of crystal growth (Marangoni, 2005a)….. 28

Table 4.1: Dependence of the average fractal dimension and the standard deviation using non-isothermal cooling rates determined using small deformation rheology… 56

Table 5.1: Demixing entropies and the enthalpy associated with the phase transition for 12-hydroxystearic acid (12HSA), stearic acid (SA) and trihydroxystearin (THS)…….. 76

LIST OF FIGURES

Figure 2.1: The structures which form a fat crystal networks (Taken from Marangoni and Tang, 2008) ……. 7

Figure 2.2: Molecular structures of stearic acid (A), D-12-hydroxystearic acid (B) and trihydroxystearin (glyceryl tri-D-12-hydroxystearate) (C)……...……. 10

Figure 2.3: Simulated Gibbs energy as a function of temperature for the liquid (black line) and solid (grey line) phase of a system (Adopted from Walstra, 2003) … 12

Figure 2.4: Temperature and crystallization profiles for materials crystallizing under isothermal (A), near-isothermal (B) and non-isothermal (C) conditions (Taken from Marangoni, *et al.*, 2006) ……..... 18

Figure 3.1: Polarized light micrographs of 1D fibres (12-hydroxystearic acid) (A), 2D platelets (stearic acid) (B), and 3D spherulite (trihydroxystearin) (C) with their respective axes of crystal growth represented by x, y and z. Bar = 5 μm …….. 21

Figure 3.2: A sampling of FT-IR spectrums of 12HSA (A), stearic acid (B) and trihydroxystearin (C) cooled at 1 °C/min from 90 °C to 30 °C and their respective area under the peak plotted over time fitted to the modified Avrami model (D, E, and F respectively). The filled and open in data points for Figures D and F represent the carboxyl peak (1710 cm^{-1}) and hydroxyl peak (3200 cm^{-1}) respectively …… 33

Figure 3.3: A sampling of DSC thermograms of 12HSA (A), stearic acid (B) and trihydroxystearin (C) cooled at different rates and a plot of their respective continuous integration for the different cooling rates fitted to the modified Avrami model (D-F respectively) ……..……. 34

Figure 3.4: A sampling of the storage modulus obtained for 12HSA (A), stearic acid (B) and trihydroxystearin (C) collected under different cooling rates and fitted to the modified Avrami model ……... 35

Figure 3.5: A sampling of PLM characteristic lengths corrected for their dimensionality of crystal growth for 12HSA 1-D fibres (A), stearic acid 2-D platelets (B) and trihydroxystearin 3-D spheres (C) and fitted to the modified Avrami model 36

Figure 3.6: Avrami exponents (n) calculated from the fits of the experimentally observed

data to the modified Avrami model for FT-IR (A, E and I), PLM (B, F, and J), DSC (C, G, and K) and rheology (D, H and L) for 12HSA (A-D), stearic acid (E-H) and trihydroxystearin (I-L) ……. 38

Figure 3.7: The induction times (x_0) of the fitted data for 12HSA (A), stearic acid (B) and trihydroxystearin (C) ……..…… 40

Figure 3.8: The maximal measure of the change in the phase volume (Y_{max}) as a function of cooling rate for the experimentally observed verses the fitted data to the modified Avrami model for FT-IR (A, E and I), PLM (B, F, and J), DSC (C, G, and K) and rheology (D, H and L) for 12HSA (A-D), stearic acid (E-H) and trihydroxystearin (I-L) ……..…. 42

Figure 3.9: Apparent rate constants (k_{app}) obtained from the experimental fits of the data to the modified Avrami model for FT-IR (A, C, and E) and PLM (B, D, and F) for 12HSA (A-B), stearic acid (C-D) and trihydroxystearin (E-F) ……..... 43

Figure 4.1: Nucleation and crystal growth mechanism using the crystallographic mismatch theory (Adapted from Li, *et al.*, 2009) ……..... 49

Figure 4.2: Two and a half (wt%) 12HSA in mineral oil organogels at 30°C cooled at 1 °C/min (A), 4 °C/min (B), 7 °C/min (C) and 20 °C/min (D). Magnification bar = 100 μm ……..… 52

Figure 4.3: Correlation length of 2.5 wt% 12HSA fibres in mineral oil measured from mineral oil measured from the micrographs obtained at 30 °C after they had been cooled from 90 °C at varying cooling rates ……... 53

Figure 4.4: The evolution of G* as a function of time during gelation under non-isothermal conditions for slow cooling rates (A) and fast cooling rates (B). The dependence of $\ln[-\ln(1-X_{cr})]$ on $\ln(t-t_g)$ to determine the fractal values under different non-isothermal cooling profiles (C and D). Data was shifted to prevent overlap (C) ……. 55

Figure 4.5: Differential FT-IR spectra of 12HSA assembly during slow cooling at 1 °C/min and was collected from 90 °C to 30 °C over a 60 min period (A) and fast cooling at 10°C/min from 90 to 30°C over a 6 min period (B) non-isothermal cooling profiles. Integration of the FT-IR spectra (C and D) to determine the area under the spectra features of interest (Filled symbols represent absorbance at

3200 cm^{-1} and open symbols represent the absorbance at 1700 cm^{-1}). Avrami constants are determined by fitting the integrated area verses time to obtain maximum signal (E), apparent rate constant (F), induction time (G) and dimensionality of growth (H) ……. 58

Figure 5.1: Brightfield micrographs of 12HSA (A-C), polarized light micrographs of stearic acid (D-F) and trihydroxystearin (G-I) in mineral oil cooled at 1 °C/min ……..…….. 69

Figure 5.2: Brightfield micrographs of 12HSA (A-C), polarized light micrographs of stearic acid (D-F) and trihydroxystearin (G-I) in mineral oil cooled at 10 °C/min ……... 70

Figure 5.3: Number of nuclei on the corresponding light micrographs as the sample is non-isothermally cooled for 2.5% 12HSA (A-B), 2.5% stearic acid (C-D) and 2.5% trihydroxystearin (E-F) in mineral oil where time zero is the maximum cooling temperature ……...…..……..…. 72

Figure 5.4: The rate of nucleation determined from the derivative of Figure 3 for 2.5% 12HSA (A-B), 2.5% stearic acid (C-D) and 2.5% trihydroxystearin (E-F) ….... 72

Figure 5.5: The dependence of the relative nucleation rate (J/J_{max}) verses the supercooling-time exposure (β) for 2.5% 12HSA (A), 2.5% stearic acid (C) and 2.5% trihydroxystearin (E) in mineral oil, and the dependence of the relative nucleation rate (J/J_{max}) versus the cooling rate for 2.5% 12HSA (B), 2.5% stearic acid (D) and 2.5% trihydroxystearin (F) in mineral oil ……...….... 73

Figure 5.6: Molecular dimers of 12-hydroxystearic acid (A) and stearic acid (B) …..... 74

Figure 5.7: The enthalpy for crystallization of 12-hydroxystearic acid (12HSA) (left axis), stearic acid (SA) (right axis) and trihydroxystearin (THS) (right axis) 75

LIST OF ABBREVIATIONS

1-D	One dimensional
2-D	Two dimensional
3-D	Three dimensional
12HSA	12-hydroxystearic acid
A	Pre-exponential factor
A_d	Area of diffusion
β	Supercooling-time-trajectory parameter
γ_i	Interfacial tension
c	Concentration of supersaturated material
c*	Equilibrium saturation concentration of the material per unit volume
C	Concentration of soluble material
C_p	Specific heat
CMB	Crystallographic mismatch branching
$\Delta C/\Delta x$	Change in concentration of soluble material across a thickness
δ	Crystal-melt interfacial tension
D	Diffusion coefficient
D_f	Fractal dimension
DSC	Differential scanning calorimeter
E_a	Activation Energy
FEM-TTT	Finite element method using the isothermal time-temperature-transformation
FT-IR	Fourier transformed infrared spectroscopy
g	Linear growth rate
G′	Storage modulus
G*	Modulus
G_0*	Initial modulus
G*(max)	Maximum modulus
ΔG	Gibbs energy
ΔG_B	Crystallographic mismatch nucleation barrier
ΔG_S	The positive Gibbs energy associated with the formation of a surface

ΔG_V	The negative Gibbs energy associated with a forming volume
ΔG_n	Gibbs energy for the formation of a spherical nucleus
ΔG^*	The Gibbs energy for the critical radius
h	Non-propagating surface of a growing plate
ΔH	Enthalpy for the phase transition
ΔH_{fus}	Change in enthalpy per unit volume
HDL	High density lipoproteins
j_c	Nucleation rate
J_c	Number of stable nuclei formed over a time per unit volume
J	Nucleation rate
J_{max}	Maximum nucleation rate
κ	Boltzmann's constant
κ_s	Crystalline surface
k	Rate change in phase volume
k_n	Rate constant for nucleation
k^0	Growth rate constant
k_{app}	Apparent rate constant
k_g	Rate constant for crystal growth in mass
k_n	Rate constant for nucleation kinetics
l	Dimension of the growing plate
LDL	Low density lipoproteins
LVR	Linear viscoelastic region
$\Delta\mu$	Chemical potential difference between the liquid and the solid
m_s	Total mass of solids present in the system at a particular time
MW	Molecular weight
n	Avrami exponent
N	Number of crystals
N*	Number of molecules capable of overcoming the energy barrier for nucleation
N_T	Total concentration of molecules in a system

$p(x)$	The probability density function that describes the frequency distribution of a particular event
pdf	Probability density function
PLM	Polarized light microscopy
$\partial Q/\partial t$	Moles of material crystallized as a function of time
Q	Moles of Material
Q_m	Heat removed
r	Radius of a nucleus
r_c	Critical radius
r_{fibre}	Radius of a growing fibre
r_{sphere}	Radius of a growing sphere
R	Ideal gas constant
R^2	Coefficient of determination
ΔS	Demixing entropy
τ	Supercooling
t	Time
t_0	Induction time
t_c	Time associated with the crystallization temperature
t_g	Gelation time
T	Absolute temperature
TTT	Isothermal time-temperature-transformation diagram
ΔT	Difference in the melted to the sample temperature (*i.e.* supercooling)
ΔT_c	Difference between the melting and crystallization temperature (T_m-T_c)
T_c	Crystallization temperature
T_g	Gelation temperature
T_m	Melting temperature
T_s	Set temperature
T*	Equilibrium temperature
ρ	Number of crystals per unit volume
ϕ	Cooling rate
v	rate of reaction

V_m^s	Molar volume of a solid
V_t	Volume of a system
ξ	Correlation length
x	Time
Δx_d	Diffusional distance
x_0	Induction time
$X_{cr}(t)$	Crystallization at time t
Y	Measure of the phase change
Y_c	Mass of a crystal
Y_{max}	Maximal phase change
Y_s	Mass of total solids

1. Introduction

Crystallization is a process that is utilized in the production of many products, such as ice cream, butter and chocolates, and is critical in determining the stability, textural and rheological properties of a product. Crystallization and nucleation are traditionally studied under isothermal cooling conditions, yet under industrial settings, non-isothermal cooling conditions occur whereby the temperature changes with time, which is commonly defined by a cooling rate. Crystallization and nucleation under non-isothermal cooling conditions requires its own models to characterize these processes which are paramount to the industry.

Of the many foods which utilize crystallization, fat crystal networks are important because they provide structure to high-fat foods such as butter and chocolate. Fat crystal networks are comprised of triglycerides, which are composed of fatty acids and glycerol. These triglycerides form lamellar structures which aggregate into crystallites. Crystallites interact to form flocs. Weak links are formed between flocs until the system becomes a continuous three-dimensional network. There are negative health implications associated with the consumption of fat crystal networks because they contain saturated and *trans* fatty acids (Aro, Jauhiainen, Partanen, Salminen, & Mutanen, 1997). Therefore, alternatives such as unsaturated oils gelled by a low-dimensional gelator, are being sought to replace traditional fat crystal networks (Pernetti, van Malssen, Flöter, & Bot, 2007; Rogers, 2009). Furthermore, as these low-dimensional products enter the market, understanding how changes in the processing conditions affect crystallization and the resulting product from an industrial perspective is imperative.

The objective of this body of work was to investigate the nature of nucleation and crystallization under non-isothermal cooling conditions. This was accomplished by studying the nucleation and crystallization behaviour of molecules containing a stearic

acid moiety but differ in their dimensionality of crystal growth. 12-hydroxystearic acid (12HSA) represented 1-D fibres (Huang & Weiss, 2007; Iwanaga, Sumizawa, Miyazaki, & Kakemi, 2010; Li, Wang, Liu, & Pan, 2009; Rogers & Marangoni, 2008, 2009; Rogers, Wright, & Marangoni, 2009a; Tachiban & Kambara, 1968), stearic acid represented 2-D platelets (Gandolfo, Bot, & Flöter, 2004; Schaink, van Malssen, Morgado-Alves, Kalnin, & van der Linden, 2007; Swamy, Prasad, & Raju, 1985) and trihydroxystearin represented 3-D spheres (Hackeng, de Bruijn, Douw, & van Dieijen Visser, 2000). Three experimental designs were used to achieve our objectives:

1) To validate the modified Avrami model for crystallization under non-isothermal cooling conditions using four techniques.
2) To investigate the nature of crystallographic mismatches in 12HSA.
3) To determine of the role of molecular structure on the corresponding activation energy for nucleation under non-isothermal cooling conditions.

It was hypothesized that the modified Avrami model may be used as a tool to model crystallization under non-isothermal cooling conditions. The modified Avrami model takes the following form:

$$Y = Y_{max}(1 - e^{-k_{app}(t-t_0)^n}) \qquad \text{(eq. 1.1)}$$

where Y is the measure of the phase change, Y_{max} is the maximum phase change detected, k_{app} is the apparent rate constant, t is time, t_0 is the induction time and n is the Avrami exponent (Rogers & Marangoni, 2008, 2009).

It was hypothesized, for objective two, that the rate of hydrogen bond formation would be greatly diminished under high cooling rates. This hypothesis was based on the knowledge that non-specific hydrogen bonding of the hydroxyl group in 12HSA was responsible for longitudinal fibre growth (Suzuki, Nakajima, Yumoto, Kimura, Shirai, & Hanabusa, 2003). This was examined by using Fourier-transform infrared spectroscopy to determine the rate of non-specific hydrogen bonding at 3200 cm^{-1} and comparing that to carboxylic acid dimerization at 1700 cm^{-1}.

It was hypothesized for objective three that the activation energy for crystallization is dependent on the relative polarity of the molecule with respect to the solvent such that an increase in polarity will result in a decrease in the activation energy. It was also predicted that the ascending order of activation energies obtained under non-isothermal cooling will be 12HSA, stearic acid, trihydroxystearin and triglycerides. To examine this hypothesis, a statistical approach was used to determine the activation energy for nucleation under non-isothermal cooling conditions for stearic acid and trihydroxystearin and compared to previously reported results for 12HSA and triglycerides (Marangoni, Aurand, Martini, & Ollivon, 2006; Marangoni, Tang, & Singh, 2006; Rogers & Marangoni, 2008, 2009).

2. Literature Review

2.1 Crystallization

Crystallization is the process by which a material undergoes a phase transition from a liquid to a solid. This is an important process as it occurs in numerous foods containing water, carbohydrates and lipids. The resulting crystalline structure affects the physical properties of a product such as texture, mouth feel, rheology and stability. These physical properties are due, in part, to the morphology and size of the crystals. Furthermore, different crystal morphologies are desirable in different products such as smooth crystals in ice cream and jagged crystals in popsicles (Hartel, 2001). Small crystals are desired in frozen foods because large crystals rupture cell membranes causing water loss in the thawed product (Hartel, 2001). The size and morphology of crystals in a food product are primarily due to the formulation, processing conditions and thermal history (Hartel, 2001).

Fat crystal networks are important due to their ability to provide structure in foods rich in lipids. These mixtures of lipids may include phospholipids, monoglycerides, diglycerides and triglycerides. The physical properties of fat crystal networks are primarily attributed to their triglyceride composition, crystal packing, crystal size, polymorphism and spatial distribution of mass (McClements & Decker, 2008). Triglyceride composition affects the physical properties, including melting profile, hardness and mouth feel (McClements & Decker, 2008). Butter, for example, has many different classes of triglycerides which possess a wide range of melting temperatures (McClements & Decker, 2008). This wide range of melting temperatures gives butter a gradual melting profile (McClements & Decker, 2008). The crystal packing, or polymorphism, of a fat affects not only the hardness and melting profile but also its stability (McClements & Decker, 2008).

Monotropic polymorphism is the ability for a molecule to be able to take on several different molecular packings (Hartel, 2001; Walstra, 2003). In triglycerides, the common molecular packings are hexagonal, orthorhombic and triclinic which are designated as α, β′ and β respectively (McClements & Decker, 2008). Though these three are the most common polymorphs, foods like chocolate have more than three polymorphisms. Polymorphism is determined by the molecular structure and composition of the lipids present (McClements & Decker, 2008). Polymorphs have differing thermodynamic stabilities where the α-form has the lowest stability followed by the β′ and the β-forms (McClements & Decker, 2008; Walstra, 2003). Polymorphism is important because it affects the mouth feel and the rheological properties of fats (McClements & Decker, 2008).

2.2 The Structure of Fats

Fats are semi-solid materials which exhibits viscoelasticity. Viscoelasticity is the ability for a material to have both viscous and elastic properties whereby a material deforms under stress and partially recovers when the stress is removed. The viscoelastic properties of fat contribute to its texture which includes a number of physical properties such as brittleness, hardness, softness, and spreadability (deMan & deMan, 2002). The elastic properties of fats are dependent on the fat crystals and their associated network (deMan & deMan, 2002).

At the smallest scale, fats are comprised of triglycerides packed into a crystalline conformation forming a lamellar structure (Figure 2.1) (deMan & deMan, 2002). These lamellar structures are stacked to form a domain (Marangoni & Tang, 2008). Multiple domains aggregate to form a single crystallite (Marangoni & Tang, 2008). Multiple crystallites aggregate and interact to form flocs (Marangoni & Tang, 2008). Flocs interact to form weak links with each other until a continuous network is formed (Marangoni & Tang, 2008). It is these weak links, which are postulated as bonds that are easily disturbed and reformed, between crystal flocs which affect the textural properties of a fat (deMan & deMan, 2002). When fat is deformed, the weak links are easily disrupted and then reformed when the fat is left undisturbed (deMan & deMan, 2002). The elastic properties of fats are affected by the spatial distribution of flocs and

their associated weak links (Marangoni & Tang, 2008). The structures found in a fat crystal network are depicted in figure 2.1.

2.3 Health Implications of Diets High in Saturated and *Trans*- Fats

Though triglycerides composed of saturated and *trans*- fatty acids are responsible for providing structure to a fat crystal network, the consumption of these fatty acids have negative health implications. Diets high in these fatty acids cause an increase in low density lipoprotein (LDL) whereas diets high in *trans*- fats also reduces the high density lipoproteins (HDLs), the heart healthy fat, in the body (Aro *et al.*, 1997). By elevating LDL to total cholesterol ratios, there is an associated increase risk for contracting cardiovascular diseases such as atherosclerosis (Ross, 1999). Even though research demonstrate the dangers of having an elevated LDL level due to diets high in saturate fats, it is important to note that not all saturated fatty acids have deleterious health effects (Livesey, 2000). Stearic acid is a fatty acid which is non-detrimental as it is not known to alter LDL and HDL levels (Aro *et al.*, 1997). Stearic acid is non-detrimental due to its reduced digestibility and is therefore considered a neutral lipid (Livesey, 2000).

One potential detrimental health effect of consuming diets high in saturated and *trans*- fats is the development of metabolic syndrome (Roche, 2005). People with at least two of the following risk factors are considered to have metabolic syndrome according to the World Health Organization: impaired insulin sensitivity, dyslipidaemia, abdominal obesity and hypertension (Isomaa, Almgren, Tuomi, Forsen, Lahti, Nissen, Taskinen, & Groop, 2001). Patients with metabolic syndrome are at high risk for developing cardiovascular diseases (Isomaa *et al.*, 2001). Yet, the deleterious effects of saturated and *trans*- fats are reversible by replacing them with polyunsaturated fats (Roche, 2005). It is estimated that a replacement of 5% daily saturated and *trans*- fats, can cause a reduction of 22 to 37% associated risk of contracting cardiovascular disease (Roche, 2005). Due to the associated health risks, there is increasing pressure on food companies to find substitutes for saturated and *trans*- fats in foods. Unfortunately, it is

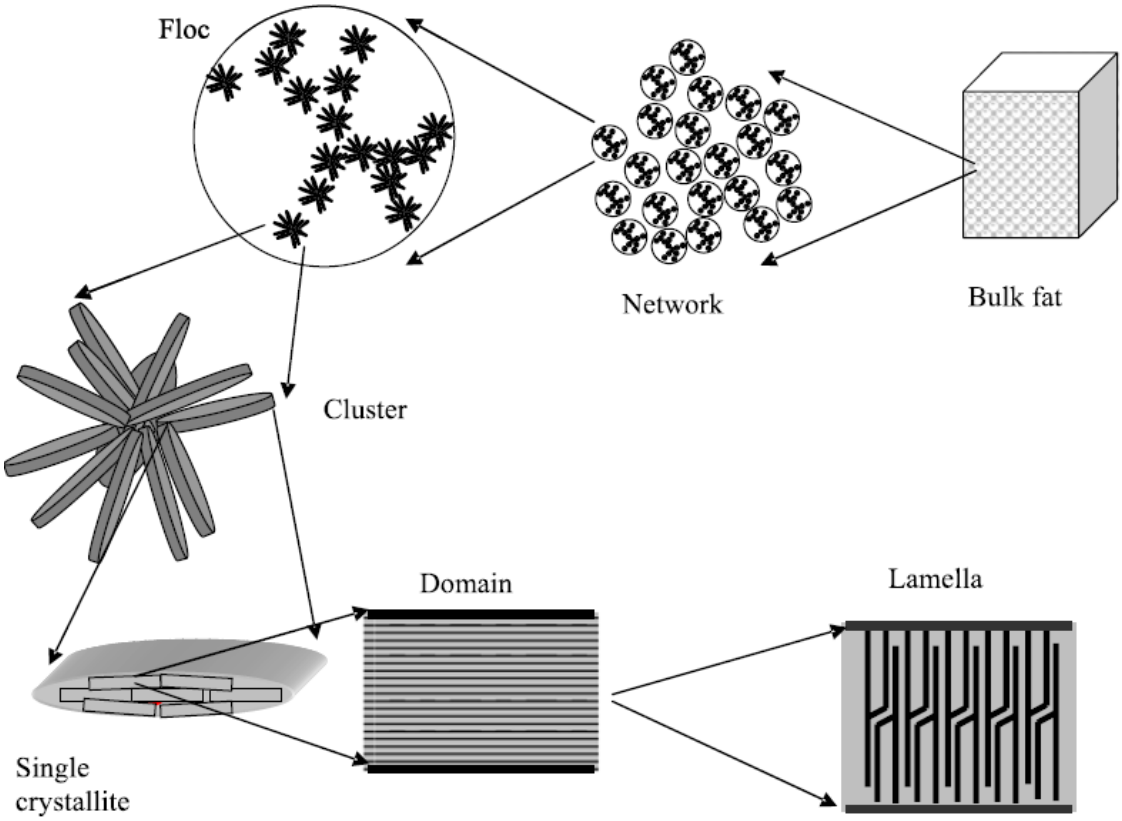

Figure 2.1: The structures which form a fat crystal networks (Taken from Marangoni and Tang, 2008).

these saturated and *trans*- fats which provide the elastic structure in products such as ice cream, cheese, butter, lard, *etc*. (Rogers, 2009). Therefore saturated and *trans*- fats are both required and desirable in food products such that removing them will affect the properties of the product (Rogers, 2009). One potential alternative to saturated and *trans*- fats is the use of organogelators to structure oils.

2.4 The Use of Organogelators to Replace Fats

Organogelators are an attractive alternative due to their ability to structure oils at low concentrations. These structures typically take on low-dimensional structure such as liquid-crystalline, inverse bilayers forming rod shaped tubules, crystal platelets, and self-assembled fibrillar networks (Rogers, 2009). Finding organogelators has been quite difficult and often serendipitous (Rogers, 2009). One major hurdle for the use of organogelators in food is the ability to mimic the viscoelastic properties of fat crystal networks (Pernetti *et al.*, 2007). In addition, the high cost of making these gelators and the lack of food grade compounds have inhibited the use of organogelators in foods (Rogers, 2009). Thus far, there are a variety of compounds that have been found to structure oils (*i.e.* monoglycerides, sorbitan monostearate, lecithin, candelilla wax, fatty alcohols, fatty acids and hydroxystearic acid) which crystallize into low-dimensional crystal structures.

2.5 Stearic Acid Containing Molecules with Different Dimensionalities of Crystal Growth

12HSA, stearic acid and trihydroxystearin are stearic acid containing molecules with different dimensionalities of crystal growth. 12HSA form one-dimensional self-assembled fibres (Huang & Weiss, 2007; Iwanaga *et al.*, 2010; Li *et al.*, 2009; Rogers & Marangoni, 2008, 2009; Rogers *et al.*, 2009a; Tachiban & Kambara, 1968). Stearic acid (SA) form two-dimensional platelets (Gandolfo *et al.*, 2004; Schaink *et al.*, 2007; Swamy *et al.*, 1985). Trihydroxystearin form three dimensional spherulites (Hackeng *et al.*, 2000).

2.5.1 Trihydroxystearin and 12-Hydroxystearic Acid

12-hydroxystearic acid (12HSA) is a well-studied organogelator which self-assembles into a one-dimensional fibrillar network (Huang & Weiss, 2007; Huo, dai, zhang, Kong, Fang, Guo, Liu, Hu, Pan, & Wang, 2008; Rogers & Marangoni, 2008, 2009; Rogers, Wright, & Marangoni, 2008a). Though 12HSA is not food grade, it can be used as an ideal model system to study the effects of processing conditions on the properties of the network (Rogers, 2009). Furthermore, 12HSA is an efficient gelator, because it can gel oil with a concentration as low as 0.3% (w/w) (Rogers & Marangoni, 2008). 12HSA is also known to gel various organic solvents which enable it as a suitable model system for studying nucleation and crystallization behaviour (Rogers & Marangoni, 2009).

Early studies on 12HSA (Figure 2.2B) and trihydroxystearin (Figure 2.2C) attempted to incorporate these compounds into peanut butter formulations to prevent syneresis (Elliger, Dunlap, & Guadagni, 1972). Since then, the use of 12HSA in foods has been banned due to its laxative properties (Johnson, 2000). 12HSA and trihydroxystearin have since found its way into cosmetics (Johnson, 2000) and lubricant formulations (Boner, 1958). Trihydroxystearin and 12HSA may be used at a concentration of up to 5% in cosmetics because they do not cause skin irritations (Johnson, 2000).

Trihydroxystearin and 12HSA are both products derived from castor oil (Elliger *et al.*, 1972; Maskaev, Man'Kovskaya, Lend'el, Fedorvskii, Simurova, & Terent'eva, 1971). Trihydroxystearin is produced by hydrogenating triricinolein which is found in castor oil (Maskaev *et al.*, 1971). To produce 12HSA, trihydroxystearin is saponified to release the fatty acids by using caustic soda (Maskaev *et al.*, 1971). The saponified fatty acids are neutralized by an acid and washed in water to produce 12HSA (Maskaev *et al.*, 1971).

The conditions used during hydrogenation are critical to ensure the complete conversion of triricinolein to trihydroxystearin (Maskaev *et al.*, 1971). Slight variations in the processing conditions could cause an unwanted dehydration reaction and a reduction of a hydroxyl group which produces stearic acid (Maskaev *et al.*, 1971).

Furthermore, to ensure that no alternative products are made, high purity castor oil is required for the production of these products (Maskaev *et al.*, 1971).

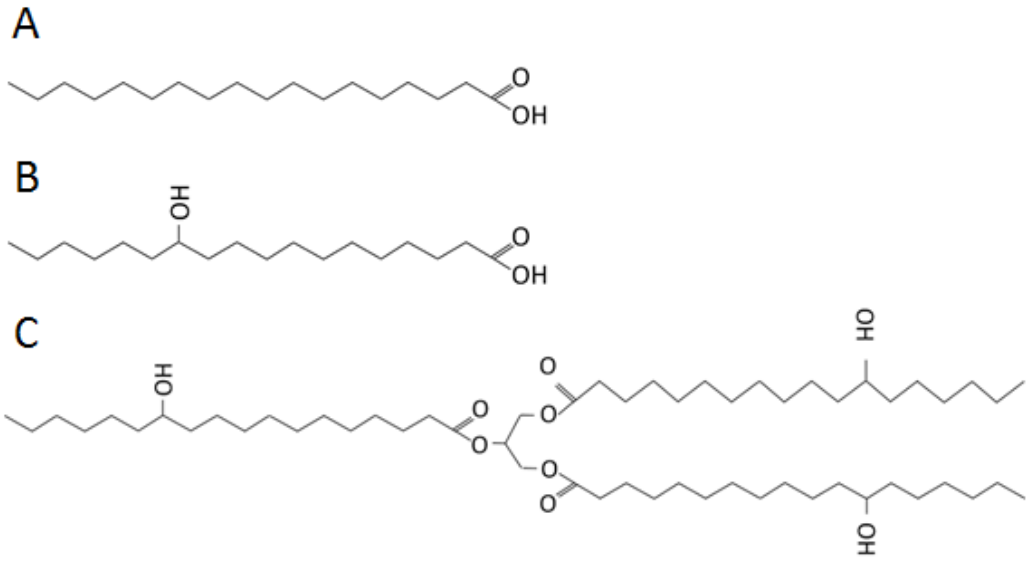

Figure 2.2: Molecular structures of stearic acid (A), D-12-hydroxystearic acid (B) and trihydroxystearin (glyceryl tri-D-12-hydroxystearate) (C).

2.5.2 Stearic Acid

Stearic acid (Figure 2.2A) is a fatty acid found in many vegetable oils (Fernandez-Moya, Martinez-Force, & Garces, 2005) and animal fats. Like 12HSA, stearic acid can be obtained by saponifying stearic acid containing triglycerides and separated. Stearic acid is studied in oilseed plants to understand how fatty acid production is regulated because the oxidative stability of vegetable oils can be improved by increasing stearic acid content (Fernandez-Moya *et al.*, 2005). Several oilseed crops have been selected for modification to increase stearic acid content including rapeseed, soybean with low linolenic acid content, sunflower mutants with elevated oleic acid content and other oilseed crops (Fernandez-Moya *et al.*, 2005). Stearic acid is also used in formulations in the cosmetic industry (Johnson, 2000). Stearic acid is also known for its ability to structure oils by forming 2-D crystal platelets (Daniel & Rajasekharan,

2003). The crystallization process in fats and organogelators, such as stearic acid, can then be studied to reveal how to replace traditional saturated and *trans*-fats by using organogelators.

2.6 The Crystallization Process

Crystallization is a process by which a liquid undergoes a phase change and become a solid. Unlike glasses, which are amorphous, a crystalline solid is characterized by structuring molecules in a regular repeating pattern. This phase transition from liquid to solid is a temperature and pressure dependent process. A graph of the Gibbs energy of an assumed system at varying temperature may be used in demonstrating the phase transition whereby a system can exist as a solid or liquid state (Figure 2.3) (Walstra, 2003). These two states have their associated lines which represent the Gibbs energy for that state at a given temperature (Walstra, 2003). At a given temperature, the predominant state is the one with the lower Gibbs energy (Walstra, 2003). At the point where the two lines intersect, there exists an equilibrium whereby there is no preference for either state at that temperature (Figure 2.3) (Walstra, 2003). In figure 2.3, the grey line represents the Gibbs energy for a system in the solid state while the black line represents the system in a liquid state (Walstra, 2003). The dashed portions of the lines in figure 2.3 are extrapolated to demonstrate what the Gibbs energy values would be should they exist for their respective states (Walstra, 2003).

For the phase transition to occur from a liquid to a solid state, the system is cooled till the equilibrium temperature is reached (Walstra, 2003). Beyond the equilibrium point, Figure 2.3 falsely implies that a phase transition occurs instantaneously whereby the liquid becomes a solid state as the temperature of the system continues to decrease (Walstra, 2003). In reality, supercooling is required before nucleation initiates (Walstra, 2003).

2.6.1 Supercooling

Supercooling occurs when the temperature of a system (T) is below its melting temperature (T_m). Under supercooling, the system is supersaturated meaning that the dissolved molecules are typically solid at that temperature (T). The temperature

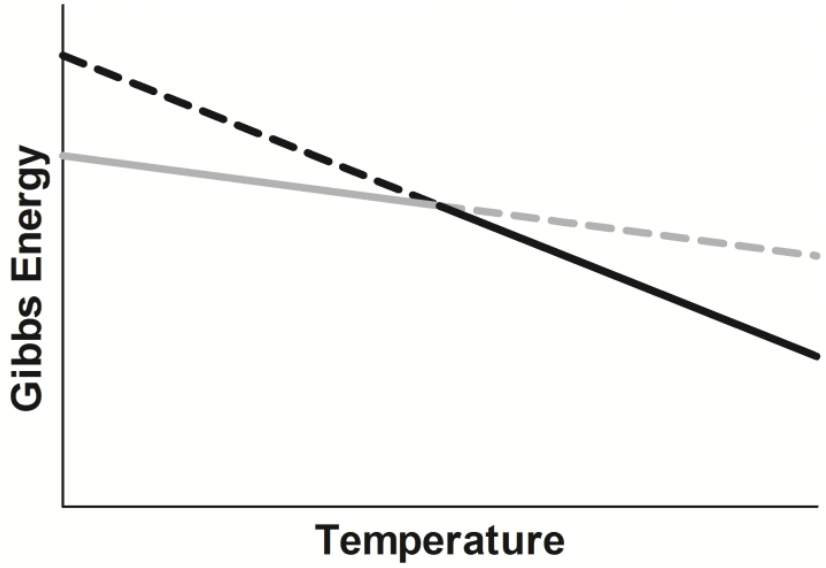

Figure 2.3: Simulated Gibbs energy as a function of temperature for the liquid (black line) and solid (grey line) phase of a system (Adopted from Walstra, 2003).

difference (T_m - T) represents the thermodynamic force, or supercooling, experienced by the system. Molecules begin to aggregate under supercooling to form clusters known as embryos. At low degrees of supercooling, a metastable region forms where stable embryos do not form because the interactions formed between the crystallizing molecules are weaker than the kinetic energy of the molecules in the melt. Stable embryos begin to form when the system is further supercooled (*i.e.* at lower temperatures) where the kinetic energy of the molecules in the melt is less than the interactions between the crystallizing molecules which hold the embryo together.

2.6.2 Nucleation

Nucleation involves the aggregation of molecules into an embryo which phase separates into a tiny crystal and become the template for crystal growth (Hartel, 2001). There are two thermodynamic components which dictate whether a nucleus will form: the positive Gibbs energy (ΔG_S) associated with the formation of the new boundary layer and the negative Gibbs energy (ΔG_V) associated with the formation of a new phase

that changes the entropy and enthalpy of a new phase (McClements & Decker, 2008). The overall Gibbs relationships may be expressed as (McClements & Decker, 2008):

$$\Delta G = \Delta G_V + \Delta G_S = \frac{4}{3}\pi r^3 \frac{\Delta H_{fus}\Delta T}{T_m} + 4\pi r^2 \gamma_i \qquad \text{(eq. 2.1)}$$

where r is the radius of the nuclei, ΔT is the difference between T_m and the temperature of the sample (*i.e.* supercooling), ΔH_{fus} is the change in enthalpy per unit volume associated with the formation of the new solid phase (which is a negative term), and γ_i is the interfacial tension (McClements & Decker, 2008). The positive Gibbs energy associated with the formation of a new boundary is proportional to the surface area of the new crystallite (Marangoni, 2005a; McClements & Decker, 2008). The negative Gibbs energy is the enthalpy and entropy components proportionate to the volume of the new nucleus (Marangoni, 2005a; McClements & Decker, 2008). As the volume of the crystallite increases, its surface area to volume ratio decreases which eventually makes the Gibbs energy for the new phase negative and thermodynamically favourable (Marangoni, 2005a; McClements & Decker, 2008). Hence, the critical radius (r_c), which is the smallest potential nucleus, is equal to (Marangoni, 2005a; McClements & Decker, 2008):

$$r_c = \frac{2\gamma_i T_m}{\Delta H_{fus}\Delta T} \qquad \text{(eq. 2.2)}$$

Above this critical radius the negative Gibbs energy term dominates which leads to the formation of a nucleus (Marangoni, 2005a; McClements & Decker, 2008). Below the critical radius, the positive Gibbs energy term dominates and the cluster of molecules will disperse due to Brownian motion to reduce the Gibbs energy of the system (Marangoni, 2005a; McClements & Decker, 2008). Equation 2.2 also demonstrates that the radius of the critical nucleus is dictated by the degree of supercooling experienced by the system (Walstra, 2003). At low degrees of supercooling, ΔT is small such that a larger critical radius (r_c) is required for nucleation and vice versa (Walstra, 2003). For the formation of a stable nucleus, molecules continuously aggregate and breakdown until a stable nucleus may be formed.

2.6.3 Crystal Growth

Crystal growth is a secondary heterogeneous nucleation process where the crystallizing molecules are incorporated onto a crystal surface. The preference for nucleation or crystal growth is affected by the supercooling experienced by the system (McClements & Decker, 2008). Under high degrees of supercooling, more nuclei are formed with less crystal growth while under low degrees of supercooling, more crystal growth occurs while fewer nuclei are formed (McClements & Decker, 2008). During crystal growth, molecules diffuse to the crystal surface, reorient and incorporate onto the crystal lattice (Walstra, 2003). If molecules are incorporated sufficiently fast, then the volume immediately surrounding the crystal surface maybe devoid of the molecules needed for crystallization (Walstra, 2003). In this scenario, crystal growth is diffusion limited (Walstra, 2003). Diffusion limited crystal growth may occur when the concentration of the crystallizing molecules is low (Walstra, 2003). If the diffusion of the molecules to the crystal surface is not limiting, then the crystal growth is reaction limited (Walstra, 2003). Reaction limited crystal growth often occurs when molecules need reorientation before incorporating onto the crystal surface (Walstra, 2003). This may occur when the thermodynamic drive for crystallization is high due to increased supercooling (Walstra, 2003). For small molecules, reorientation required at the crystal surface is minimal whereas for large polymers, such as triglycerides, reorientation may be a difficult process which may limit the rate of crystal growth (Walstra, 2003). Only a portion of the polymer requires the correct orientation to be incorporated into the crystal lattice (Walstra, 2003). With part of the polymer incorporated, the rest can reorient accordingly and attain the correct orientation (Walstra, 2003).

2.7 The Avrami Model

Modelling crystal growth is important because it helps to determine how changes in the crystallization condition affect the product. Fat crystal networks are most commonly modelled using the Avrami model (Ahmadi, Wright, & Marangoni, 2008; Boodhoo, Bouzidi, & Narine, 2009; Liu, Meng, Zhang, Shan, & Wang, 2010; Maragoni, 2005a; Metin & Hartel, 1998). The Avrami model describes the change in the volume of the new phase formed relative to the total phase volume (Avrami, 1939). This model

accounts for the nucleation and crystal growth processes for the phase transition (Avrami, 1939; Marangoni, 2005a). Furthermore, the Avrami model assumes that crystallization is stochastic, which is a process that takes place with constant probability per unit time or distance, that occurs isothermally with a constant growth rate (Avrami, 1939). Avrami observed that the formation of the solid phase from the melt begins with a period of slow growth, followed by rapid growth which slows down at the end of crystallization (Avrami, 1939). Avrami noted that a graph of the change in phase volume as function of time resembles a sigmoidal curve (Avrami, 1939). Avrami observed that by increasing supersaturation (*i.e.* supercooling), the rate for the phase transition also increases (Avrami, 1939). The Avrami equation takes the following form:

$$Y = 1 - e^{-kt^n} \qquad \text{(eq. 2.3)}$$

where Y is the volume phase change, k is the growth rate of the new phase, t is time and n is the Avrami exponent (Avrami, 1939, 1940, 1941). The rate constant (k) represents both nucleation and crystal growth (Marangoni, 2005a). The Avrami exponent dictates the mode of nucleation and the dimensionality of crystal growth. The mode of nucleation can be spontaneous or instantaneous whereas the dimensionality of crystal growth can be 1-, 2- or 3-dimensional (Avrami, 1939, 1940, 1941). Instantaneous nucleation occurs when nuclei appear within a short time span during the crystallization process whereas sporadic nucleation occurs when nuclei appear at a nucleation rate throughout the crystallization process (Marangoni, 2005a). Sharples defined the different integers of the Avrami exponent such that instantaneous and sporadic nucleation is represented by an integer of 0 and 1, respectively (Sharples, 1966). The different dimensional growth is represented by integers of 1, 2 and 3 for their respective dimensionality (Sharples, 1966). Table 2.1 illustrates the different integers which can be represented by the Avrami exponent (Sharples, 1966). Therefore when an Avrami exponent of 2 is obtained, this could indicate an instantaneously nucleating two-dimensional platelet or a sporadically nucleating one-dimensional fibre (Marangoni, 2005a).

Table 2.1: Values for the Avrami exponent, n, for different types of nucleation and crystal growth (Taken from Sharples, 1966).

n	Type of Crystal Growth and Nucleation Expected
3 + 1 = 4	Spherulitic growth from sporadic nuclei
3 + 0 = 3	Spherulitic growth from instantaneous nuclei
2 + 1 = 3	Disc-like growth from sporadic nuclei
2 + 0 = 2	Disc-like growth from instantaneous nuclei
1 + 1 = 2	Rod-like growth from sporadic nuclei
1 + 0 = 1	Rod-like growth from instantaneous nuclei

2.8 The Differences between Cooling Conditions Used to Crystallize Products

2.8.1 Isothermal Cooling Conditions

The Avrami equation was developed to model crystallization under isothermal cooling conditions (Avrami, 1939, 1940, 1941). Isothermal cooling conditions occur when a sample is cooled from its melting temperature (T_m) instantaneously to the set temperature (T_s) (Figure 2.4A) (Marangoni *et al.*, 2006b). In the industry, it is impractical to cool a large quantity of material instantaneously as heat removed in one process is typically recovered into another (Singh & Heldman, 2001). Furthermore, isothermal cooling is often beyond the capabilities of most equipment found in the industry (Marangoni *et al.*, 2006b). Instantaneous heat removal from food materials is further complicated by the low thermal conductivity, which is the amount of heat conducted through a material over time, of most foods (approximately 0.3-0.7 $Wm^{-1}K^{-1}$) (Singh & Heldman, 2001). Therefore non-isothermal cooling conditions are typically observed in industrial settings (Marangoni *et al.*, 2006b).

2.8.2 Non-Isothermal Cooling

Non-isothermal cooling conditions occur when the temperature of the material changes with time which is typically characterized by a cooling rate (Figure 2.4C) (Marangoni *et al.*, 2006b). Under non-isothermal cooling conditions, crystallization

typically begins prior to the system reaching the set temperature (Marangoni *et al.*, 2006b).

Under isothermal cooling conditions, an induction time is used to signal the onset of the crystallization process (Marangoni *et al.*, 2006b). Under non-isothermal cooling conditions, an induction time cannot be used to characterize the onset of crystallization because both time and temperature are dynamic parameters (Marangoni *et al.*, 2006b). Therefore, non-isothermal cooling conditions are characterized by a crystallization temperature (T_c) and a crystallization time (t_c) (Marangoni *et al.*, 2006b). The crystallization temperature (T_c) is the temperature when the first nucleus appears. The crystallization time (t_c) is the time the system has been supercooled prior to T_c being reached (Marangoni *et al.*, 2006b).

Under isothermal and near-isothermal cooling conditions, the set temperature relative to the melting temperature dictates the degree of supercooling experienced by the sample which characterizes the thermodynamic drive for the phase transition. Under non-isothermal cooling conditions, the characteristic driving force for the phase transition is not simply the supercooling but instead is the temperature-time profile experienced by the sample. Therefore the supercooling-time-trajectory parameter (β) was developed to characterize the thermodynamic drive for the phase transition under non-isothermal cooling conditions, which includes both the time and temperature experienced by the system (Marangoni *et al.*, 2006b).

Under non-isothermal cooling conditions, the Avrami model cannot be used to characterize the crystallization process. The Avrami model assumes that crystallization occurs under isothermal cooling conditions (Avrami, 1939, 1940, 1941). Therefore each set temperature has its associated rate constant for crystallization (Avrami, 1939, 1940, 1941). The Avrami model implies that the rate constant changes over time because the temperature of the system changes over time under non-isothermal cooling conditions (Rogers & Marangoni, 2009). The application of the Avrami model under these circumstances is incorrect because the assumptions for this model do not apply (Rogers & Marangoni, 2009). Therefore new models which can model the crystallization

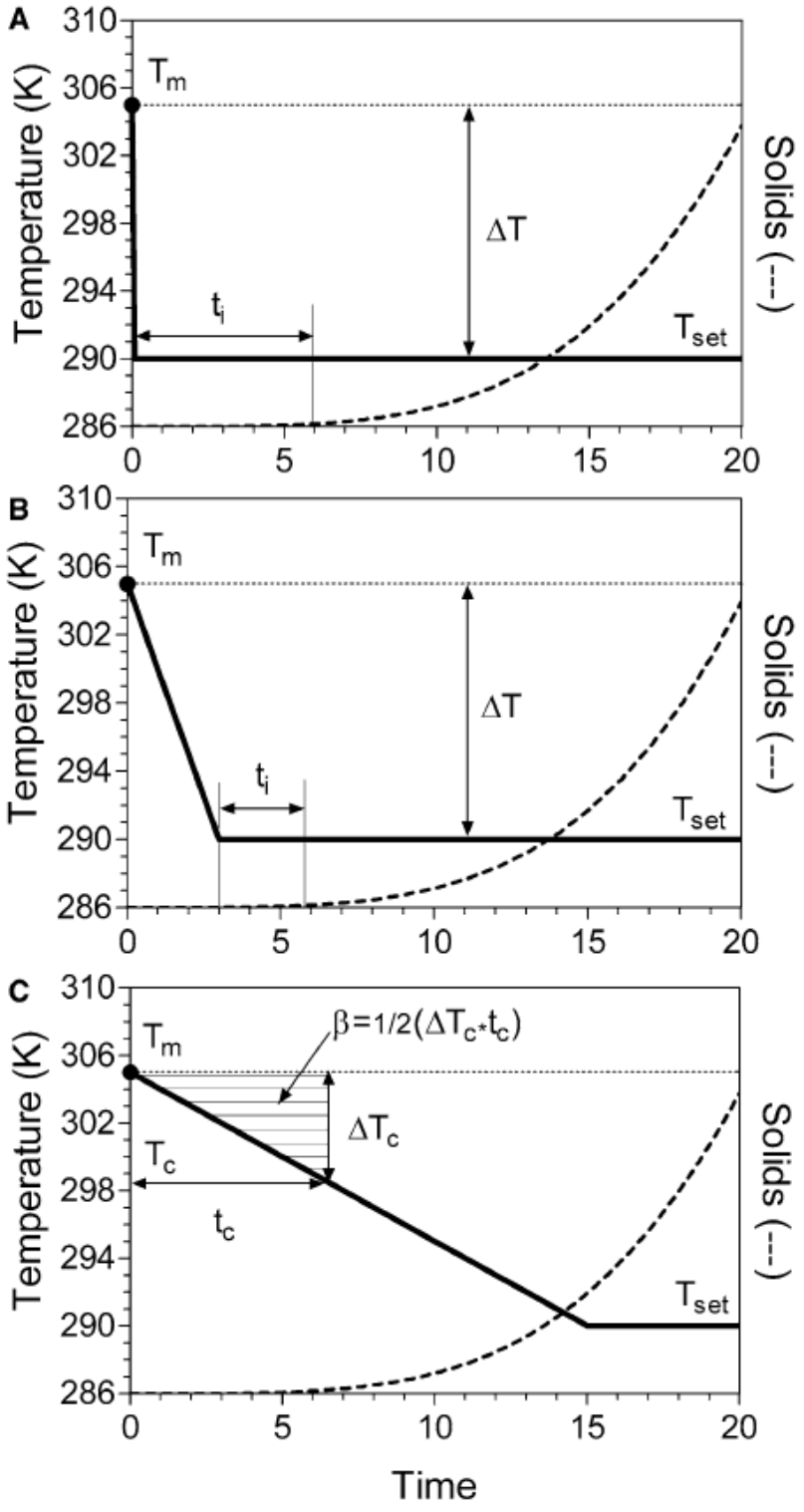

Figure 2.3: Temperature and crystallization profiles for materials crystallizing under isothermal (A), near-isothermal (B) and non-isothermal (C) conditions (Taken from Marangoni, et al., 2006b)

process under non-isothermal cooling conditions are imperative. A versatile model will be capable to account for the crystallization process, different modes of nucleation and dimensionalities of crystal growth.

3. Study 1: Experimental Validation of the Modified Avrami Model for Non-Isothermal Crystallization Conditions[1]

3.1 Abstract

The modified Avrami model was found to accurately predict the induction time, maximum phase volume and dimensionality of crystal growth for stearic acid containing molecules when the experimental method employed measures as a function of the phase volume. Four methods were examined to validate the model including: Fourier transformed infrared spectroscopy (FT-IR), differential scanning calorimetry (DSC), small deformation rheology and polarized light microscopy (PLM). PLM and FT-IR were able to detect the nucleation event prior to DSC and rheology. FT-IR and PLM provided the most accurate data due to similarities between the experimental and fitted induction times (x_0), maximal phase change (Y_{max}) and the Avrami exponent (n). Further, the Avrami exponent, obtained from FT-IR, was sensitive to both the mode of nucleation and the dimensionality of crystal growth. Therefore, the apparent rate constants (k_{app}) obtained by FT-IR and PLM are useful in providing further insights into the kinetics of non-isothermal crystallization. The calculated apparent rate constants suggest a diffusion limited crystallization at slow cooling rates (*i.e.*, below 5-7 °C/min) and at cooling rates greater than 5-7 °C/min, the incorporation of the gelator molecules onto the crystal lattice becomes limited by the reaction rate constant.

3.2 Introduction

Dimensionality of crystal growth is essential in determining the physical properties of crystalline materials (Hu, Odom, & Lieber, 1999). The dimensionality of crystal growth is represented by the number of axes of the crystal in which growth takes place (Figure 3.1). For 1-dimensional crystals, growth occurs in one axis, for

[1]Chapter 3 was published in: CrystEngComm, (2011). 13(3), 866-875. DOI: 10.1039/C0CE00523A – Reproduced with permission of The Royal Society of Chemistry (RSC) - http://pubs.rsc.org.cyber.usask.ca/en/Content/ArticleLanding/2011/CE/c0ce00523a#divAbstract

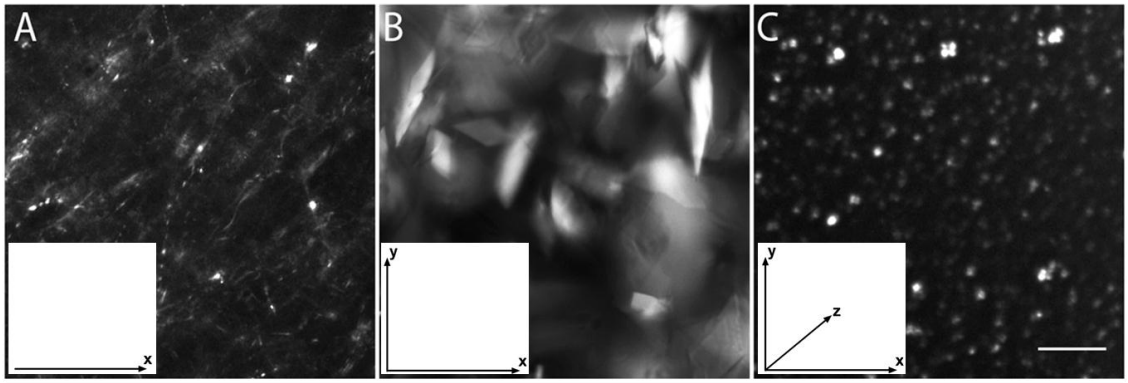

Figure 3.1: Polarized light micrographs of 1D fibres (12-hydroxystearic acid) (A), 2D platelets (stearic acid) (B), and 3D spherulite (trihydroxystearin) (C) with their respective axes of crystal growth represented by x, y and z. Bar = 5 µm.

2- dimensional crystals growth occurs in two axes forming a plane and for 3-dimensional crystals growth occurs on all 3 axes forming a sphere. Emphasis has traditionally focused on high-dimensionality crystals in fields such as oxide and phosphate inorganic chemistry (Holland, Blanford, Do, & Stein, 1999) polymer chemistry (Wang, Li, Hanzlicek, Cheng, Geil, Gerbowicz, & Ho, 2001), and lipid chemistry (Marangoni, 2005a). However, current advances in low-dimensionality crystals including nanowires, nanotubes and nanoplatelets are becoming crucial for numerous practical applications propelling these technologies to the forefront of crystal physics and chemistry. Low-dimensionality crystals are revolutionizing lipid chemistry (Bot & Agterof, 2006; Gandolfo *et al.*, 2004; Rogers, 2009; Rogers *et al.*, 2009a; Rogers, Wright, & Marangoni, 2009b), ceramics (Li & Xia, 2004), and chemo-responsive gels (Hanabusa, Miki, Taguchi, Koyama, & Shirai, 1993). To further the applications of low-dimensionally crystals not only a practical understanding is required but also a fundamental understanding into their nucleation and crystal growth mechanisms is essential (Jin, Song, & Pan, 2007).

Nucleation events result in the formation of a new phase from the 'mother' state *via* the formation of a three-dimensional spherical cluster or a "crystal embryo". The cluster forms, as the solution is cooled below the melting temperature, resulting in a super-saturated state causing molecules to microscopically or macroscopically phase separate (Weiss & Terech, 2006). "Crystal embryos" are spherical minimizing the

surface free energy (*i.e.*, the major energy barrier needed to be overcome during crystallization) of the interface between the new phase and the previously existing phase. A meta-stable region exists because Brownian forces disrupt the formation of the crystal embryo while the formation of non-covalent interactions stabilizes the embryo. At elevated temperatures the Brownian forces exceed the non-covalent forces and the embryo is unstable. At lower temperatures, the non-covalent forces exceed the Brownian forces and the nuclei are stable. Depending on the cooling profile the mode of nucleation may be instantaneous (*i.e.*, all nuclei form at once) or sporadic (*i.e.*, nuclei form as a function of time). Following nucleation, the crystal grows either as three-dimensional spheres, two-dimensional plates or discs, or one-dimensional fibres.

Crystal physics has long been concerned with not only the rate of crystal growth but also the dimensionality of how materials assemble during crystallization (Avrami, 1939, 1940, 1941). For practical applications, the effect of non-isothermal crystallization conditions on the microstructure and macrostructure is of utmost importance (Rogers & Marangoni, 2008, 2009). The kinetics of a phase change is frequently modeled using the Avrami equation where it is assumed that the number and size of the crystals is a function of time and temperature (Avrami, 1939). The Avrami model has previously been derived from Fick's first law of diffusion (Marangoni, 2005a).

However, in industrial applications, crystallization typically occurs under non-isothermal cooling conditions (*i.e.*, the temperature changes as the material crystallizes) inducing different physical properties. The nucleation and crystallization rate change as a function of time because heat and mass transfer conditions evolve as temperature is decreased. Nucleation behaviour is of great importance due to the effect on structural features including crystal size, crystal morphology and the spatial distribution of crystalline mass (Marangoni & McGauley, 2003; Rogers, Wright, & Marangoni, 2008b; Rogers *et al.*, 2009a). Therefore, the model for isothermal cooling has been adapted for non-isothermal conditions and takes the following form (Rogers & Marangoni, 2008, 2009):

$$\frac{Y_S}{Y_{max}} = 1 - e^{-k_{app}(x-x_0)^n} \quad \text{(eq. 3.1)}$$

where k_{app} is the apparent rate constant, x is the time and x_0 is the induction time, n is the Avrami exponent representing both the dimensionality of growth and mode of nucleation. The Avrami exponent (n) is a function of both the dimensionality of crystal growth as well as the mode of nucleation (*i.e.*, sporadic or instantaneous) (Sharples, 1966). Although numerous reports have been presented using the non-isothermal Avrami model there has yet to be a systematic study evaluating the applicability of this model or the experimental techniques used to measure the change in crystal phase volume. Not all techniques used to measure crystal phase volume are applicable because crystal growth may occur beyond the maximum measured phase change such as in turbidity measurements (Marangoni, 1998).

Two other approaches to modeling crystal growth under non-isothermal cooling conditions have been reported (Bouzidi & Narine, 2010; Rousset, 2002; Smith, Cain, & Talbot, 2005). Rousset developed the finite element method which utilizes the isothermal time, temperature and transformation diagrams (FEM-TTT) (Rousset, 2002). Isothermal time-temperature-transformation (TTT) diagrams are crystallization data collected under isothermal cooling conditions at different temperatures (Rousset, 2002). FEM-TTT utilizes isothermal data which is applied to non-isothermal cooling conditions (Rousset, 2002). The thermal path for crystallization under non-isothermal conditions is obtained and split into small segments which are analyzed isothermally (Rousset, 2002). Each segment is assigned a corresponding isothermal temperature whereby data from TTT diagrams are used to extrapolate the relative amount of phase transition undergone at that time interval (Rousset, 2002). A series of these time segments are analyzed isothermally and pieced together to determine the path of the phase transition experienced by the sample under non-isothermal cooling conditions (Rousset, 2002).

An isoconversional method to model phase transition in lipids has also been reported where data are not fitted to a specific model (Bouzidi & Narine, 2010; Smith *et al.*, 2005). The phase transition is captured and the first derivative is utilized to measure the change in the rate of the phase transition as the sample undergoes non-isothermal

cooling conditions (Bouzidi & Narine, 2010; Smith *et al.*, 2005). The FEM-TTT and the isoconversional methods both provide phase transition kinetics but provide no data on the mode of nucleation or the dimensionality of crystal growth. In these two models the kinetic data are determined experimentally and *via* the model which can be compared for accuracy; however, there are no alternative parameters to verify their accuracy. The modified Avrami model can utilize the Avrami exponent, which indicates the mode of nucleation and dimensionality of crystal growth, induction time, and the maximal crystal phase volume to verify the fit to the experimental data.

In this systematic study, three stearic acid containing molecules were examined to assess the modified Avrami model. 12-hydroxystearic acid (12HSA) crystallizes into one-dimensional fibres (Figure 3.1A) (Huang & Weiss, 2007; Huo *et al.*, 2008; Li *et al.*, 2009; Mallia, George, Blair, & Weiss, 2009; Rogers & Marangoni, 2008, 2009; Rogers *et al.*, 2008b, 2009a, 2009b; Terech & Weiss, 1997). This is due to the incorporation of 12HSA molecules *via* van der Waals interactions and hydrogen bonding (Suzuki *et al.*, 2003). Stearic acid (Figure 3.1B) crystallizes into two-dimensional rhombic platelets (Gandolfo *et al.*, 2004; Schaink *et al.*, 2007; Swamy *et al.*, 1985). Trihydroxystearin (Figure 3.1C) forms three-dimensional spherulitic crystals. In 2- and 3-D systems, growth occurs with the alignment of the alkane chains which maximizes the van der Waals interactions required for crystal growth among stearic acid and trihydroxystearin (Marangoni, 2005b; Suzuki *et al.*, 2003). The purpose of this research is to experimentally validate the use of the modified Avrami equation under non-isothermal crystallization conditions.

3.3 Derivation of the Modified Avrami Model from Fick's First Law of Diffusion

Fick's first law of diffusion is:

$$\frac{\partial Q}{\partial t} = D A_d \left(\frac{\partial C}{\partial x_d}\right) \qquad \text{(eq. 3.2)}$$

where $\partial Q/\partial t$ is the number of moles of material (Q) crystallized as a function of time (t), D is the diffusion coefficient, A_d is the area of diffusion and $\partial C/\partial x_d$ is the changing concentration of soluble material (C), which is the decrease due to crystallization, across

a thickness (x_d) of boundary layer. If the mass of a crystal (Y_c) is proportional to the number of moles and the molecular weight of the crystallizing molecules (MW), then diffusion across the boundary layer onto the crystal surface may be rewritten as:

$$\frac{\partial Y_c}{\partial t} = \frac{\partial Q}{\partial t} MW \; or \; \frac{\partial Y_c}{\partial t} = DA_d \left(\frac{\Delta C}{\Delta x_d}\right) MW \qquad \text{(eq. 3.3)}$$

The rate of mass deposition onto a crystal surface can be expressed as a rate constant for crystal growth (k_g). This parameter (k_g) is typically used in describing crystal growth and accounts for the two steps required for an increase in crystalline mass: the diffusion of the molecule to the crystal surface (D) across a distance (Δx_d) and the rate of incorporation of the molecule into the crystalline surface (κ_s). Hence k_g takes the following form (Marangoni, 2005a):

$$k_g = \left(\frac{1}{D} + \frac{1}{\kappa_s}\right)^{-1} {\Delta x_d}^{-1} \qquad \text{(eq. 3.4)}$$

and

$$(c - c*) = MW \, \Delta C \qquad \text{(eq. 3.5)}$$

where c is the concentration of the supersaturated material and c* is the equilibrium saturation concentration of the material per unit volume. Substituting equation 3.4 and 3.5 into equation 3.3 attains the following relationship:

$$\frac{\partial Y_c}{\partial t} = k_g A_d (c - c*) \qquad \text{(eq. 3.6)}$$

Equation 3.5 may be rewritten since the mass of total solids (Y_s) is a function of the number of crystals (N) and the mass of the crystals (Y_c) assuming that the crystals are homogenous in nature:

$$\frac{\partial Y_s}{\partial t} = N k_g A_d (c - c*) \; while \; (c - c*) = \frac{Y_{max} - Y_s}{V_t} \qquad \text{(eq. 3.7)}$$

where (Y_{max}-Y_s) is the amount of uncrystallized material (Y_{max} is the total amount of solids at infinity and Y_s is the total solids at a given time) and V_t is the volume of the system. The number of crystals per unit volume (ρ) can be written as:

$$\rho = \frac{N}{V_t} \qquad \text{(eq. 3.8)}$$

substituting equation 3.6 and 3.7 into 3.5 followed by variable separation leads to the Avrami equation derived by Marangoni (2005a):

$$\frac{\partial Y_s}{(Y_{max} - Y_s)} = k_g \rho A_d \partial t \qquad \text{(eq. 3.9)}$$

At this point, equation 3.8 represents instantaneous nucleation followed by crystal growth. In the case of sporadic nucleation, the number of crystals per unit volume (ρ) is a function of time (t) and the nucleation rate (j_c) and for sporadic nucleation equation 3.8 is modified to become:

$$\frac{\partial Y_s}{(Y_{max} - Y_s)} = k_g j_c t A_d \partial t \qquad \text{(eq. 3.10)}$$

Depending on the dimensionality of growth the area of the growing surface is represented by a sphere ($(A_d = 4\pi r_{sphere}^2)$ where A_d is the area and r_{sphere} is the radius), a platelet ($(A_d = 4lh)$ where l is the dimension of the growing plate and h is the non-propagating surface) or a fibre ($(A_d = 2\pi r_{fibre}^2)$ where r_{fibre} is the radius). For the radius of the sphere (r_{sphere}) it is assumed it grows at a linear growth rate (g) as a function of time (t). Similarly, the growing dimension of the platelet (l) also has a linear growth rate (g) (r=gt for a sphere or l=gt for a platelet).

Hence the Avrami model, for each mode of nucleation and crystal growth shape, may be derived by substituting the growth area and the nucleation term. For illustration purposes the Avrami model for instantaneous nucleation with spherical growth (equation 3.10) is shown:

$$\frac{\partial Y_s}{(Y_{max} - Y_s)} = k_g \rho (4\pi g^2 t^2) \partial t \qquad \text{(eq. 3.11)}$$

equation 3.10 may be integrated across the boundary condition $m_s=0$ at time t=0 and m_s at t:

$$\int_0^{m_s} \frac{\partial Y_s}{(Y_{max} - Y_s)} = k_g \rho 4\pi g^2 \int_0^t t^2 \partial t \qquad \text{(eq. 3.12)}$$

resulting in:

$$\ln\left(\frac{Y_S}{(Y_{max}-Y_S)}\right) = k_g\rho\frac{4}{3}\pi g^2 t^3 \quad \text{(eq. 3.13)}$$

which rearranges to:

$$\frac{Y_S}{Y_{max}} = 1 - e^{k_g\rho\frac{4}{3}\pi g^2 t^3} \quad \text{(eq. 3.14)}$$

hence for instantaneous nucleation and spherulitic crystal growth the Avrami equation is:

$$\frac{Y_S}{Y_{max}} = 1 - e^{K_c t^3} \quad \text{(eq. 3.15)}$$

Where $K_c = k_g\rho\frac{4}{3}\pi g^2$ and n=3. Using the same logic in which equation 3.14 was derived; the other possible forms of the Avrami model are presented (Table 3.1).

3.4 Materials and Methods

12HSA (Nu-Chek Prep, Elysian, MN, USA), stearic acid (Sigma Aldrich, Oakville, ON) and trihydroxystearin (Nu-Chek Prep, Elysian, MN, USA) were purchased and used as received. Three percent (w/w) of the stearic acid containing molecules were added to heavy mineral oil (Sigma Aldrich, Oakville, ON, CA) and were melted at 90 °C and held for 10 minutes to erase crystal memory. Cooling rates of 1-10 °C/min at 1 °C increments, and at 15 °C/min were applied to the samples when cooling from 90 °C to 30 °C.

3.4.1 Synchrotron Fourier Transform-Infrared Spectroscopy (FT-IR)

FT-IR was done at the Canadian Light Source (Saskatoon, SK, Canada) on the mid-IR beamline (beamline 01 B1-01, Canadian Light Source, Saskatoon, SK). The end station used is comprised of a Bruker Optics IFS66v/S interferometer coupled to a Hyperion 2000 IR microscope (Bruker Optics, Billerica, MA, USA). Light was focused on the system using a 15x magnification Schwarzschild condenser, collected by a 15x magnification Schwarzschild objective with the aperture set to a spot size of 40 µm by

Table 3.1: Possible Forms of the Avrami model for the different modes of nucleation and their associated dimensionality of crystal growth (Marangoni, 2005a):

Mode of Nucleation	Dimensionality of Crystal Growth	Avrami Equation	K_c	n
Instantaneous	Linear	$\frac{Y_s}{Y_{max}} = 1 - e^{Kt^1}$	$2\pi r^2 k_g j_c$	1
Sporadic	Linear	$\frac{Y_s}{Y_{max}} = 1 - e^{Kt^2}$	$\pi r^2 k_g j_c$	2
Instantaneous	Platelet	$\frac{Y_s}{Y_{max}} = 1 - e^{Kt^2}$	$2hk_g\rho g$	2
Sporadic	Platelet	$\frac{Y_s}{Y_{max}} = 1 - e^{Kt^3}$	$\frac{4}{3}hk_g j_c g$	3
Instantaneous	Spherulitic	$\frac{Y_s}{Y_{max}} = 1 - e^{Kt^3}$	$k_g\rho\frac{4}{3}\pi g^2$	3
Sporadic	Spherulitic	$\frac{Y_s}{Y_{max}} = 1 - e^{Kt^4}$	$j_c k_g \pi g^2$	4

40 µm and detected by a liquid nitrogen cooled narrowband MCT detector utilizing a 100 µm sensing element.

Spectra were collected at 32 scans per measurement from 690 to 7899 cm^{-1} at a spectral resolution of 4 cm^{-1}. The temperature controlled stage [LTS120 and PE94 temperature controller (Linkam, Surrey, UK)] was used to modify the cooling rate while collecting spectrum on the FT-IR instrument.

A KBr-supported Ge multilayer beam splitter was used to measure spectra in the mid-infrared spectral region. Measurements were taken using the Opus 6.5 software (Bruker Optics, Billerica, MA). The systems were held in between two calcium fluoride optical windows (25 mm diameter, 2 mm thick) with a 15 µm Teflon spacer. Approximately 10 mg of the melted sample were held between the two calcium fluoride optical windows. The non-covalent hydrogen bonding was determined by analyzing for the carboxyl and hydroxyl peak at 1710 cm^{-1} and 3200 cm^{-1} respectively (Lin-Vien, Colthup, Fateley, & Grasselli, 1991). A spectrum was taken of the samples in the molten state at 90 °C where all subsequent spectra taken were compared to and the difference plotted. The peaks were analyzed by determining the area under these peaks using the Opus 6.5 Software (Bruker Optics, Billerica, MA). The areas for the two peaks were plotted as a function of time and fitted to the modified Avrami model. Due to restrictions such as the availability of time on the synchrotron, one replicate was performed for this analysis.

3.4.2 Differential Scanning Calorimetry

A Q2000 Differential Scanning Calorimeter (DSC) (TA Instruments, New Castle, Delaware, USA) was used to detect the evolution of heat during the exothermic phase transition. 8-10 mg of sample was hermetically sealed in aluminum pans and thermograms were collected as the sample was cooled at different rates. TA analysis software (TA Instruments, New Castle, Delaware, USA) applied a running integral across the enthalpy peak associated with crystallization. The onset of crystallization was determined by the observable inflection point on the collected thermograms. From the inflection point, the thermogram was integrated until no significant change was observed

between data points. The obtained integrated curve followed a sigmoidal line indicative of a crystallization event and was fitted to the modified Avrami model. Three replicates were performed for this analysis to obtain statistical significance.

3.4.3 Small Deformation Rheology

An AR1000 rheometer with a 4 cm diameter flat stainless steel parallel plate geometry monitored the evolution of the storage modulus (G′) (TA Instruments, New Castle, Delaware, USA). Approximately 1.26 mL of the melted sample was held by the rheometer between the Peltier plate and the geometry. The sample thickness was controlled by the rheometer and held at 1000 μm. The measurements were conducted using a 10 Pa oscillatory stress and a frequency of 1 Hz as it was cooled from 90 °C to 30 °C. 10 Pa was selected as the ideal oscillatory stress as it was the lowest value obtained from the linear viscoelastic region in the solid state for all the samples. The modified Avrami model was fitted to the evolving G′. Three replicates were performed for this analysis to obtain statistical significance.

3.4.4 Polarized Light Microscopy

A Nikon Eclipse E400 light microscope equipped with a Nikon DS-FiL color camera and a long working distance 10x lens and condenser (Nikon Instruments Inc., Melville, NY, USA) was used to acquire polarized light micrographs. A temperature controlled stage (LTS120 and PE94 temperature controller (Linkam, Surrey, UK)) was used to control the cooling rates. The image resolution was 2560 by 1920 pixels. Images were analyzed using Adobe Photoshop Extended CS4.0 (Adobe Systems Incorporate, San Jose, CA, USA) to determine the length of the crystals. Sample preparation consists of taking a drop of the melted sample and spreading it onto a glass microscopy slide. Micrographs were taken as the sample cooled and the average of 10 crystals was taken to represent the average length at a given time. The growth of the average crystal length was measured as a function of time for each cooling rate. Three replicates were obtained to ensure statistical significance.

3.4.5 Fitting the Modified Avrami Model

Fitting the data was done using Graphpad Prism 5.0 (www.graphpad.com, La Jolla, CA) where initial values of Y_{max}, k_{app}, x_0 and n were given and the software determined the best fit values through an iterative process (1000 iterations). None of the terms were confined during the iterative process. The initial Y_{max} used was the maximum signal detected. The exponent n was initially set to 1, 2, or 3 for 12HSA, stearic acid and trihydroxystearin; respectively. Finally, k_{app} and x_0 were set to zero and determined by the software.

3.5 Results and Discussion

Carboxylic acid dimerization is observed by the increase in the peak area at 1710 cm^{-1} and a simultaneous decrease at 1700 cm^{-1} corresponding to the stretching of the free carboxylic acid monomer (Lin-Vien *et al.*, 1991). Dimerization of the free carboxylic acid groups and the hydrogen bonding of the hydroxyl group at position 12 on the fatty acid may be monitored using FT-IR for 12HSA (Figure 3.2A). Stearic acid crystallization was monitored by the dimerization of the carboxylic acid monomers (Figure 3.2B). Trihydroxystearin crystallization was monitored by the 3200 cm^{-1} peak corresponding to the hydrogen bonding at the 12 carbon position on the fatty acid (Figure 3.2C). The areas of these peaks have previously been correlated to the formation of non-covalent intermolecular interactions in the crystalline phase and have been used to quantify the amount of crystalline material (Cornel & Mazzotti, 2009; Huang, Gu, & Ozaki, 2006). Since FT-IR has been used to measure the phase volume it is an ideal method to fit the modified Avrami model too. The CH_2 stretching was detected, however, it was not possible to differentiate changes for the crystalline phase from the mineral oil. Therefore no analysis could be complied on the CH_2 groups in the sample. The FT-IR signals (Figure 3.2A-C) were integrated and the area under the curve was plotted as a function of time and fitted to the modified Avrami model (Figure 3.2D-F) obtaining the Avrami exponent, induction time and maximum phase change.

DSC is commonly used to measure the heat released during exothermic crystallization events (Ahmadi *et al.*, 2008; Bouzidi & Narine, 2010; Campus, Ollivon,

& Marangoni, 2010; Chaleepa, Szepes, & Ulrich, 2010; Grompone, Correa-Cabrera, & Irigaray, 1999; Sato, 2001; Smith *et al.*, 2005). A single enthalpic peak was observed for each of the gelator molecules during crystallization and the peak (Figure 3.3A-C) was integrated using a running integral which was then fitted to the modified Avrami model (Figure 3.3D-F). The use of the running integral to represent the crystallization process in DSC has been previously reported and the data collected were fitted to the modified Avrami model (Figure 3.3D-F) (Bouzidi & Narine, 2010).

The presence of network formation was monitored though the storage modulus (G′) (Figure 3.4). Although the plot gave a sigmodial shaped curve which the Avrami equation is typically used to model; G′ is not a measure of the phase volume of the new phase. The storage modulus or the elastic component of the material is a function in part of the solid content but also a function of the spatial distribution of mass, crystal shape and entanglement of the new phase.

Finally, PLM visualizes birefringent anisotropic crystals. Birefringence is the double refraction of light through an anisotropic material (Campos, 2005). PLM allows for the visualization of crystal microstructure where birefringent anisotropic crystals appear bright while the liquid oil remains dark under polarized light (Campos, 2005). Under PLM, 12HSA appears as long helical fibres which are observed as a segmented line representing the crystals being in and out of phase with the cross polarizers (Figure 3.1A) (Fuhrhop, Schnieder, Rosenberg, & Boekema, 1987; Rogers, 2009; Rogers *et al.*, 2008b, 2009a; Tachiban & Kambara, 1968; Terech, Rodriguez, Barnes, & McKenna, 1994; Uzu & Sugiura, 1975). Stearic acid crystals are rhombic shaped (Gandolfo *et al.* 2004; Schaink *et al.*, 2007; Swamy *et al.*, 1985) (Figure 3.1B) and trihydroxystearin appears as Maltese crosses (Figure 3.1C). Spherical growth is often identified by the presence of the Maltese cross under polarized light (Berger, Jewell, & Pollitt, 1979; Gioielli, Simoes, & Rodrigues, 2003; Meara, 1980). For 12HSA, the length of the fibre was recorded. For stearic acid, the maximum length of the rhombic crystal was recorded and the radius of a trihydroxystearin spherulites crystal was determined. However, the measurement must be converted to a measure of the phase volume prior to fitting the data to the modified Avrami model. The fibre length is characteristic of the phase

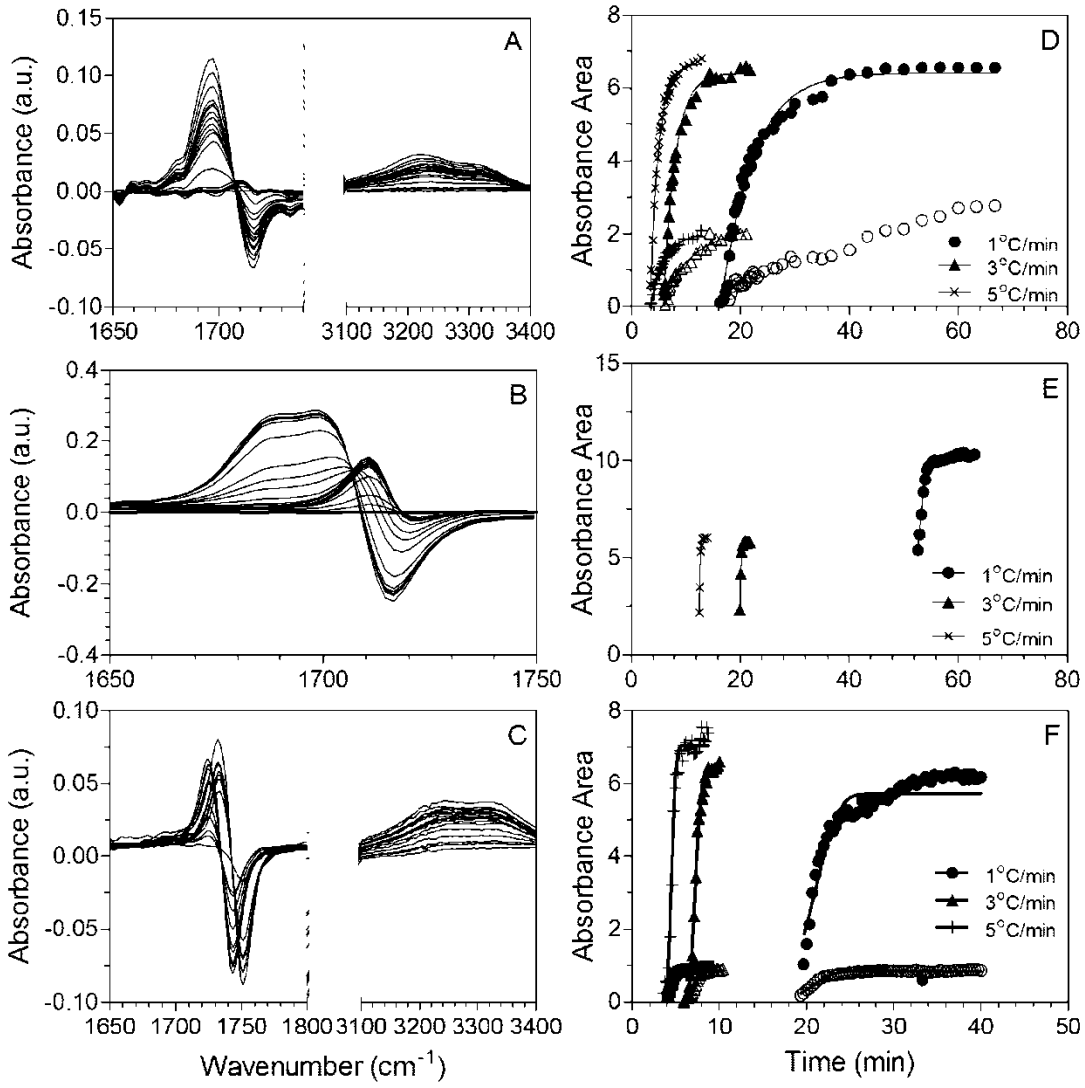

Figure 3.2: A sampling of FT-IR spectrums of 12HSA (A), stearic Acid (B) and trihydroxystearin (C) cooled at 1 °C/min from 90 °C to 30 °C and their respective area under the peak plotted over time fitted to the modified Avrami model (D, E, and F respectively). The filled and open in data points for Figures D and F represent the carboxyl peak (1710 cm^{-1}) and hydroxyl peak (3200 cm^{-1}) respectively.

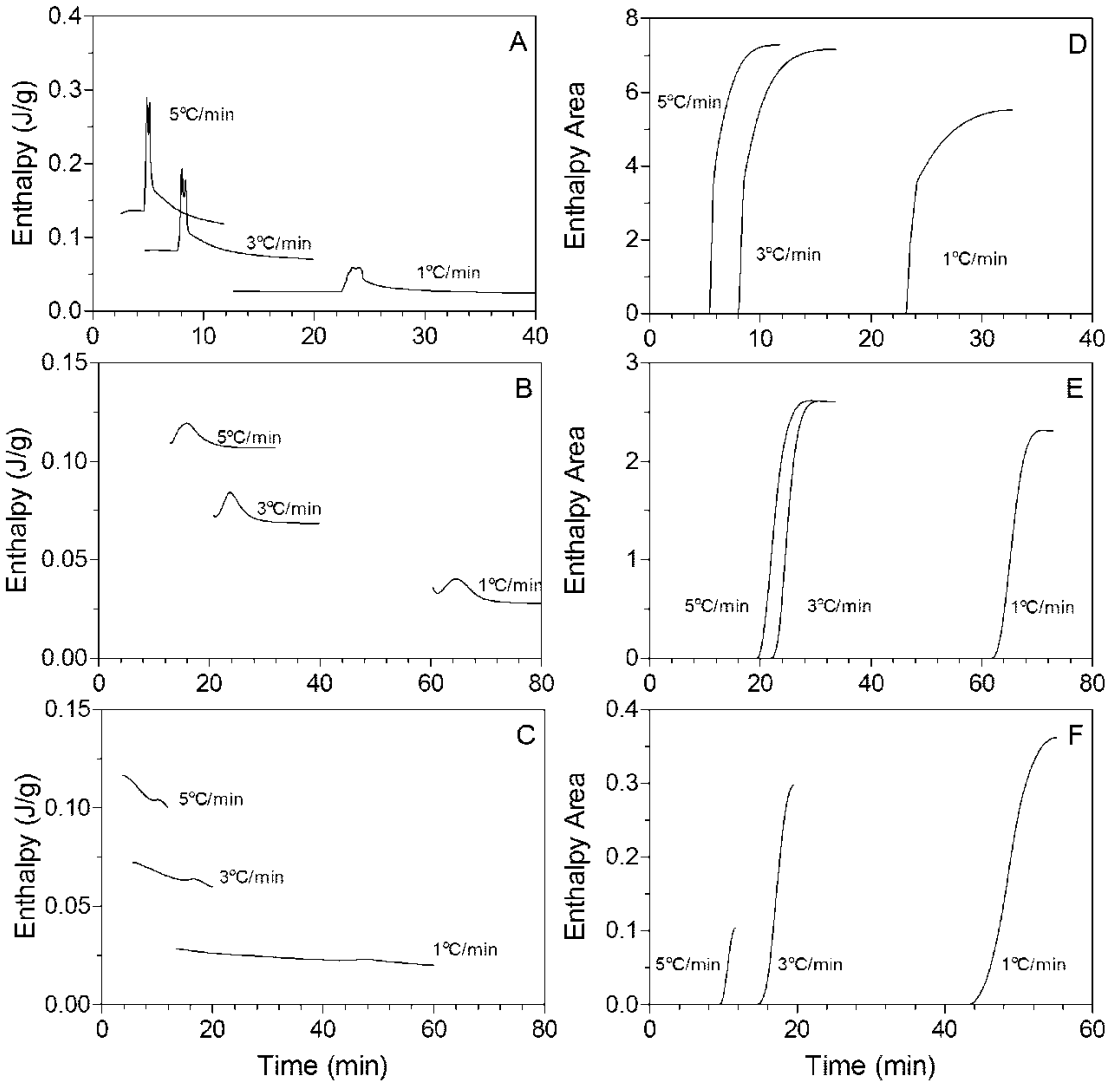

Figure 3.3: A sampling of DSC thermograms of 12HSA (A), stearic acid (B) and trihydroxystearin (C) cooled at different rates and a plot of their respective continuous integration for the different cooling rates fitted to the modified Avrami model (D-F respectively).

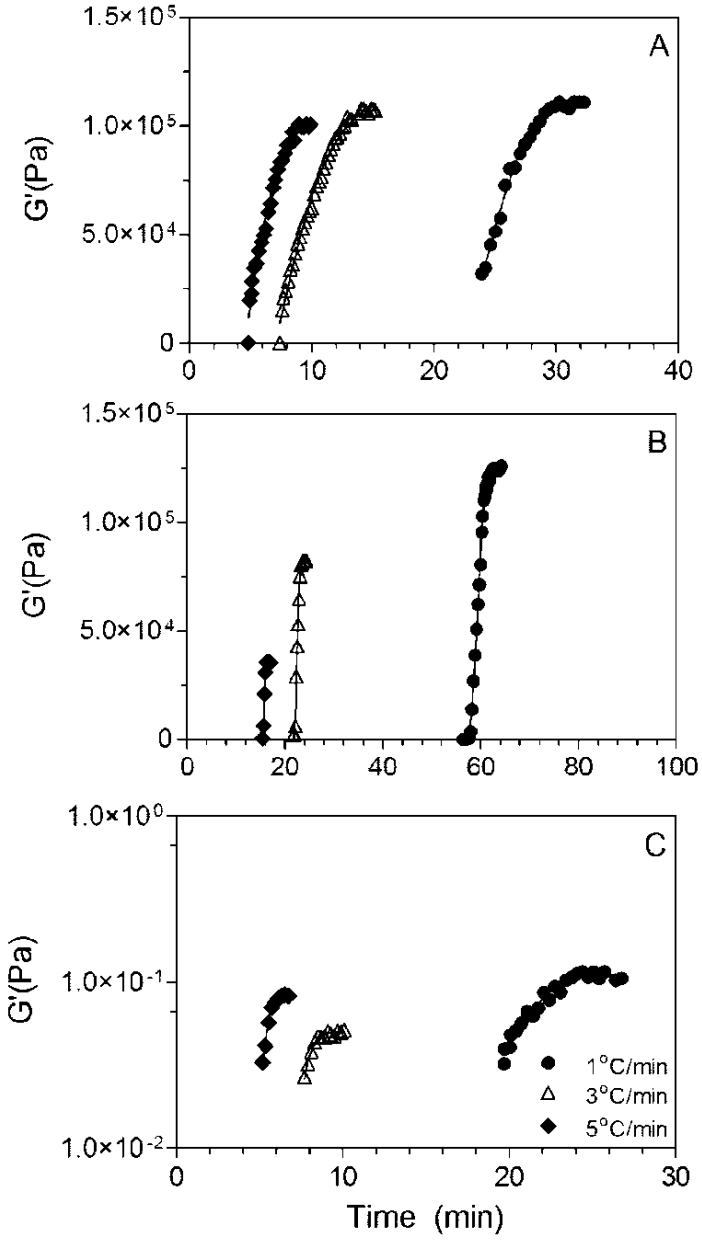

Figure 3.4: A sampling of the storage modulus obtained for 12HSA (A), stearic acid (B) and trihydroxystearin (C) collected under different cooling rates and fitted to the modified Avrami model.

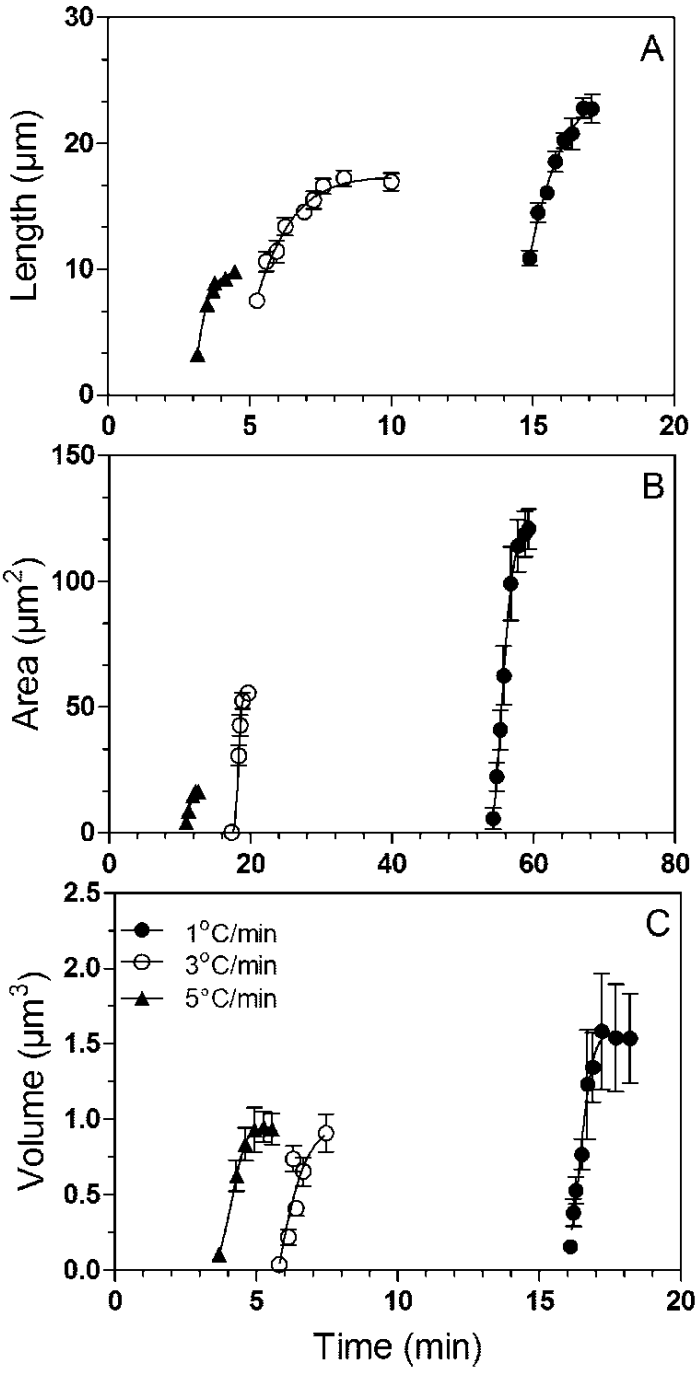

Figure 3.5: A sampling of PLM characteristic lengths corrected for their dimensionality of crystal growth for 12HSA 1-D fibres (A), stearic acid 2-D platelets (B) and trihydroxystearin 3-D spheres (C) and fitted to the modified Avrami model.

volume in one dimensional growth. For the two and three dimensional samples, the measurement of the maximum length in a crystal is not representative of their respected dimensionalities. The phase volume for platelets was approximated by calculating the area of the platelet and squaring the length, while for trihydroxystearin phase volume was determined cubing the radius to determine the area for a sphere. The crystal phase volume was plotted as a function of time and fitted to the modified Avrami model (Figure 3.5).

A sigmoidal crystal growth curve was found for each sample, cooling rate and technique measured (Figure 3.2-5). The Avrami exponents obtained from the fits to the modified Avrami model are presented in Figure 3.6. Figure 3.6 indicates that the model accurately predicted the correct dimensionality of growth using DSC (Figure 3.6C, G and K) and PLM (Figure 3.6B, F and J). While for FT-IR (Figure 3.6A, E and I) the correct dimensionality of crystal crystal growth and mode of nucleation were predicted. Sporadic nucleation occurred at slow cooling and instantaneous nucleation at faster cooling rates which are congruent to general principles of crystallization. At low degrees of supercooling (*i.e.*, low cooling rates) the activation energy for nucleation is harder to overcome leading to greater ease of crystal growth than nucleation (Marangoni, 2005a). At high degrees of supercooling, the activation energy is easier to overcome and nucleation is favoured over crystal growth which leads to a high nucleation rate and smaller crystals (Marangoni, 2005a).

Fractional Avrami exponents were observed when the storage modulus, determined using rheology, was fitted to the modified Avrami model (Figure 3.6D, H and L). It is possible that the fractional Avrami exponents may be due to the contraction of the material during cooling which affects the G′ obtained. A true-gap system has been shown to improve rheological results during crystallization as it accounts for the contraction of the material (Morales-Rueda, Dibildox-Alvarado, Charo-Alonso, & Toro-Vazquez, 2009). The storage modulus is not only a function of the change in phase volume but also the spatial distribution of mass, crystal size and inter-crystal interactions (Lam, Quaroni, Pedersen, & Rogers, 2010). Therefore, the measure of the system is not purely a measure of the change in phase volume (Avrami, 1939; Lam *et al.*, 2010).

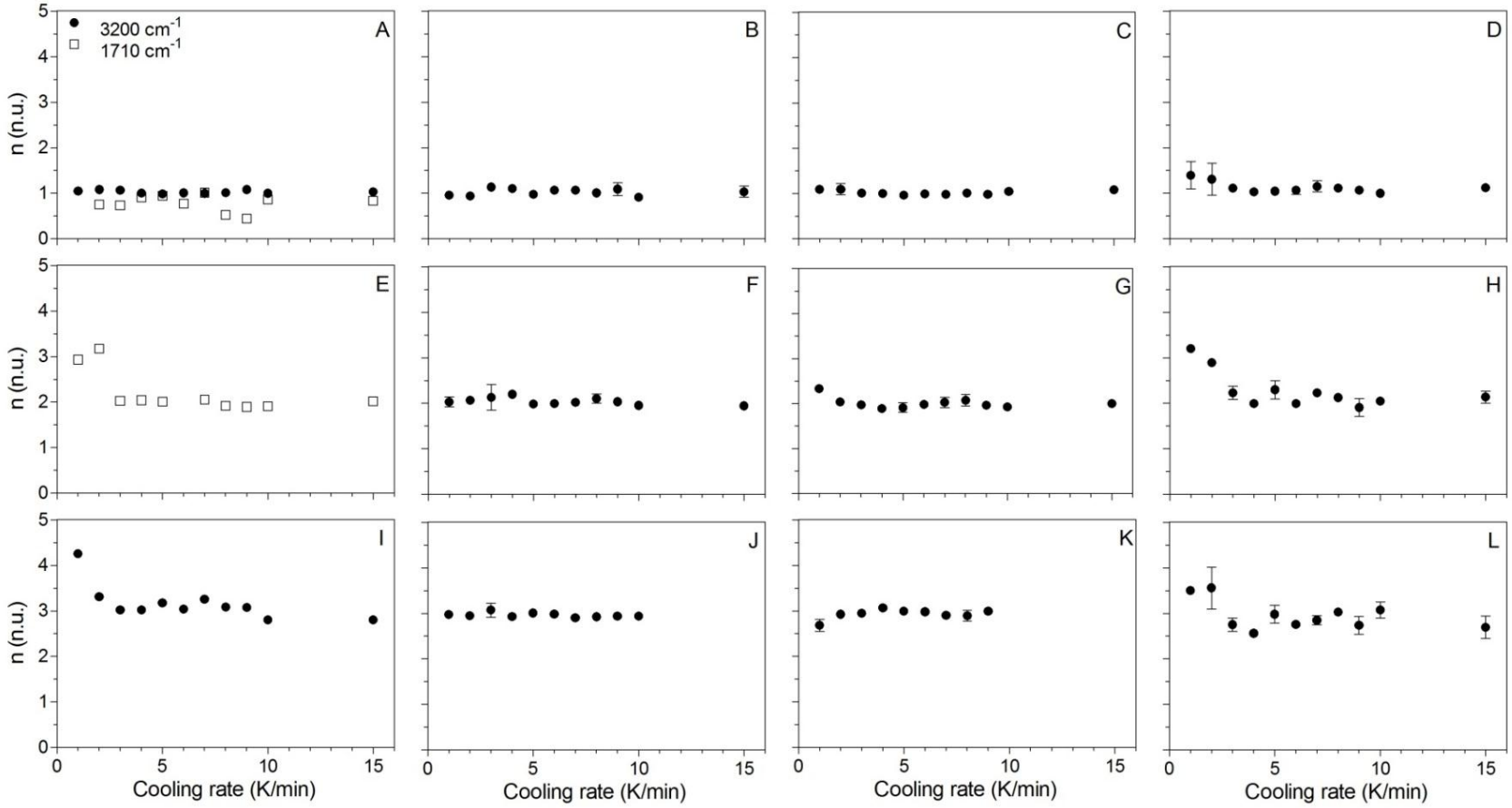

Figure 3.6: Avrami exponents (n) calculated from the fits of the experimentally observed data to the modified Avrami model for FT-IR (A, E and I), PLM (B, F, and J), DSC (C, G, and K) and rheology (D, H and L) for 12HSA (A-D), stearic acid (E-H) and trihydroxystearin (I-L).

The dimensionality of crystal growth from the Avrami exponents was also verified by the PLM micrographs taken when the sample reached the final temperature (Figure 3.1). The model was capable of determining the correct dimensionality of growth using DSC and PLM but the mode of nucleation was only detected under FT-IR.

The calculated induction times were compared for each method, cooling rate and sample (Figure 3.7). A comparison of the experimentally observed *versus* the calculated induction times was found to have less than 5% difference (data not presented). The induction time dictates whether a method can detect the onset of nucleation. The observed induction times were determined by the inflection point on the graphs for FT-IR, DSC and rheology. In FT-IR, the inflection point was determined based on the plot of the absorbance area over time. The inflection point for DSC was determined by the change in the integrated curve over time whereas in rheology it was based on the change in the storage modulus. For PLM, the observed induction time was based on the initial presence of nuclei observed under polarized light. The fitted induction times were determined using the modified Avrami model. At low cooling rates, the earliest induction time were detected by PLM and FT-IR while rheology and DSC occurred significantly later (Figure 3.7).

The induction time, determined using DSC, has a delayed onset due to the thermodynamics of nucleation which is a complex relationship between the decrease in entropy and release of enthalpy during nuclei formation (Walstra, 2003). At the early stages of crystallization, the heat released from the formation of the first few nuclei may not be captured by DSC (Piorkowska, Galeski, & Haudin, 2006) which makes it difficult to determine an accurate induction time. Rheology measures the elastic properties of the network which occur upon the formation of a continuous network significantly later than the onset of nucleation (Schwittay, Mours, & Winter, 1995; Winter, 1999). In trihydroxystearin and stearic acid, entanglement of the network does not occur as readily as 12HSA and hence a significantly lower G′ is observed. Both PLM and FT-IR determined the dimensionality of crystal growth while only FT-IR appeared to be sensitive to the mode of nucleation. Therefore the modified Avrami model is capable of not only determining the dimensionality of crystal growth but also the induction time.

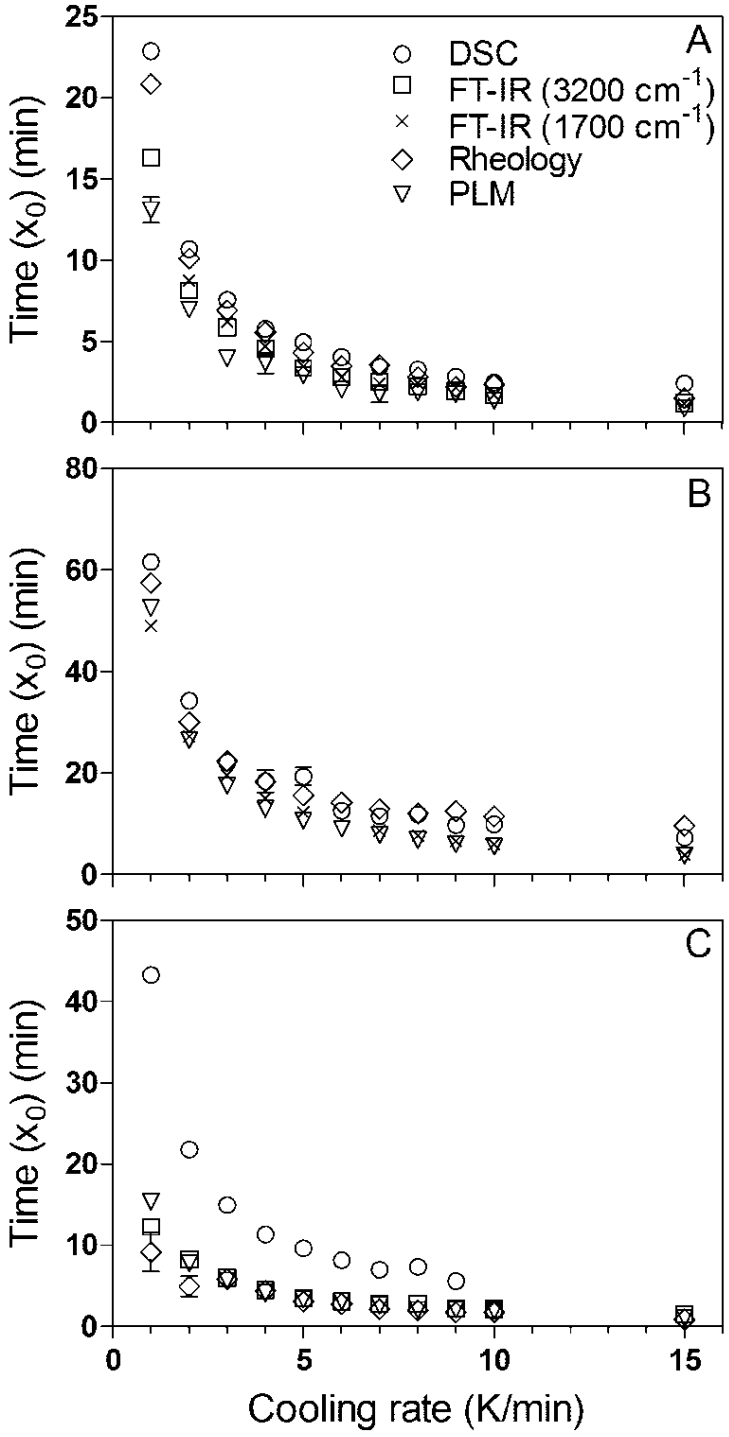

Figure 3.7: The induction times (x_0) of the fitted data for 12HSA (A), stearic acid (B) and trihydroxystearin (C).

The maximal signal, or maximum phase volume (Y_{max}), is also an important parameter in the modified Avrami model. While the induction time indicates when the first sign of the crystallization event is detected, Y_{max} indicates when the phase volume has reached its maximum at that given temperature. The observed Y_{max} *versus* the calculated Y_{max} was plotted for the different samples and cooling rates (Figure 3.8). The Y_{max} values obtained for the observed overlapped those that were calculated (Figure 3.8). This indicates that the model was capable of correctly fitting to the maximal measured change in the phase volume (Y_{max}). Though the maximal change in phase volume (Figure 3.8) and induction times (Figure 3.7) for the experimentally observed values correlated well with the fitted values, not all four of the methods used predicted good parameters for the modified Avrami model. In order to obtain an accurate Avrami exponent and rate constant, the method must be capable of detecting the early formation of nuclei. The inability for DSC to detect the heat released at early stages of crystallization leading to a delayed induction time invalidates it as a candidate to predict accurate parameters for the modified Avrami model. Though rheology also obtained a later induction time than other techniques (Figure 3.7), it was capable of detecting the transition prior to DSC. Rheology obtained a later induction time (Figure 3.7) and predicted fractional Avrami exponents which were not observed in the other methods (Figure 3.6D, H and L). For the aforementioned reasons, the data obtained by FT-IR and PLM were considered valid and further insights were gained by the apparent rate constants (k_{app}).

The apparent rate constants, k_{app}, were determined by fitting the data to the modified Avrami model (Figure 3.9). Under isothermal cooling conditions, as the crystallization temperature decreases, the crystallization rate constant increases (Avrami, 1939, 1940, 1941). Therefore, under non-isothermal crystallization conditions it is expected that the rate constant will increase as the cooling rate increases. Furthermore, when comparing the rate constants obtained by the two methods, an increase in cooling rate is accompanied by the increase in rate constant until a plateau is reached at higher cooling rates (Figure 3.9). This phenomenon may be explained by the two components of the rate constant: diffusion and reaction rates (Marangoni, 2005a). Diffusion limited reactions occur when the crystallization rate is limited by the molecules ability to diffuse

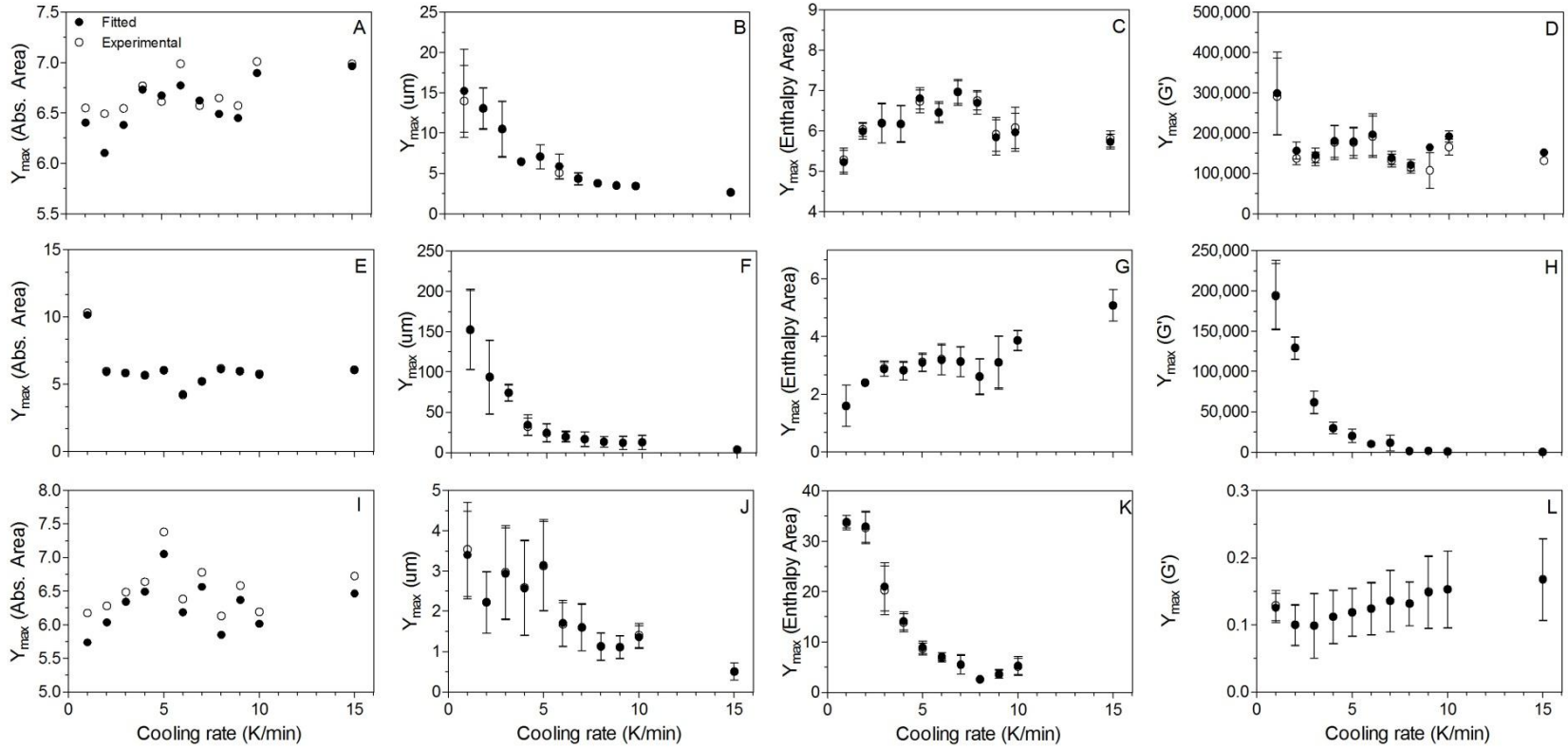

Figure 3.8: The maximal measure of the change in the phase volume (Y_{max}) as a function of cooling rate for the experimentally observed verses the fitted data to the modified Avrami model for FT-IR (A, E and I), PLM (B, F, and J), DSC (C, G, and K) and rheology (D, H and L) for 12HSA (A-D), stearic acid (E-H) and trihydroxystearin (I-L).

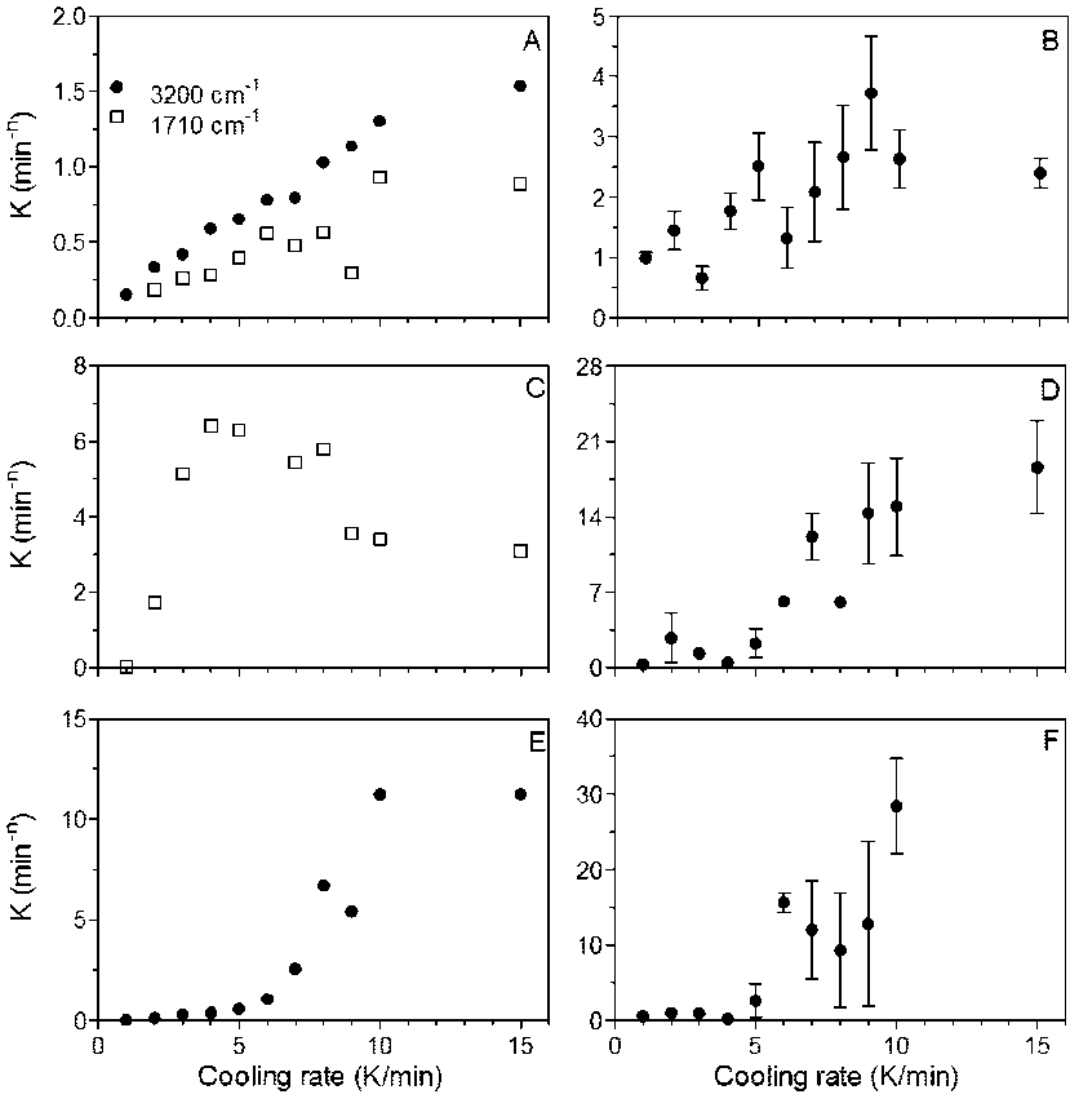

Figure 3.9: Apparent rate constants (k_{app}) obtained from the experimental fits of the data to the modified Avrami model for FT-IR (A, C, and E) and PLM (B, D, and F) for 12HSA (A-B), stearic acid (C-D) and trihydroxystearin (E-F).

to the crystal surface; while, reaction limited crystallization occurs when the rate of incorporation of the molecule into the crystal lattice is limited (Marangoni, 2005a). A dual trend was observed for the apparent rate constants (k_{app}) obtained below and above cooling rates of 5-7 °C/min. A steeper slope was observed among the lower regime of cooling rates whereas a shallower slope was observed for the upper regime. This dual trend observation is congruent with observations made by previously reported research (Rogers & Marangoni, 2008, 2009). Slow cooling profiles lead to crystallization being diffusion limited while at faster cooling rates crystallization is reaction limited (Bouzidi & Narine, 2010). A similar result was previously reported in non-isothermal cooling conditions for crystallization using the isoconversional technique (Bouzidi & Narine, 2010). Under low cooling rates, the thermodynamic driving force for crystallization is low allowing molecules near or at the crystal-solvent interface to orient before incorporating into the crystal lattice (Lam *et al.*, 2010; Marangoni, 2005a). Under high cooling rates, the thermodynamic driving force is high and the molecules lack the time to attain the optimal configuration before incorporation into the crystal lattice (Lam *et al.*, 2010; Marangoni, 2005a). This yields imperfectly formed crystals which was previously reported in the crystallization of 12HSA as branched fibres (Lam *et al.*, 2010).

3.6 Conclusions

The application of the modified Avrami model requires the data to be a measure only of the change in phase volume. When this criterion is not met, fractional Avrami exponents were obtained which invalidated the data. The experimental validation of the modified Avrami model relies on the model to accurately predict the Avrami exponent (n), induction time (x_0) and the maximal signal (Y_{max}). For all the data collected, the experimentally observed maximal signal (Y_{max}) and the induction time (x_0) corresponded well with the fitted parameters. An accurate Avrami exponent (n) requires that the experimental method capable of detecting early nucleation events. Both the PLM and FT-IR reported early induction times (x_0). Furthermore, FT-IR was the only method to determine the mode of nucleation and the dimensionality of crystal growth. This suggests that the FT-IR method is the most accurate method to characterize the non-

isothermal crystallization of materials providing insights into the apparent rate constant (k_{app}).

3.7 Study 1 in context of this thesis

Study 1 experimentally validates the use of the modified Avrami model to characterize crystallization under non-isothermal cooling conditions. Study 1 demonstrated that the modified Avrami model can be used under non-isothermal cooling conditions which fulfill the first objective in the introduction. This model may be used by the industry as a tool to determine how changes in the crystallization conditions affect the kinetics of the phase transition. Furthermore, this model was used in the second study to determine the rate limiting reaction for 12HSA fibre formation.

4. Study 2: A Molecular insight into the nature of crystallographic mismatches in self-assembled fibrillar networks under non-isothermal crystallization conditions.[2]

4.1 Abstract

The lengths of the 12-hydroxystearic acid (12HSA) fibres are influenced by crystallographic mismatches resulting from the incorporation of 12HSA monomers into the crystal lattice in an imperfect manner. On a molecular level, this can be differentiated using synchrotron Fourier transform infrared (FT-IR) spectroscopy by monitoring the change in area of the 1700 cm^{-1} and 3200 cm^{-1} peaks, corresponding, respectively, to the dimerization of the carboxylic acid groups and hydroxyl non-covalent interactions, during crystallization. The crystallographic mismatch is attributed to a plateau in the apparent rate constant for the dimerization of the carboxylic acid head groups while the hydroxyl interactions linearly increase as a function of cooling rate (ϕ). The rate constant for hydroxyl interactions linearly increases as a function of cooling rate while a plateau is observed for the rate of dimerization at cooling rates above 5 to 7 °C min^{-1}. At cooling rates greater than 5 to 7 °C min^{-1} 12HSA monomers do not effectively dimerize before being incorporated into the crystal lattice causing crystal imperfections impeding linear epitaxial crystal growth and produces branched fibres. At slow cooling rates (*i.e.*, less than 5 to 7 °C min^{-1}), long fibres are produced with a fractal dimension between 0.95 and 1.05 and for rapid cooling rates (*i.e.*, greater than 5 to 7 °C min^{-1}) short branched fibres are produced with a fractal dimension between 1.15 and 1.32.

4.2 Introduction

Fundamental research on molecular gels, capable of self-assembling into fibrillar networks, has primarily focused on structural and mechanical characterization of these

[2]Chapter 4 was published in: Soft Matter, (2010). 6(2), 404-408. DOI: 10.1039/b919477k – Reproduced by permission of The Royal Society of Chemistry (RSC) - http://pubs.rsc.org/en/content/articlelanding/2010/sm/b919477k

soft materials (Terech, 2009). This, in part, is due to the numerous, assorted applications of these complex systems including: drug delivery (Kang, Liu, Sawant, Ho, Chan, & Chan, 2005; Liang, Yang, Zhang, Li, Fan, Kuang, Gao, Wang, Lu, & Xu, 2009), tissue engineering (Xu, 2009), lipid structuring (Bot & Agterof, 2006; Bot, den Adel, & Roijers, 2008; Rogers *et al.*, 2009b) and scaffolding systems (Ajayaghosh, Praveen, Vijayakumar, 2008). To illustrate the structural significance of these materials in practical applications, such as drug delivery, the rate of release is a function of the bioseparation process. This separation process is directly related to the mesh size distribution of the network (Li, Liu, Wang, & Xiong, 2005; Rogers *et al.*, 2008b). Therefore, the ability to manipulate and control the rheological network properties of the desired gelator–solvent combinations is crucial in achieving the desired physical properties of these soft materials. Due to the importance of the rheological and network properties, the degree of branching and hence the mesh size distribution have been extensively examined under isothermal (Li *et al.*, 2009; Liu & Sawant, 2001, 2002a, 2002b) and non-isothermal conditions (Rogers & Marangoni, 2008, 2009). The diversity of the microscopic and mesoscopic structures of low molecular weight organogels makes them interesting soft materials with numerous theoretical and practical applications (Terech & Weiss, 1997).

Thermoreversible molecular gels are capable of aggregating upon cooling the organogelator–solvent melt below the gelators' melting point leading to the formation of a supersaturated state (Weiss & Terech, 2006). The supersaturated state (also termed supercooling or undercooling) is achieved *via* isothermal or non-isothermal cooling conditions. Supercooling (τ) has been defined under isothermal conditions as $\tau = (T^*-T_g)/T^*$ where T^* is the equilibrium temperature and T_g is the temperature of gelation (Li *et al.*, 2009). While for non-isothermal conditions the comparable supercooling-time exposure (β) term is defined as $\beta=(\Delta T_c)^2/\phi$ where ΔT_c is equal to T_m-T_c and T_m is the melting temperature, T_c is the crystallization temperature and ϕ is the cooling rate (Rogers & Marangoni, 2008, 2009). Cooling beyond the formation of the supersaturated state causes the gelator molecules to microscopically phase separate and self-assemble *via* stochastic nucleation events driven by enthalpic forces (Weiss & Terech, 2006). Following nucleation, crystal growth causes gelator molecules to

aggregate into a network forming rods, tubes, or sheets *via* non-covalent interactions. The aggregation process requires a meticulous balance between the contrasting parameters of solubility and those controlling epitaxial growth (Suzuki *et al*., 2003). Molecular gels contain fibres that form a 3-dimensional network interacting *via* transient and permanent junction zones (Wang, Liu, Xiong, & Li, 2006). Permanent junction zones are effective at entraining the liquid apolar phase in the mesh-like network arising because of crystallographic mismatches at the interface of the growing one-dimensional crystals, resulting in branch points and truncations along the fibre (Liu, 2005; Wang *et al.*, 2006).

Recent work by Liu has advanced the understanding on how these fibres can be engineered *via* the modification of the isothermal crystallization conditions of the gelator–solvent system (Li *et al.*, 2009). Liu has been instrumental in developing the theory on crystallographic mismatches used to model the branching and generation of permanent junction zones. Significant evidence has been provided to support the nucleation–growth–crystallographic mismatch branching (CMB) mechanism (Figure 4.1). The CMB method suggests that with low degrees of undercooling, following nucleation, the fibres grow one-dimensionally with little branching, interpenetration and entanglement (Wang *et al.*, 2006). At low degrees of bulk supersaturation, the crystallographic mismatch nucleation barrier (ΔG_B) is very high, favouring one dimensional fibre growth with a corresponding large correlation length (ξ) (Wang *et al.*, 2006). However, when the crystallization temperature is decreased an increase in the supersaturation causes the crystallographic mismatch barrier to be significantly reduced increasing the fibre tip branching (Wang *et al.*, 2006). The highly branched fibres (*i.e.*, short correlation length (ξ)) coincide with smaller pore sizes (Wang *et al.*, 2006). Recently, it has been shown that increased supercooling leads to more elastic gels due to the shorter branched fibres (Li *et al.*, 2009; Rogers *et al.*, 2008b). However, at this time, molecular evidence has not been provided to support or reject the theory of crystallographic mismatches and it is our aim to examine the crystallographic mismatch theory by examining the non-covalent interactions which allow the gelator molecules to assemble into fibrillar aggregates.

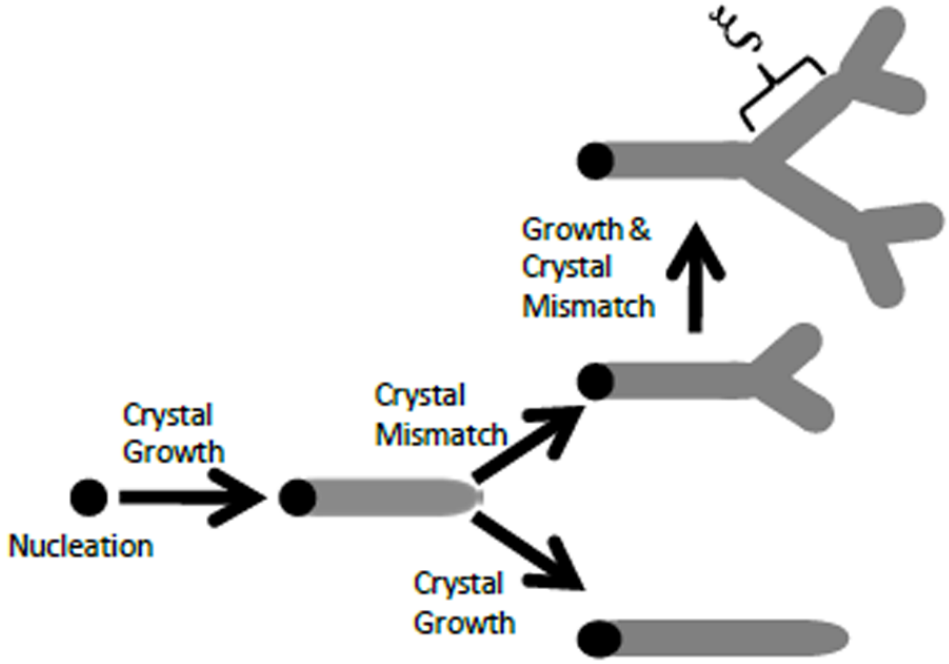

Figure 4.1: Nucleation and crystal growth mechanism using the crystallographic mismatch theory (Adapted from Li, *et al.*, 2009).

4.3 Methods

4.3.1 Sample Preparation

DL-12-Hydroxystearic acid was obtained from Nu-check Prep (Elysian, MN, USA) and heavy mineral oil was obtained from Sigma-Aldrich (Oakville, ON, CAN) and used as received. Two and a half (wt%) samples of 12HSA in mineral oil were prepared in triplicate by heating the 12HSA in heavy mineral to 90 °C for 30 min and stored at room temperature.

4.3.2 Polarized Light Microscopy

Polarized light micrographs were acquired using a Nikon Eclipse E400 light microscope equipped with a Nikon DS-FiL color camera and a long working distance 10X lens and condenser with a resolution of 2560 by 1920 pixels. Non-isothermal cooling conditions from 1 °C/min to 20 °C/min were carried out using a temperature controlled stage [LTS 120 and PE94 temperature controller (Linkam, Surrey, UK)]. Images were acquired when the system reached 30 °C. Fibre length was measured using the software Image J (Bethesda, Maryland, USA) where the number of pixels along a fibre was determined and calibrated to a 100 µm magnification bar imaged under the same conditions as the gels.

4.3.3 Small deformation Rheology

An AR 1000 rheometer (TA instruments, New Castle, DE) was used to probe the macroscopic properties of the materials during the formation of the network. A 4 cm flat steel parallel plate (TA Instruments, New Castle, DE) and a gap of 1000 µm were used to carry out the oscillatory measurements during crystallization. Small deformation oscillatory rheology was employed to monitor the evolution of the modulus (G*) as a function of time during controlled cooling rates at 1 Hz and 10 Pa. 10 Pa was chosen as the controlled stress because it is the lowest value obtained in the linear viscoelastic region (LVR).

4.3.4 Synchrotron Fourier Transform Infrared Spectroscopy

A drop of sample was placed between two CaF_2 optical windows (25 mm diameter, 2 mm thick) separated with a 15 µm Teflon spacer. The samples were then cooled on a Linkam LTS120 controlled temperature stage (Linkam, Surrey, United Kingdom) with cooling rates between 1 °C min^{-1} to 20 °C min^{-1}. Fourier transform infrared spectroscopy (FT-IR) spectra were collected using the end station of the mid-IR beamline (beamline 01B1-01, Canadian Light Source, Saskatoon, SK). The end station is comprised of a Bruker Optics IFS66v/S interferometer coupled to a Hyperion 2000 IR microscope (Bruker Optics, Billerica, MA, USA). Light is focused on the sample using a 15X magnification Schwarzschild condenser, collected by a 15X magnification Schwarzschild objective with the aperture set to a spot size of 40 µm by 40 µm and detected by a liquid nitrogen cooled narrowband MCT detector utilizing a 100 µm sensing element.

A KBr-supported Ge multilayer beamsplitter was used to measure spectra in the mid-infrared spectral region. Measurements were performed using OPUS 6.5 software (Bruker Optics, Billerica, MA). The measured interferograms were an average of 32 scans and were recorded by scanning the moving mirror at 40 kHz (in relation to the reference HeNe laser wavelength of 632.8 nm). The wavelength range collected was 690 to 7899 cm^{-1} with a spectral resolution of 4 cm^{-1}. Single channel traces were obtained using the fast Fourier transform algorithm, without any zero-filling, after applying a Blackman-Harris 3-Term apodization function. For single spectra, measurements' reference single channel traces were carried out in the molten state.

4.4 Results and Discussion

Figure 4.2 illustrates images of 2.5 wt% 12 hydroxystearic acid (12HSA) in mineral oil which produce a transparent gel when cooled below the melting point of the gelator. Figure 4.2A and B represent cooling rates of 1 and 4 $^{\circ}C\ min^{-1}$ which are subjected to a lesser degree of supercooling, Figures 4.2C and D represent cooling rates

of 7 and 20 °C min^{-1}. The faster cooling rates (Figures 4.2C and D) produced shorter fibres due to the presence of crystallographic mismatches. This corresponds well to

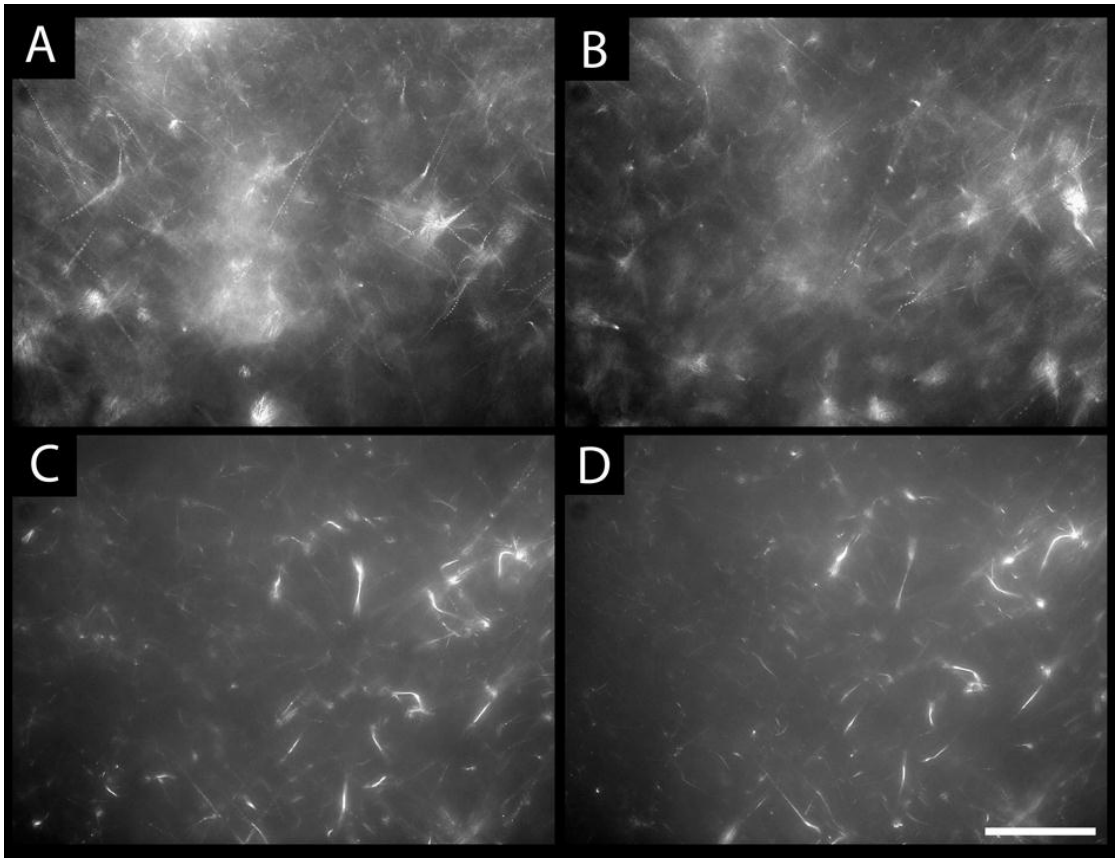

Figure 4.2: 2.5 wt% 12HSA in mineral oil organogels at 30°C cooled at 1°C/min (A), 4°C/min (B), 7°C/min (C) and 20°C/min (D). Magnification bar = 100 µm.

results observed by Liu, Chen, Liu, and Liou (2005), where they observed the formation of highly branched networks when isothermally cooled to 20 °C, while little branching was observed when isothermally cooled to 50 and 55 °C. In their system, they found that the correlation length (ξ) linearly decreased as a function of supercooling
((T* - T_g)/T*) until reaching a plateau where the fibre no longer decreases in length (ξ) (Li *et al.*, 2009). Under non-isothermal conditions the lengths of the fibres uninterrupted by crystallographic mismatches were measured (Figure 4.3). A similar trend was observed where the correlation length decreased

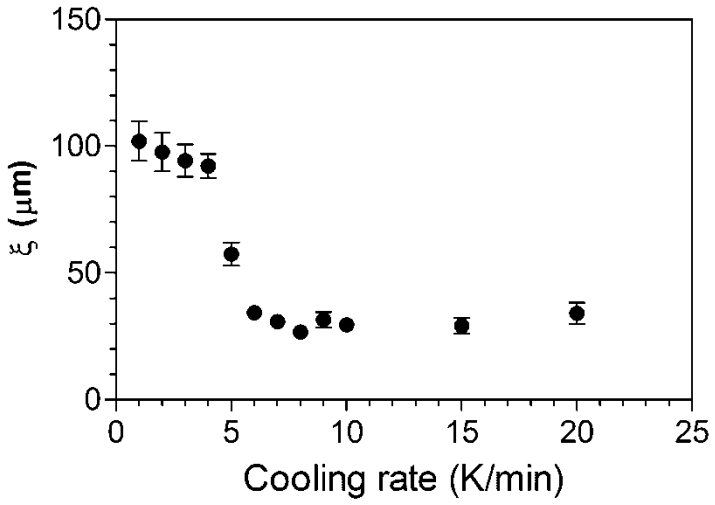

Figure 4.3: Correlation length (ξ) of 2.5 wt% 12HSA fibres in mineral oil measured from the micrographs obtained at 30°C after they had been cooled from 90°C at varying cooling rates.

linearly as a function of cooling rate between 1 °C min^{-1} and 4 °C min^{-1}. Cooling rates greater than 4 °C min^{-1} resulted in an abrupt change in the fibre length resulting in significantly ($p < 0.05$) shorter fibres. Previously, using a modified

Avrami equation for non-isothermal cooling conditions we illustrated that the length of fibres and rate of fibre growth have two linear regimes where the distinction is at approximately 5-7 °C min^{-1} (Rogers & Marangoni, 2008, 2009). It has been established that molecular self-assembly occurs *via* highly specific non-covalent interactions occurring *via* Liu's nucleation-growth-crystallographic mismatch-growth mechanism (Li *et al.*, 2009).

Typically crystal growth is thought of in integer values where fibres would be 1-dimensional, platelets would be 2-dimensional and spherulites would correspond to 3-dimensional growth. However, in many instances materials grow in a fractal or self-similar nature regardless of the length scale examined (Liu & Sawant, 2002b). Liu and Sawant (2002b) have developed a fractal rheological method for quantifying isothermal crystallization of organogels which originates from the Cayley tree network structure and the Avrami model leading to the following form:

$$\ln[1 - X_{cr}] = -k^o(t - t_g)^{D_f} \qquad \text{(eq. 4.1)}$$

where:

$$X_{cr}(t) = \frac{G^*(t) - G_0^*}{G^*(\max) - G_0^*} \qquad \text{(eq. 4.2)}$$

where G* is the modulus at a given time, G_o* is the initial modulus and G*(max) is the maximum modulus, k^o is a constant related to the growth rate, t is the time, t_g is the gelation time and D_f is the fractal dimension (Liu & Sawant, 2002b). Since the rheological fractal dimension is a measure of the solid network structure, the spatial distribution of the solid phase, the degree of branching and fibre-fibre interactions and not solely a measure of a solid phase volume, the assumptions which apply to the Avrami model do not hold. However, the fractal from is consistent with numerous other researchers and the exponent D_f derived from Liu's model is a function of the network structure. However, the fractal value is theoretically different from the exponent (n) in the Avrami model which is only correct if the physical attribute being measured is a function of the solid phase volume. D_f represents the dimensionality of crystal network growth while n from the Avrami

model incorporates not only the dimensionality of crystal growth but also the mode of nucleation.

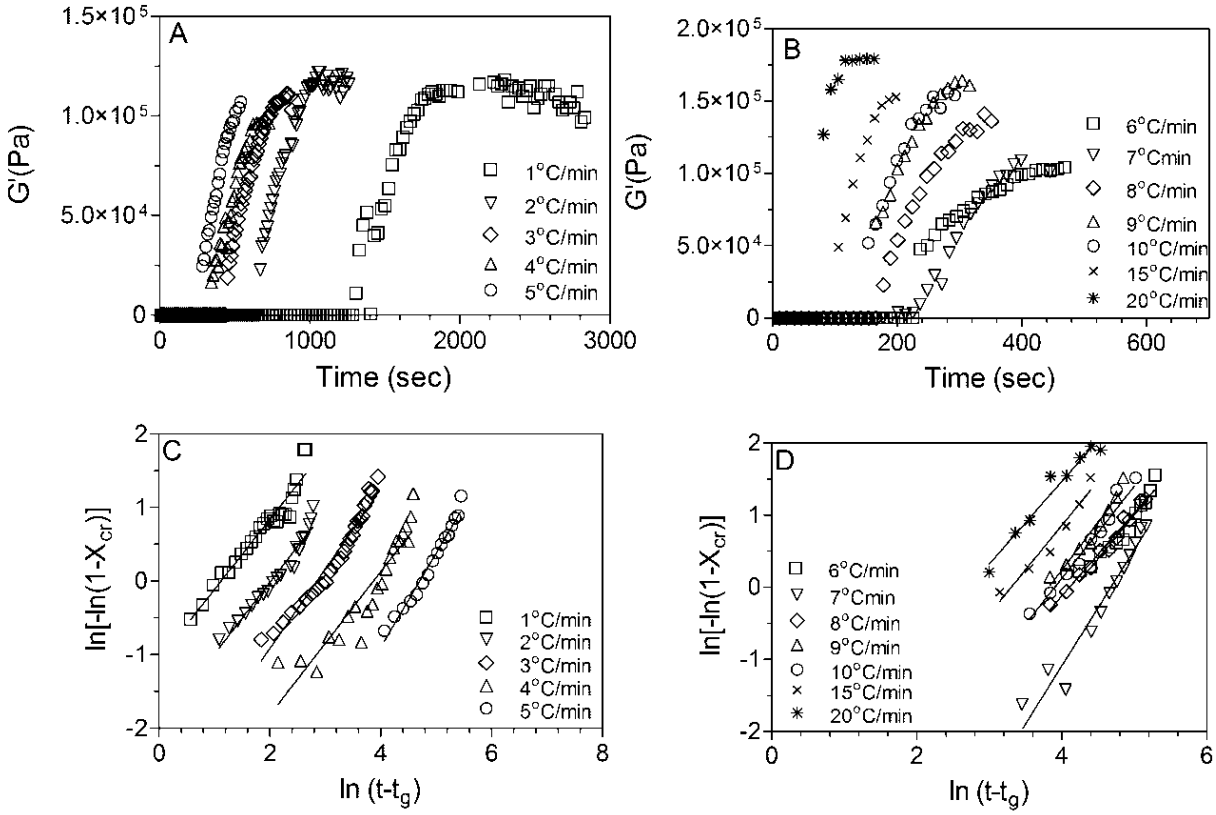

Figure 4.4: The evolution of G* as a function of time during gelation under non-isothermal conditions for slow cooling rates (A) and fast cooling rates (B). The dependence of $\ln[-\ln(1-X_{cr})]$ on $\ln(t-t_g)$ to determine the fractal values under different non-isothermal cooling profiles (C and D). Data was shifted to prevent overlap (C).

Table 4.1: Dependence of the average fractal dimension and the standard deviation using non-isothermal cooling rates determined using small deformation rheology.

Cooling rate (°C/min)	1	2	3	4	5	6	7	8	9	10	15	20
D_f	0.95 ± 0.05	0.98 ± 0.05	1.08 ± 0.04	0.97 ± 0.08	1.28 ± 0.06	1.22 ± 0.10	1.31 ± 0.06	1.15 ± 0.05	1.32 ± 0.11	1.28 ± 0.10	1.23 ± 0.14	1.15 ± 0.10

Rheological data was collected (Figure 4.4A and B) and transformed using these equations to calculate the fractal dimension for 12HSA under different non-isothermal conditions (Figure 4.4 C and D). It was observed that the fibres which developed under slow cooling rates had longer correlation length (Figure 4.3) and similar fractal values (Table 4.1). For long one-dimensional fibres (*i.e.*, cooling rates less than 4 °C min^{-1}) the corresponding fractal values were of between 0.95 and 1.08 indicating "fibre-like" growth. At accelerated cooling rates (i.e, cooling rates greater than 5 °C min^{-1}) there is an increase in the fractal value between 1.15 and 1.32. This would indicate that the fibres are becoming less linear and coincide with a greater degree of branching. Using both the correlation length determined *via* microscopy (Figure 4.3) and the fractal dimension determined by rheology (Figure 4.4 and Table 4.1) it is obvious that cooling rates greater than 5 °C/min result in crystallographic mismatches. Therefore, it is assured that these branch points are a result of a crystallographic mismatch or an imperfect interaction between 12HSA molecules resulting in branched networks. Hence to observe our hypothesis that hydrogen bonding is affected during crystallographic mismatches we employed FT-IR spectroscopy using synchrotron radiation.

12HSA develops fibres by two monomers dimerizing between carboxylic acid groups and longitudinal growth occurs *via* hydrogen bonding between the hydroxyl groups at carbon 12. Therefore, we can monitor these spectral features using FT-IR (Figure 4.5A and B). The dimerization of 12HSA may be observed *via* a shift in the spectral features due to the carboxylic acid stretch shifting from 1710 cm^{-1} to 1700 cm^{-1} (Lin-Vien *et al.*, 1991). During assembly of 12HSA, the spectra were recorded as a function of time for each cooling rate. As the system assembles there is a decrease in the absorbance at 1710 cm^{-1} corresponding to an increase at 1700 cm^{-1} indicating that 12HSA molecules are forming dimers. Similarly, hydrogen bonding was monitored for the hydroxyl groups which is observed as an increase in the area of the peak at position 3200 cm^{-1} (Figure 4.5A and B) (Lin-Vien *et al.*, 1991). The area under the peaks at 1700 cm^{-1} and 3200 cm^{-1} were measured and plotted as a function of time while undergoing non-isothermal cooling.

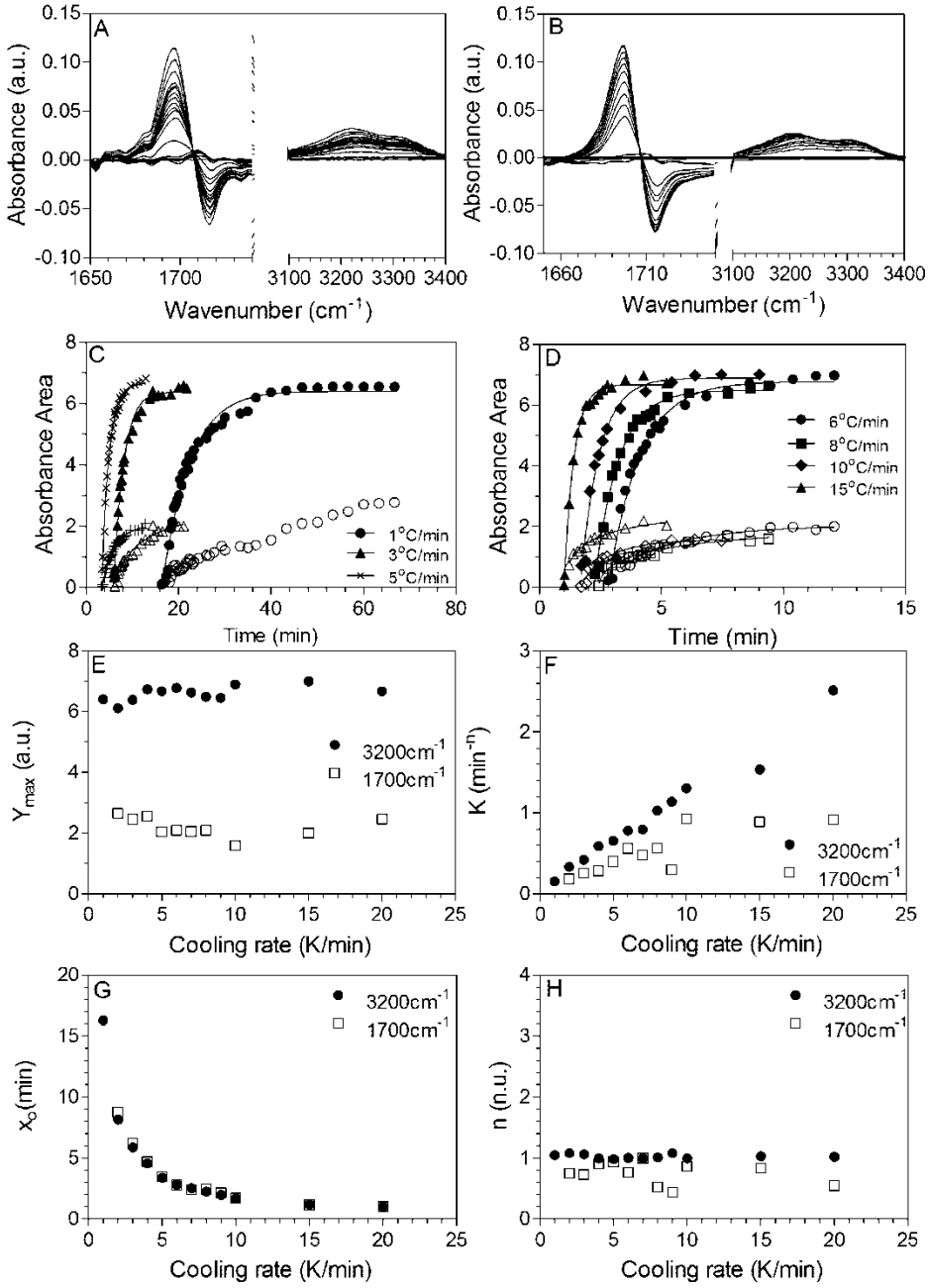

Figure 4.5: Differential FT-IR spectra of 12HSA assembly during slow cooling at 1°C/min and was collected from 90°C to 30°C over a 60 min period (A) and fast cooling at 10°C/min from 90 to 30°C over a 6 min period (B) non-isothermal cooling profiles. Integration of the FT-IR spectra (C and D) to determine the area under the spectral features of interest (Filled symbols represent absorbance at 3200 cm^{-1} and open symbols represent the absorbance at 1700 cm^{-1}). Avrami constants are determined by fitting the integrated area verses time to obtain maximum signal (E), apparent rate constant (F), induction time (G) and dimensionality of growth (H).

To assess if any changes in the rate of evolution between these two peaks were observed the modified Avrami model was applied which has been previously reported as (Rogers & Marangoni, 2008, 2009):

$$Y = Y_{max}(1 - e^{-k_{app}(x-x_o)^n}) \quad \text{(eq. 4.3)}$$

where Y is the area under the peak at 1700 cm^{-1} or 3200 cm^{-1} (Figure 4.5C and D), Y_{max} is the maximum area of the corresponding peaks, k_{app} is the apparent rate constant for non-covalent interactions (*i.e.*, hydrogen bonding), x is the time, x_o is the induction time and n is the dimensionality of growth. In previous work, we had confined n to be equal to two because light microscopy indicated sporadic nucleation and one-dimensional growth (Rogers & Marangoni, 2008, 2009). However, the Avrami model was fitted by giving an initial value of n equals two, k_{app} and x_o equal to zero and Y_{max} is set to the maximum absorbance observed. The graphs were fitted using Graph Pad Prism 6.0 and an iterative process (1000 iterations) was used to fit the growth curves. The coefficient of determination (R^2) for all fits were greater than 0.98. Upon fitting with the Avrami model, it was observed that regardless of the cooling rate, similar intensities of the peak area was measured meaning no significant differences were observed in the intensity of the signal (Figure 4.5E). An exponential decrease in the induction time was observed as a function of cooling rate which has been previously reported (Figure 4.5G) (Rogers & Marangoni, 2008, 2009). The Avrami model suggests that for all cooling rates, the dimensionality of crystal growth is instantaneous nucleation and linear 1-dimensional growth corresponding to an Avrami exponent of n = 1 (Figure 4.5H) (Lin-Vien *et al.*, 1991). However, examining the apparent rate constant of hydrogen bond formation between the 12HSA carboxylic acid groups and between the hydroxyl groups we have a new insight into self-assembly and to crystallographic mismatches (Figure 4.5F). It has been previously mentioned that branched fibres result from molecules being incorporated into the lattice in an imperfect manner. This would suggest that there is a significant decrease in the rate of hydrogen bonding above 5 °C min^{-1} which corresponds to the significant change in fibre length (Figure 4.2). It was astounding to observe that the rate of hydroxyl hydrogen

bonding changes linearly with cooling rate, and does not plateau as the cooling rate increased. However, it was observed at cooling rates greater than 5-7 °C min^{-1} that the rate of dimerization between carboxylic acid groups plateaued (Figure 4.5F). This suggests that the crystallographic mismatch for 12HSA is a result of the inability of 12HSA monomers to effectively dimerize at faster cooling rates. When incorporated into the crystal lattice, monomers prevent the uninterrupted longitudinal growth observed at slower cooling rates.

4.5 Conclusions

When low molecular weight organogelators self-assemble into fibrillar networks they require highly specific non-covalent interactions. Upon large degrees of supercooling, *via* isothermal or non-isothermal cooling, the fibres undergo crystallographic mismatches resulting in higher fractal networks ($D_f \sim 1.2$) affecting the hardness and the ability of the network to retain the solvent. For 12HSA, cooling rates faster than 5 °C min^{-1} result in short fibres while for slower cooling rates longer fibres result with lower fractal values ($D_f \sim 1.0$). FT-IR spectroscopy revealed that nucleation for 12HSA is instantaneous while the crystallographic mismatch is a result of the rate of dimerization between carboxylic acid groups and not hydroxyl interactions.

4.6 Study 2 in context of this thesis

Crystallographic mismatches in 12HSA fibres cause branching points to form which affect the properties of the resulting network such as mesh size. Changes in mesh size due to changes in the processing conditions have been reported to affect the ability of the network to entrain oil (Rogers *et al.*, 2008a, 2008b). Study 2 fulfills the second objective of three as stated in the introduction by determining why crystallographic mismatches occur in 12HSA. Study 2 revealed that FT-IR analysis using the modified Avrami model can be employed to determine rate limiting reactions during the crystallization process. FT-IR analysis determined that carboxylic acid dimerization was the rate limiting reaction for 12HSA longitudinal fibre growth.

5. Study 3: Activation Energy of Crystallization for Stearic Acid Containing Molecules under Non-Isothermal Cooling Conditions

5.1 Abstract

The nucleation activation energy under non-isothermal cooling conditions was determined for 12-hydroxystearic acid (12HSA) (1-D crystals), stearic acid (2-D crystals), and trihydroxystearin (3-D crystals). The relative nucleation rate of trihydroxystearin and stearic acid were inversely proportionate to the supercooling-time trajectory parameter (β), while 12HSA was linearly proportionate to β. The differences in the proportionately to β is attributed to microscopic *versus* macroscopic phase separation. This suggest that both stearic acid and trihydroxystearin follow a probability density function for the number of molecules which crystallize as a function of supercooling (*i.e.*, the greater the cooling rate the greater the number of molecules which are incorporated into the crystal lattice). On the other hand, 12HSA molecules all crystallize when supercooled. The activation energy for stearic acid, 12HSA, trihydroxystearin and triglycerides were 1.52 kJ/mol, 5.40 kJ/mol, 7.87 kJ/mol and 24.80 kJ/mol; respectively. The activation energy is partly affected by the polarity of the crystallizing molecules relative to the solvent. As the relative polarity of the crystallizing molecules increases the activation energy decreases. However, this was not always observed because the activation energy for stearic acid was less than 12HSA. Therefore, the activation energy is not only a function of the molecular polarity but also due to the specific interaction between the nucleating molecules. The specific interaction affects the ability of the polar regions of the molecule to phase separate from the apolar solvent. As 12HSA and stearic acid dimerize the carboxylic acid regions of the molecule are shielded from the solvent but, 12HSA cannot effectively shield the hydroxyl groups from the crystalline surface resulting in a higher interfacial tension and thus a higher activation energy.

Chapter 5 has been recently accepted to be published into Crystal Growth & Design 11 (2011) 3593-3599.

5.2 Introduction

Often, crystallization is thought to occur in three-dimensional (3-D) space whereby spherulitic aggregates result and minimize the surface area to volume ratio and interfacial tension (Marangoni, 2005a). However, recent advances in crystal physics have thrust low-dimensionality crystals (*i.e.*, two-dimensional (2-D) platelets and one-dimensional (1-D) fibres) into the forefront of numerous fields including pharmacology (Liu *et al.*, 2005; Qian, Tao, Desikan, Hussain, & Smith, 2007; Tiberg & Johnsson, 2011), medicine (Bianco, Kostarelos, & Prato, 2005; Duncan, 2007; Moghimi, Hunger, & Murray, 2005) and nano-materials (Bruchez, Moronne, Gin, Weiss, & Alivisatos, 1998; Hosono, Fujihara, Honna, & Zhou, 2005; Rosenflanz, Frey, Endres, Anderson, Richards, & Schardt, 2004). Currently, there is a limited understanding on how these molecules nucleate and form supramolecular aggregates which no longer minimize the surface area of the crystal (Rogers & Marangoni, 2008).

It has been well established that changes to the crystallization conditions greatly affect the mechanical properties, flow behaviour and the supramolecular structure of materials regardless of the dimensionality of crystal growth (Hartel, 2001; McClements & Decker, 2008). For example, increasing the cooling rate, increases the number of nuclei, decreases the crystal size, modifies the polymorphism, and crystal imperfection (Lam *et al.*, 2010; Lam & Rogers, 2010). The thermodynamic conditions during nucleation and crystal growth dictate the structures formed by 12HSA, stearic acid and trihydroxystearin crystals (Lam and Rogers, 2010). At high cooling rates, highly branched networks are formed in 12HSA due to crystallographic mismatches, while at low cooling rates, large aggregates with few branching points are formed (Lam *et al.*, 2010). In industrial applications, crystallization often occurs under non-isothermal crystallization conditions where the temperature changes as crystallization progresses (Marangoni *et al.*, 2006a, 2006b). Understanding how nucleation and crystallization occurs under non-isothermal cooling conditions is of paramount importance.

Three systems, 12HSA, stearic acid and trihydroxystearin were chosen to be modeled to determine the activation energy of nucleation due to their molecular similarities and different dimensionalities of crystal growths. Upon crystallization,

12HSA form 1-D nanofibres (Huang & Weiss, 2007; Iwanaga *et al.*, 2010; Li *et al.*, 2009; Rogers & Marangoni, 2008, 2009; Rogers *et al.*, 2009a; Tachiban & Kambara, 1968), stearic acid form 2-D platlets (Gandolfo *et al.*, 2004; Schaink *et al.*, 2007; Swamy *et al.*, 1985) and trihydroxystearin form 3-D spherulitic crystals (Hackeng *et al.*, 2000; Lam & Rogers, 2010).

Traditionally, nucleation is studied under isothermal cooling conditions due to the ease of experimental design and application of theoretical models. The activation energy for nucleation may be determined under non-isothermal cooling conditions using a supercooling-time trajectory parameter (β) (Marangoni, Aurand, Martini, & Ollivon, 2006; Marangoni, Tang, & Singh, 2006). β describes the amount of supercooling experienced by a system during crystallization (Marangoni *et al.*, 2006a, 2006b). Polarized light microscopy (PLM) is utilized to visualize the number of nucleation sites formed as a function of time (Marangoni *et al.*, 2006a, 2006b). The number of nucleation sites is used to determine the dependence of β to nucleation rate (J) and may be used to calculate the activation energy (E_a) of a system (Marangoni *et al.*, 2006a, 2006b). The supercooling-time-trajectory parameter, β, takes into account both the time and the temperature or the amount of supercooling experienced by the material during crystallization (Marangoni *et al.*, 2006a, 2006b). Effectively, β is represented by the area under the temperature-time curve experienced by the material cooled at a specific rate (Marangoni *et al.*, 2006a, 2006b):

$$\beta = \frac{1}{2}\Delta T_c t_c \qquad \text{(eq. 5.1)}$$

where ΔT_c is the supercooling experienced by the system (*i.e.* the temperature difference between the melting temperature and the temperature at which the first crystal appears) and t_c is the time required to go from the melting temperature to the appearance of the first nucleus. Equation 5.1 may be rewritten if the system is cooled at a cooling rate ($\phi = \Delta T_c / t_c$) (Marangoni *et al.*, 2006a, 2006b):

$$\beta = \frac{1}{2}\left(\frac{\Delta T_c^{\,2}}{\phi}\right) \qquad \text{(eq. 5.2)}$$

For triacylglycerides (TAGs) an exponential scaling relationship is empirically observed between β and the nucleation rate (J) (Marangoni *et al.*, 2006b):

$$\frac{J}{J_{max}} = e^{-k\sqrt{\beta}} \quad \text{(eq. 5.3)}$$

combining equation 5.2 and equation 5.3, reveals the relationship between the nucleation rate and the cooling rate (Marangoni *et al.*, 2006a):

$$\frac{J}{J_{max}} = e^{-k(\Delta T_c/\sqrt{2\phi})} \quad \text{(eq. 5.4)}$$

equation 5.4 may be rewritten to include the activation energy parameter (Marangoni *et al.*, 2006a). Previously, it has been reasoned that the activation energy is the heat removed from the system between the melting temperature and the appearance of the first nucleus (Marangoni *et al.*, 2006a). This heat removed (Q_m) is the specific heat (C_p) of the system which is $Q_m=C_p\Delta T$ (Marangoni *et al.*, 2006a). Here, C_p is ~2.0 J g^{-1} K^{-1} for lipid based molecules (Marangoni *et al.*, 2006a). Therefore, it is possible to substitute Q_m/C_p for ΔT in equation 5.4 and to obtain the following relationship (Marangoni *et al.*, 2006a):

$$\frac{J}{J_{max}} = e^{-k(Q_m/C_p\sqrt{2\phi})} = e^{-(Q_m/Z\sqrt{\phi})} = e^{-(X/\sqrt{\phi})} \quad \text{(eq. 5.5)}$$

Q_m represents the activation energy for nucleation per unit mass (J/g), and Z (J g^{-1} $K^{-1/2}$ $s^{1/2}$) represents:

$$Z = \frac{\sqrt{2}C_p}{k} \quad \text{(eq. 5.6)}$$

the terms Z and X can be determined by the exponential fits of the relative nucleation rate (J/J_{max}) versus β or ϕ. It is possible to determine the activation energy for nucleation by calculating$Q_m = Z \times X \ [J/g]$. This model has been adapted to account for molecules requiring negligible supercooling before nucleation, such as 12HSA, by applying a Taylor expansion to the probability density function (Rogers & Marangoni, 2009). The probability density function (pdf) makes it possible to explain nucleation kinetics in a statistical manner by utilizing the kinetic theory of gases (Rogers &

Marangoni, 2009). In order to demonstrate the argument logically, the kinetic theory of gases is reviewed (Rogers & Marangoni, 2009).

The rate of reaction (v) is determined by the number of molecules with enough energy to overcome the energy barrier for the reaction (N*) (Rogers & Marangoni, 2009). Therefore $v=k_n[N^*]$, where k_n is the rate constant for the reaction and N* corresponds to the concentration of molecules in the activated state (Rogers & Marangoni, 2009). In gases, N* are the molecules with sufficient energy and proper orientation which are capable of undergoing the reaction (Rogers & Marangoni, 2009). In nucleation, N* are the molecules in the metastable state prior to the nucleation event (Rogers & Marangoni, 2009). The proportion of molecules that may nucleate is given by $(N^*)=p(x)(N_T)$, where N_T is the total concentration of molecules in a system and p(x) is the pdf that describes the frequency distribution of the particular event (Rogers & Marangoni, 2009). The pdf approach was first developed when the relative nucleation rate (J/J_{max}) was found to be exponentially dependent on $\sqrt{\beta}$ (Rogers & Marangoni, 2009). Therefore, if the rate constant for nucleation (k_n) is greater than zero, the exponential pdf, $p(\sqrt{(\beta)};k_n)$ is of the form (Rogers & Marangoni, 2009):

$$p\left(\sqrt{\beta};k_n\right)=\begin{Bmatrix} ke^{-k\sqrt{\beta}};\ \sqrt{\beta}\geq 0 \\ 0\quad ;\ \sqrt{\beta}<0 \end{Bmatrix} \qquad \text{(eq. 5.7)}$$

This pdf applies to the randomly distributed variable belonging to the set $\sqrt{\beta}\in[0;\infty)$ (Rogers & Marangoni, 2009). Therefore this pdf is appropriate to describe non-isothermal nucleation kinetics (Rogers & Marangoni, 2009).

The lower activation energy for 12HSA compared to triglycerides is due to microscopic phase separation in 12HSA compared to the macroscopic separation in TAGs (Rogers & Marangoni, 2008, 2009). This is partially due to the increased polarity of 12HSA which facilitates the formation of a nucleus by allowing 12HSA to dimerize with relative ease (Rogers & Marangoni, 2008). Therefore, smaller critical nuclei are required when going from a crystal embryo to a stable nuclei (Rogers & Marangoni, 2008). The nucleation behaviour is also dependent on the solvent employed (Rogers & Marangoni, 2009). Not only does the solvent polarity play a crucial role in the

activation energy but so does the ability of the solvent to interact with the crystallization molecules (Rogers & Marangoni, 2009). Therefore, solvent-gelator interactions greatly affect the nucleation behaviour and structural features of the crystals formed.

The aim of this study is to examine the role of molecular structure on the activation energy of nucleation. It is hypothesized that as the polarity of the crystallizing molecule increases the activation energy will decrease. The increased chemical potential may facilitate phase separation and generation of crystal embryos. It is predicted that under non-isothermal crystallization, that triglycerides will have a higher activation than trihydroxystearin while stearic acid will have a higher activation energy than 12HSA.

5.3 Materials and Methods

Stearic acid (Sigma Aldrich, Oakville, ON) and trihydroxystearin (Nu-Chek Prep, Elysian, MN, USA) were purchased and used as received. Two and a half percent (wt%) samples were added to heavy mineral oil (Sigma Aldrich, Oakville, ON, CA) and melted at 90 °C for 30 min to erase crystal memory. Cooling rates between 1-10 °C/min were done every 1 °C/min increments, as well the following cooling rates were also utilized: 0.5, 1.5, 2.5, 15 and 20 °C/min were utilizied to cool the samples to 30 °C.

5.3.1 Polarized Light Microscopy

A Nikon Eclipse E400 light microscope equipped with a Nikon DS-FiL color camera and a long working distance 10x lens and condenser (Nikon Instruments Inc., Melville, NY, USA) were used to acquire polarized light micrographs (PLMs) and brightfield micrographs. A temperature controlled stage [LTS120 and PE94 temperature controller (Linkam, Surrey, UK)] was used to control the cooling rates. The image resolution was 2560 by 1920 pixels. Images were analyzed using Adobe Photoshop Extended CS4.0 (Adobe Systems Incorporate, San Jose, CA, USA) to count for the number of crystals on each micrograph. Sample preparation consisted of applying a drop of the melted sample onto a glass microscopy slide. A cover slip was not applied to avoid crystallization in a confined environment. The samples were imaged as the sample was cooled.

5.3.2 Differential Scanning Calorimetry

A Q2000 Differential Scanning Calorimeter (DSC) (TA Instruments, New Castle, Delaware, USA) was used to determine the enthalpy of phase transition and the melting point. 8-10 mg of sample was hermetically sealed in aluminum pans and thermograms were collected as the sample was first heated to 90 °C and isothermally held for 30 min to erase the crystal memory. Then the samples were cooled down at 3 °C/min to a final temperature of 30 °C to capture the exothermic phase transition. TA analysis software (TA Instruments, New Castle, Delaware, USA) was used to integrate the transition associated with crystallization to determine the enthalpy. The onset of crystallization was determined by the observable inflection point on the collected thermograms.

5.4 Results and Discussion

The crystallization behaviour of a material is sensitive to the cooling rate (Chapman, 1962; Lam and Rogers, 2010; Li *et al.*, 2009; Rogers & Marangoni, 2008; Sato, 1999; Sato, Ueno, & Yano, 1999; Timms, 1984) , such that rapid cooling increases the degree of supercooling (*i.e.*, the crystallization temperature (T_c)) increases the thermodynamic driving force. PLM and brightfield micrographs were utilized to visualize the crystal morphology, number of crystals and crystal size (Figures 5.1 and 5.2). Trihydroxystearin crystallized as 3-D spheres (Figure 5.1G-I and 5.2G-I), stearic acid crystallized as 2-D platelets (Figure 5.1D-F and 5.2D-F) and 12HSA formed 1-D crystals (Figure 5.1A-C and Figure 5.2A-C). Rapid cooling rates resulted in more nuclei to act as crystal growth sites (Figure 5.3) and smaller crystals (Figure 5.2).

The crystallization process may be monitored by counting the number of nuclei present over time on the micrographs and plotting the number of nuclei *versus* time (Figure 5.3). The first derivative of the number of nuclei versus time ($\partial n/\partial t$) was taken to produce the rate of nucleation *versus* time (Figure 5.4). The rate of nucleation *versus* time (Figure 5.4) allows the maximum rate for nucleation to be determined for each cooling rate (Figure 5.3). From figure 5.4, a theoretical maximum nucleation rate (J_{max}) may be determined by fitting the nucleation rate (J) with its corresponding supercooling-

time trajectory parameter (β) to an exponential decay function. J_{max} corresponds to the intercept when β is zero (Marangoni *et al.*, 2006a, 2006b). Utilizing the J_{max}, J can be normalized and plotted as a function of both β and $\phi^{-0.5}$ (Figure 5.5) (Marangoni *et al.*, 2006a, 2006b; Rogers & Marangoni, 2008, 2009).

Stearic acid (Figure 5.5C-D) and trihydroxystearin (Figure 5.5E-F) were found to be inversely proportionate to β and $\phi^{-0.5}$. This inverse relationship was previously observed for triglycerides (Marangoni *et al.*, 2006a, 2006b). Previous data for 12HSA in the same solvent (Figure 5.5A and B) indicates that two distinct regions exist with differing sensitivities to the cooling rate (*i.e.*, above and below cooling rates of 5-7 °C/min) (Rogers & Marangoni, 2008, 2009). Below 5-7 °C/min, no observable dependence between cooling rate and nucleation rate was observed (Rogers & Marangoni, 2008, 2009). Therefore, the nucleation rate below 5-7 °C/min is a function of the mass transfer of crystallizing molecules to the nucleus (Rogers & Marangoni, 2008, 2009). Above 5-7 °C/min, the rate of nucleation is dependent on the cooling rate indicating that the rate crystallization is driven by a time-dependent thermodynamic driving force and not mass transfer (Rogers & Marangoni, 2008, 2009). Utilizing the scaling relationships between J_{max} *versus* β and J_{max} *versus* $\phi^{-0.5}$, it is possible to determine the activation energy for these systems using a statistical approach (Marangoni *et al.*, 2006a, 2006b; Rogers & Marangoni, 2008, 2009).

Polarity of these compounds in descending order is 12HSA, stearic acid, trihydroxystearin, and TAGs. Thus, our original hypothesis would suggest that the activation energy from lowest to highest should be in the same order. The activation energies for stearic acid and trihydroxystearin and were calculated to be 2.12 kJ/mol and 7.87 kJ/mol, respectively. The activation energy for triglycerides and 12HSA were previously reported as 24.8 kJ/mol (Marangoni *et al.*, 2006b) and 5.40 kJ/mol (Rogers & Marangoni, 2009), respectively. In general, the activation energy was strongly affected by the polarity of the crystallizing molecule; however, the one exception was the lower activation energy for stearic acid compared to 12HSA. This result is counter-intuitive to our original hypothesis where 12HSA was predicted to have the lowest activation energy. As the relative polarity of the crystallizing molecules increased, the driving

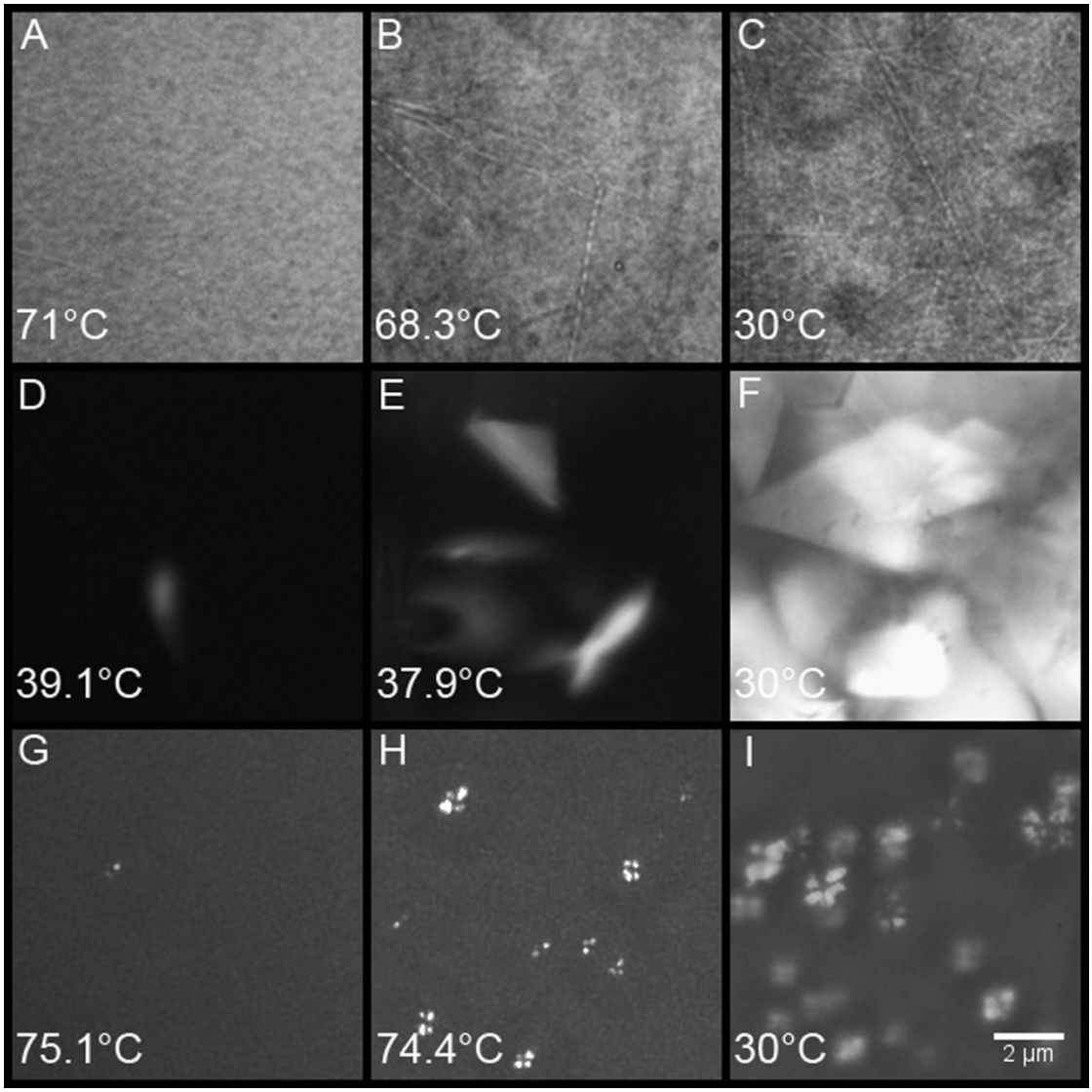

Figure 5.1: Brightfield micrographs of 12HSA (A-C), polarized light micrographs of stearic acid (D-F) and trihydroxystearin (G-I) in mineral oil cooled at 1 °C/min.

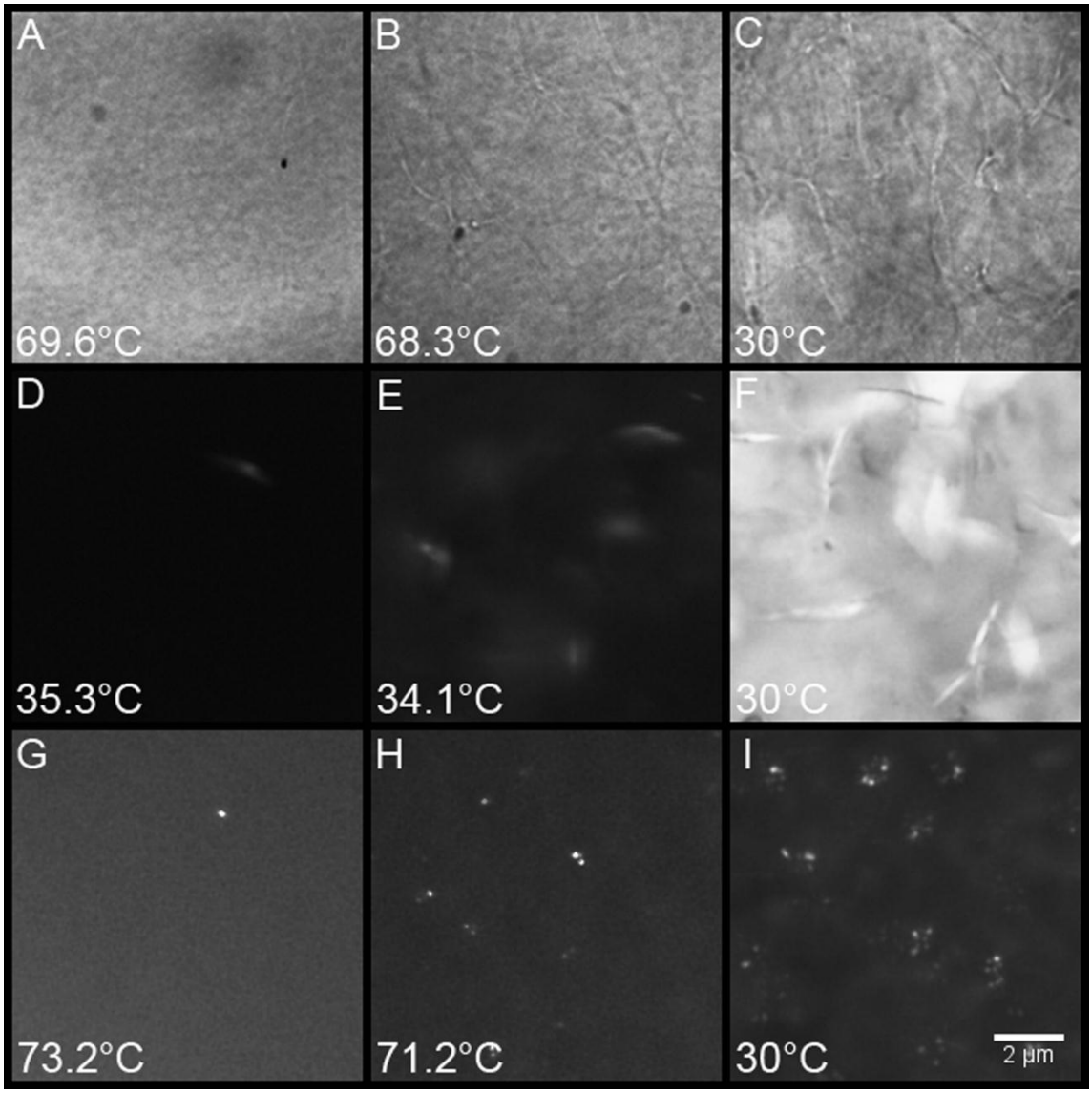

Figure 5.2: Brightfield micrographs of 12HSA (A-C), polarized light micrographs of stearic acid (D-F) and trihydroxystearin (G-I) in mineral oil cooled at 10 °C/min.

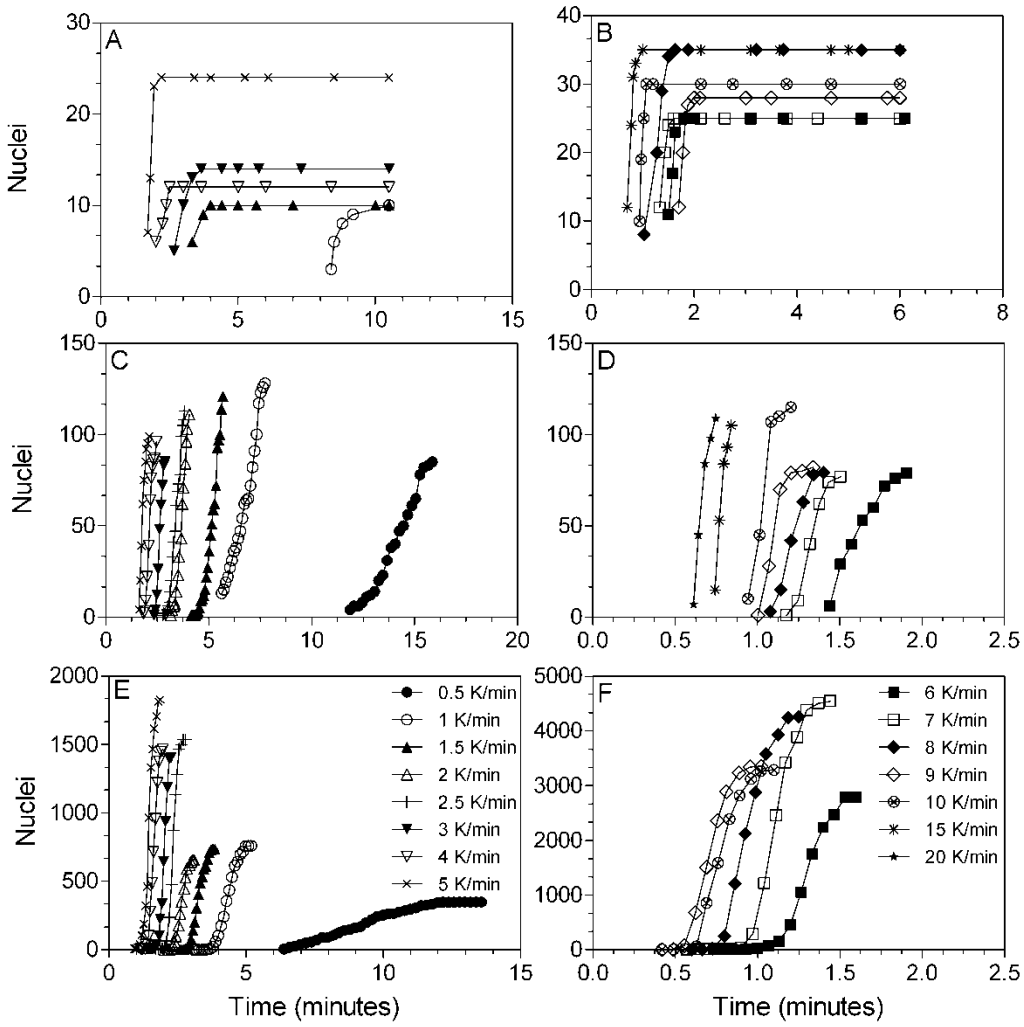

Figure 5.3: Number of nuclei on the corresponding light micrographs as the sample is non-isothermally cooled for 2.5% 12HSA (A-B), 2.5% stearic acid (C-D) and 2.5% trihydroxystearin (E-F) in mineral oil where time zero is the maximum cooling temperature.

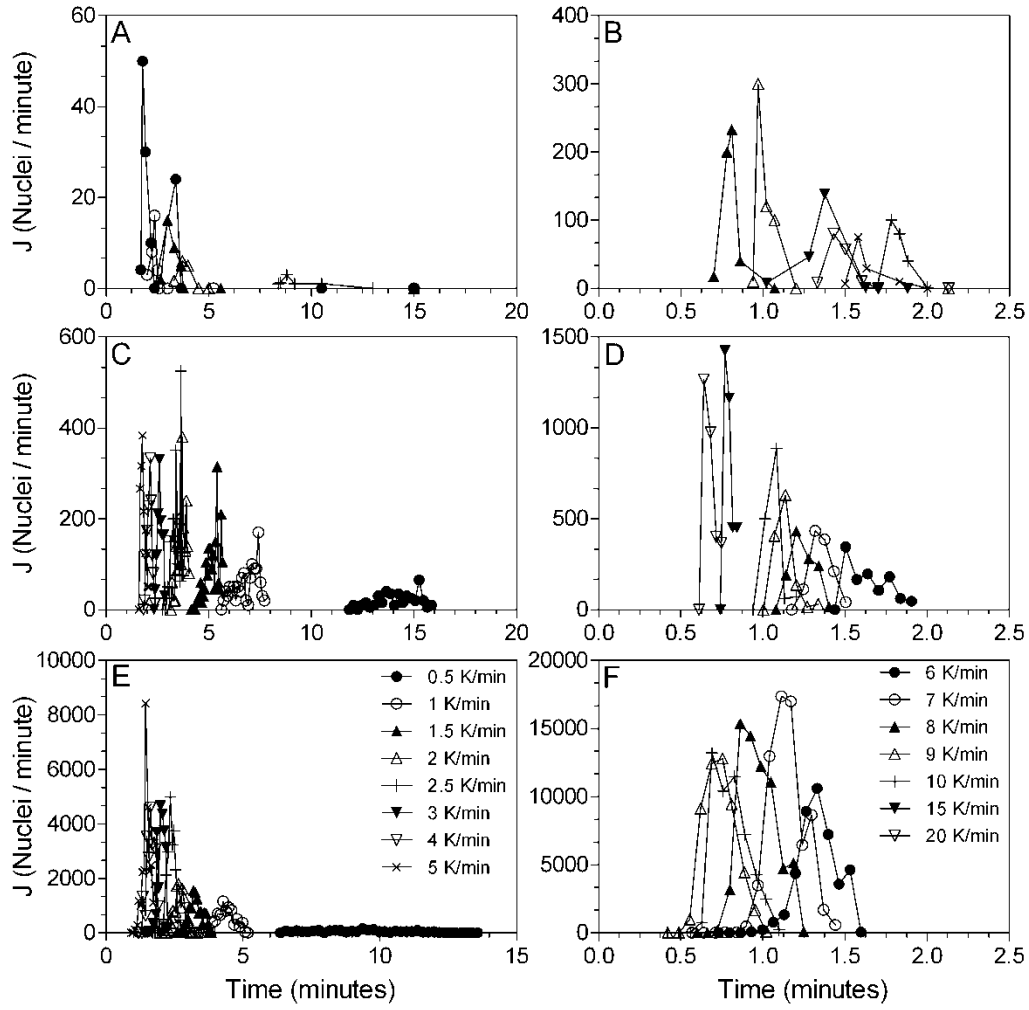

Figure 5.4: The rate of nucleation determined from the derivative of Figure 3 for 2.5% 12HSA (A-B), 2.5% stearic acid (C-D) and 2.5% trihydroxystearin (E-F).

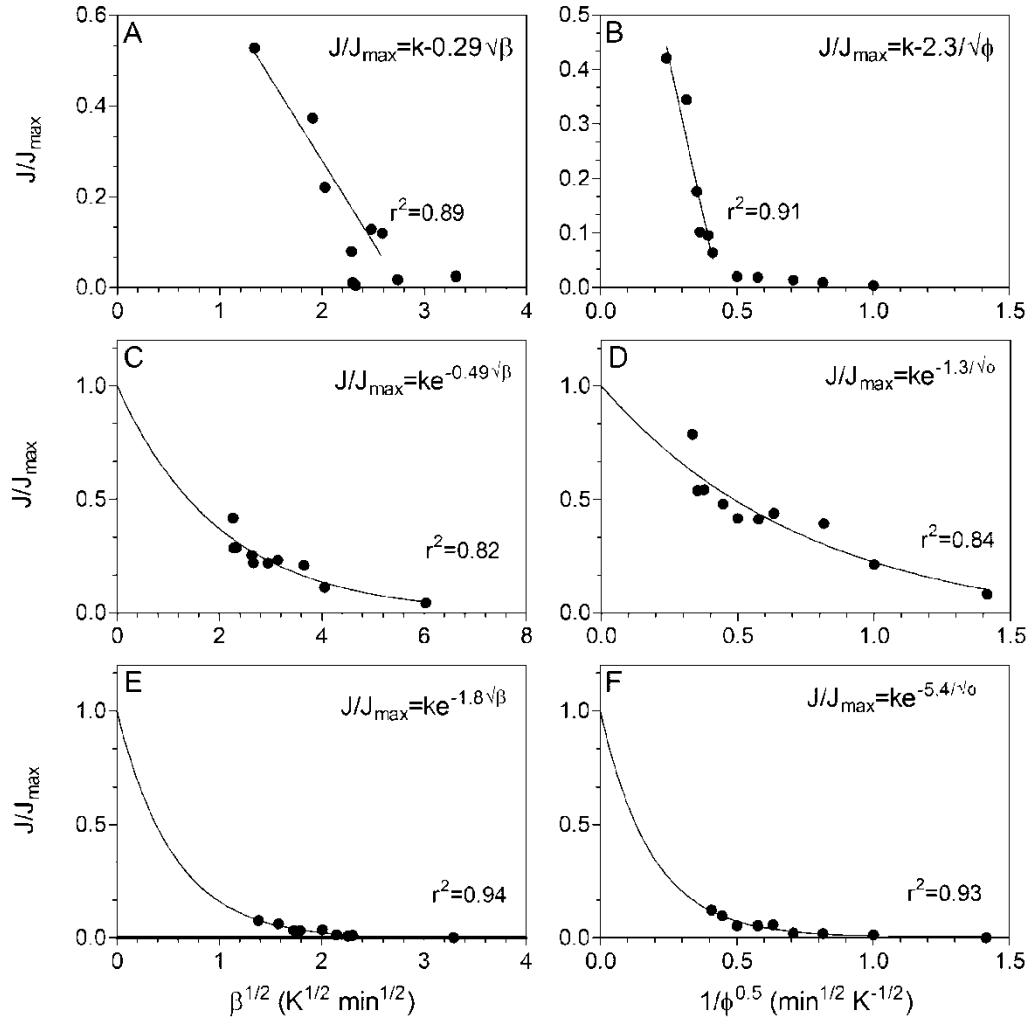

Figure 5.5: The dependence of the relative nucleation rate (J/J_{max}) verses the supercooling-time exposure (β) for 2.5% 12HSA (A), 2.5% stearic acid (C) and 2.5% trihydroxystearin (E) in mineral oil, and the dependence of the relative nucleation rate (J/J_{max}) versus the cooling rate for 2.5% 12HSA (B), 2.5% stearic acid (D) and 2.5% trihydroxystearin (F) in mineral oil.

force for phase separation increased facilitating the formation of crystal embryos.

It is speculated that the difference in polarity between triglyceride and the mineral oil would be minimal thus the chemical potential difference between the two compounds is small and hence the activation energy would be the largest. Therefore, a large thermodynamic force (*i.e.*, supercooling) is required before nucleation may occur. Trihydroxystearin is slightly more polar compared to triglycerides and thus a higher chemical potential is observed resulting in a lower activation energy. Stearic acid and 12HSA have the smallest activation due to their increased polarity compared to trihydroxystearin. Yet, differences in polarity do not explain the fact that stearic acid has a lower activation energy compared to 12HSA. The observed differences in activation energy between stearic acid and 12HSA could also be affected by factors which may limit adsorption of molecules to the crystal interface such as surface diffusion, step adsorption and incorporation into kink sites.

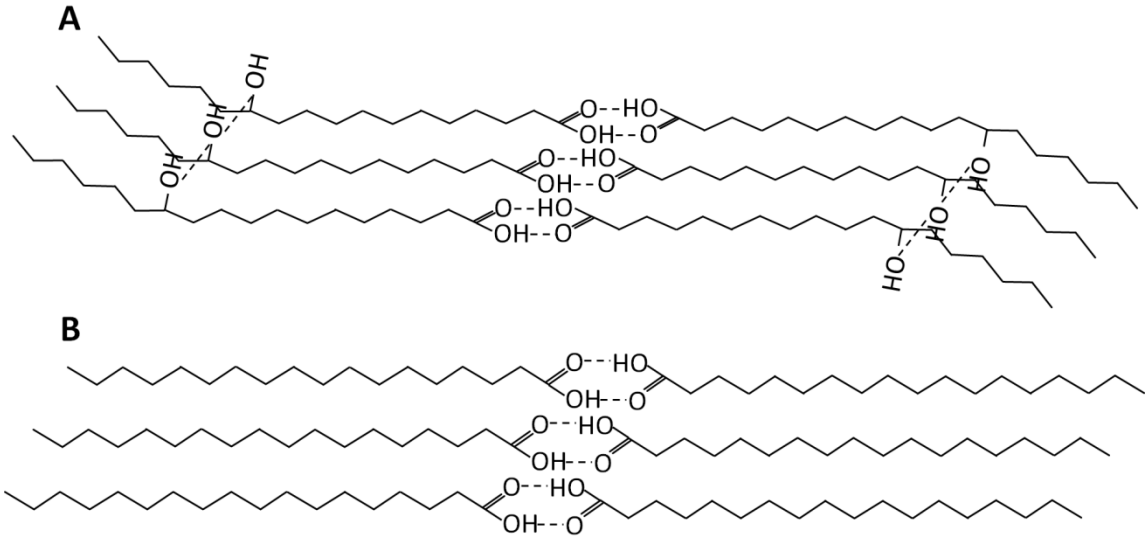

Figure 5.6: Molecular dimers of 12-hydroxystearic acid (A) and stearic acid (B).

Stearic acid and 12HSA are both 18 carbon fatty acids; however, 12HSA has a hydroxyl group at position 12. The polar carboxylic acid head groups on 12HSA and stearic acid facilitates phase separation. Therefore, as stearic acid and 12HSA cool, the molecules form dimers effectively shielding the polar carboxylic acid group away from the apolar solvent interface (Figure 5.6). When carboxylic acid groups are hidden from the crystal-solvent interface, the interfacial tension at the forming interface is reduced. For 12HSA, the formation of the dimer does not minimize the contact between the polar hydroxyl groups and solvent which results in a higher interfacial tension compared to stearic acid (Figure 5.6A). The increased polarity of 12HSA should translate to a lower nucleation activation energy but this was not observed which is explained by the crystal conformation. Therefore, a specific interaction by the nucleating molecules is required to account for the higher activation energy observed for 12HSA compared to stearic acid. The specific interaction accounts for how molecules in the nucleus are arranged (*i.e.*, if the crystal surface is devoid of polar groups). For 12HSA, the resulting dimer shields the carboxylic acid head group but leaves the hydroxyl groups exposed at the surface. The limitation in the ability of 12HSA to exclude the polar regions of the molecule from the crystal-solvent interface results in a higher interfacial tension and thus a higher activation energy.

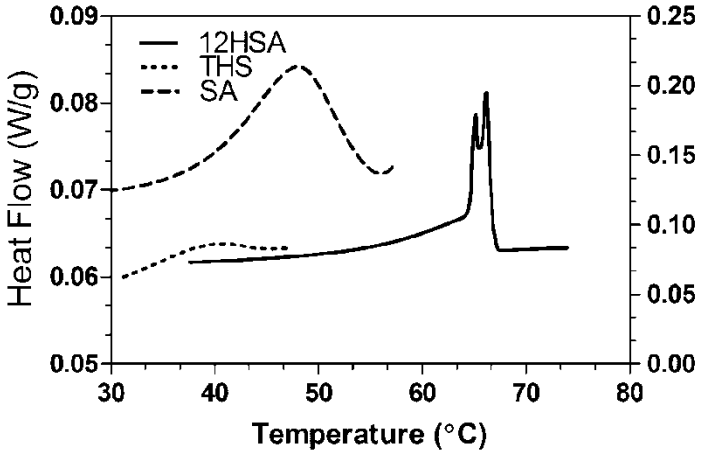

Figure 5.7: The enthalpy for crystallization of 12-hydroxystearic acid (12HSA) (left axis), stearic acid (SA) (right axis) and trihydroxystearin (THS) (right axis).

Table 5.1: Demixing entropies and the enthalpy associated with the phase transition for 12-hydroxystearic acid (12HSA), stearic acid (SA) and trihydroxystearin (THS).

	12HSA	SA	THS
Demixing Entropy ($J\ mol^{-1}\ K^{-1}$)	2.86 ± 0.08	2.50 ± 0.16	0.68 ± 0.09
Enthalpy ($J\ mol^{-1}$)	970.4 ± 28.54	771.4 ± 51.29	216.1 ± 29.78

Formation of a crystal embryo is facilitated by enthalpic forces driven by the formation of non-covalent bonds between molecules that result in a release of heat. This driving force is countered by entropic forces attributed to the demixing encountered during nucleation. The enthalpy of the phase change was measured using DSC (Figure 5.7) which allowed for the entropy to be calculated (Table 5.1). Stearic acid, 12HSA and trihydroxystearin had enthalpies of 771.4 ± 51.29 J/mol, 970.4 ± 28.54 J/mol and 216.1 ± 29.78 J/mol; respectively. These three values were calculated to be statistically different with a 95% confidence interval. The trend in the enthalpic forces did not correlate with the trend observed in the activation energy. Trihydroxystearin has the lowest enthalpy per mol because the non-covalent interactions formed during nucleation are predominately van der Waals interactions and minimal hydrogen bonding associated with the hydroxyl groups. Stearic acid forms van der Waals interactions as well as hydrogen bonds between the carboxylic acid head groups. Finally, 12HSA has the highest enthalpy because in addition to the non-covalent interactions formed by stearic acid, 12HSA has the additional hydrogen bonding associated with the hydroxyl groups.

From the enthalpies obtained, the entropy for demixing was calculated. When the sample reaches its crystallization temperature, the Gibbs energy is zero, therefore it is possible to calculate the demixing entropy associated with the system:

$$\Delta G = \Delta H - T\Delta S \qquad \text{(eq. 5.8)}$$

where ΔG is the Gibbs energy, ΔH is the enthalpy for the phase transition, T is the crystallization temperature in kelvin and ΔS is the entropy. The entropy is associated with the phase separation in the formation of a crystal embryo. This value indicates the loss of entropy, which is thermodynamically unfavourable. The entropies for stearic acid, 12HSA and trihydroxystearin were calculated to be 2.50 ± 0.16 J mol^{-1} K^{-1}, 2.86 ± 0.08 J mol^{-1} K^{-1}, and 0.68 ± 0.09 J mol^{-1} K^{-1}; respectively. Using a 95% confidence interval, stearic acid and 12HSA was calculated to not be statistically different while both were statistically different than trihydroxystearin. The entropy associative with the phase transition follows a similar trend as the activation energy associated with nucleation. This trend suggests that the phase separation process and the associated crystal-interfacial tension are central to the formation of a stable nucleus. This suggests that the ability of the molecules to arrange in such a fashion to minimize the polar groups from the interface between the apolar solvent is central in the formation of a stable nuclei which supports the concept of a molecular shape factor.

5.5 Conclusion

The nature of the activation energy for nucleation under non-isothermal cooling conditions was determined for 12HSA, stearic acid, trihydroxystearin and triglycerides. It was found that the relative nucleation rate of trihydroxystearin and stearic acid were inversely proportional to the supercooling-time trajectory parameter. The activation energies for stearic acid, 12HSA, trihydroxystearin and triglycerides were 2.12 kJ/mol, 5.40 kJ/mol (Rogers & Marangoni, 2009), 7.87 kJ/mol and 24.8 kJ/mol (Marangoni *et al.*, 2006b); respectively.

The relative polarity, in part, influences the activation energy for nucleation such that a more polar compound results in a lower activation energy. The difference in molecular polarity explains the differences in the activation energies between triglycerides and trihydroxystearin compared to stearic acid and 12HSA. However, the difference in activation energy between stearic acid and 12HSA cannot be attributed solely to the polarity and a specific interaction by the nucleating molecules must be accounted. The specific interaction is the molecular arrangement within the crystal and the ability of the crystal to facilitate the depletion of polar groups from the apolar solvent

at the crystal-solvent interface. The importance of the specific interaction may be observed by examining the entropy of demixing for these compounds which were 2.50 ± 0.16 J mol^{-1} K^{-1}, 2.86 ± 0.08 J mol^{-1} K^{-1}, and 0.68 ± 0.09 J mol^{-1} K^{-1} for stearic acid, 12HSA and trihydroxystearin; respectively. Hence, the absolute entropy values correspond well to the activation energies for these molecules.

5.6 Study 3 in context of this thesis

Study 3 completed the last objective stated in the introduction by investigating how molecular structure affects the activation energy for nucleation. It was found that the polarity along with the specific interaction governs the nucleation behaviour. Because this statistical method was able to differentiate macroscopic from microscopic phase separation, this method can also be applied to study how changes in the chain length or the addition of other side groups will affect the activation energy for nucleation in other molecules.

6. General Discussion

Crystallization occurs *via* the following steps: supercooling, nucleation and crystal growth. Understanding the crystallization process under non-isothermal cooling conditions is paramount to the industry. Three studies were done to investigate the crystallization process under non-isothermal cooling conditions. In the first study, the modified Avrami model was experimentally validated to model crystallization under non-isothermal cooling conditions. In study 2, the crystallization behaviour under non-isothermal cooling conditions for one-dimensional 12HSA fibres was investigated to determine the mechanism for crystallographic mismatches which causes branching. In study 3, the activation energy for nucleation was determined under non-isothermal cooling conditions to investigate how molecular structure affects the ability for stearic acid containing molecules to nucleate.

Three molecules were selected due to difference in dimensionality of crystal growth. 12HSA crystallized into one-dimensional fibres, stearic acid crystallized into two-dimensional platelets and trihydroxystearin crystallized into three-dimensional spherulites. In all three studies, it was observed that under non-isothermal cooling conditions these systems did not change in their crystal morphology as a function of the cooling rate (Figure 5.1 and 5.2). Study 3 revealed that the number of nucleation sites increases as a function of cooling rate (Figure 5.3). Because these systems do not change in their crystal morphology under varying non-isothermal cooling conditions, they were suitable candidates as model systems for studying crystallization and nucleation under non-isothermal cooling conditions.

The Avrami model is commonly used to model crystallization in fat crystal networks (Ahmadi *et al.*, 2008; Boodhoo *et al.*, 2009; Liu *et al.*, 2010; Marangoni,

2005a; Metin & Hartel, 1998). The Avrami model cannot be applied directly to model crystallization under non-isothermal cooling conditions because it was originally developed to study crystallization isothermally (Avrami, 1939, 1940, 1941). Therefore, a modified Avrami model was required to model crystallization under non-isothermal cooling conditions (Rogers & Marangoni, 2008, 2009). In study 1, the modified Avrami model was used to empirically model the crystallization process under non-isothermal cooling conditions. The experimental validation of the model was done by comparing the experimentally fitted parameters to the collected data. The model is valid under non-isothermal cooling conditions because the fitted parameters of the modified Avrami model such as the maximum phase change, induction time and Avrami exponent, corresponded well with the collected data. Study 1 indicated that the modified Avrami model requires the technique used to measure the crystallization process has to be purely a measure of the change in phase volume.

This model can be applied to materials of various dimensionalities of crystal growth. The apparent rate constants obtained from this model reveal the crystallization kinetics under non-isothermal cooling conditions. It is interesting to note that despite PLM not being the most accurate experimental method for modelling crystallization processes under non-isothermal cooling conditions, PLM and FT-IR both indicate two modes of crystal growth apparent by the change in slope for the two regimes separated by the 5-7 °C/min range of cooling rates for all three model systems (Figure 3.9). The apparent rate constants may be used to characterize the crystal growth process by differentiating modes of crystal growths as a function of the cooling rate.

In study 2, the mechanism for branching in 12HSA fibres was investigated. At low cooling rates, long one-dimensional fibres with little branching was formed. A highly branched network of 12HSA fibres are formed at cooling rates above 5 °C/min. Branching occurs in 12HSA due to crystallographic mismatches which is the imperfect incorporation of molecules into the crystal lattice. In 12HSA, hydrogen bonding of the hydroxyl groups are responsible for longitudinal growth while fibre thickness are due to the dimerization of carboxylic acids (Suzuki *et al.*, 2003). When the crystallization process was modelled to the modified Avrami model, it was found that while the rate of

hydrogen bonding increased linearly as a function of cooling rate, the rate of carboxylic acid dimerization plateaued above cooling rates of 5 °C/min. By using FT-IR analysis and the apparent rate constant of the modified Avrami model, it was possible to determine that the inability for carboxylic acid to dimerize at high cooling rates caused crystallographic mismatches in 12HSA. The use of the modified Avrami model and FT-IR analysis may become a useful tool to the industry to determine the molecular interactions which may affect the crystallization process under non-isothermal cooling conditions.

In study 3, nucleation, which initiates the crystallization process, was studied by determining the activation energies for 12HSA, stearic acid, and trihydroxystearin under non-isothermal cooling conditions. The activation energy for stearic acid, 12HSA, trihydroxystearin and triglycerides were 1.52 kJ/mol, 5.40 kJ/mol (Rogers & Marangoni, 2009), 7.87 kJ/mol and 24.80 kJ/mol (Marangoni *et al.*, 2006b); respectively. The activation energy for nucleation depended in part on the polarity of the molecule with respect to the polarity of the solvent, such that a more polar compound resulted in a lower activation energy. Due to the difference in activation energy between stearic acid and 12HSA, the polarity of the molecule cannot be the sole reason for the observed activation energy. Therefore, a specific interaction was introduced to account for the ability of the molecule to hide its polar groups from the forming interface. When a molecule, such as 12HSA, cannot shield its polar regions from the forming interface, the interfacial tension and the activation energy increases.

This study demonstrates how molecular structure dictates the nucleation behaviour of the system. The statistical method used was capable of determining whether a molecule underwent microscopic or macroscopic phase separation. Microscopic phase separation occurs when the critical radius for a nucleus is small, whereas macroscopic phase separation requires a significantly larger critical radius to form a nucleus (Weiss & Terech, 2006). 12HSA microscopically phase separates because hydrogen bonding formed between molecules makes it easier to form a nucleus whereas triglycerides require a larger number of molecules held together by attractive forces to form a nucleus (Rogers & Marangoni, 2008). It was observed that 12HSA

undergoes microscopic phase separation whereas trihydroxystearin and stearic acid underwent macroscopic phase separation. The statistical method used in study 3 is capable of characterizing the nucleation behaviour by determining whether a molecule undergoes macroscopic or microscopic phase separation and its associated activation energy for nucleation.

7. Conclusions

The purpose of this body of work was to gain a better understanding of crystallization under non-isothermal cooling conditions. Understanding crystallization under these conditions is vital for the industry which utilizes them. The crystallization process under non-isothermal cooling conditions was investigated by fulfilling three objectives. The first was to experimentally validate the use of the modified Avrami model to characterize crystallization under non-isothermal cooling. The second investigated the nature of crystallographic mismatches in 12HSA fibres. The third was to understand how molecular structure affects the activation energy for nucleation under non-isothermal cooling conditions.

In study 1, the modified Avrami model was experimentally validated as a model which may be applied non-isothermally to model the crystallization process. The Avrami model is robust due to the multiple parameters that may be used to verify its efficacy. Parameters such as induction time, maximum phase change and Avrami exponent was used in the experimental validation of this model. From the four techniques used, it was found that FT-IR was the best method to characterize crystallization under non-isothermal cooling conditions using the modified Avrami model. FT-IR was a superior method as the data collected correlated well with the values determined using the model. Furthermore, FT-IR was capable in accurately determining the Avrami exponent whereas other methods were capable of accurately determining the dimensionality of crystal growth but not the mode of nucleation. Therefore, kinetic data can be obtained from the apparent rate constants of FT-IR data modelled to the modified Avrami model. The kinetic data obtained, gave insights to the kinetics of phase transition under non-isothermal cooling conditions.

In Study 2, the nature of crystallographic mismatches was investigated. Crystallographic mismatches occur when molecules are incorporated into the crystal

lattice in an imperfect manner resulting in the branching of 12HSA fibres. It was found that by using FT-IR analysis and the modified Avrami model, the inability for carboxylic acid to effectively dimerize at cooling rates above 5 °C/min caused crystallographic mismatches in 12HSA fibres. This study demonstrates how methods such as FT-IR may be useful in determine the rate limiting interactions which may affect the crystallization process of a system.

In study 3, the activation energy for nucleation was determined using a statistical approach. It was found that the relative polarity plays an important role in the activation energy for nucleation. For molecules that have a large polarity relative to the solvent, the activation energy required to nucleate is greatly reduced. Yet, polarity does not fully explain the results as 12HSA had a higher activation energy than stearic acid. This required the introduction of a specific interaction to explain for the observed difference. The specific interaction describes the ability for a molecule to hide its polar groups from the forming nucleus-solvent interface. When the polar groups are not shielded from the interface, the chemical potential across the barrier increases which also increases the activation energy. The inability for 12HSA to hide its polar groups from the forming interface caused it to have a higher activation energy than stearic acid.

The nucleation and crystallization behaviour of materials crystallizing under non-isothermal cooling conditions was studied using 12HSA, stearic acid and trihydroxystearin. The modified Avrami model was experimentally validated as a technique to characterize crystallization under non-isothermal cooling conditions. Using FT-IR analysis and the modified Avrami model, it was determined that crystallographic mismatches in 12HSA were due to the inefficient dimerization of carboxylic acid dimers under higher cooling rates. Nucleation behaviour was studied by determining the activation energy for nucleation for 12HSA, stearic acid and trihydroxystearin. The activation energy for stearic acid, 12HSA, trihydroxystearin and triglycerides were 1.52 kJ/mol, 5.40 kJ/mol (Rogers & Marangoni, 2009), 7.87 kJ/mol and 24.80 kJ/mol (Marangoni *et al.*, 2006b); respectively. The activation energy was in part due to the polarity of the molecule relative to the solvent. Therefore an increase in the polarity of a molecule led to a decrease in the activation energy. Stearic acid was found to have a

lower activation energy than 12HSA which was counter-intuitive, yet this was explained by the introduction of the concept of a specific interaction among the crystallizing molecules. The specific interaction represents the ability for a molecule to shield its polar groups away from the forming interface of a nucleus. Without effective shielding, the chemical potential at the interface increases which also cause an increase in the activation energy.

This body of work experimentally validated the modified Avrami model to characterize crystallization under non-isothermal cooling conditions. This can be applied in industrial settings where crystallization undergoes non-isothermal cooling conditions. The modified Avrami model in conjunction with FT-IR could be used to identify limiting molecular reactions during the crystallization process. Finally, the statistical method used in study 3 can be used to identify whether microscopic or macroscopic phase separation occurs and determine the activation energy for nucleation for a system.

8. References

Ahmadi, L., Wright, A. J., & Marangoni, A. G. (2008). Chemical and enzymatic interesterification of tristearin/triolein-rich blends: Chemical composition, solid fat content and thermal properties. *European Journal of Lipid Science and Technology, 110*(11), 1014-1024.

Ajayaghosh, A., Praveen, V. K., & Vijayakumar, C. (2008). Organogels as scaffolds for excitation energy transfer and light harvesting. *Chemical Society Reviews, 37*(1), 109-122.

Aro, A., Jauhiainen, M., Partanen, R., Salminen, I., & Mutanen, M. (1997). Stearic acid, trans fatty acids, and dairy fat: Effects on serum and lipoprotein lipids, apolipoproteins, lipoprotein(a), and lipid transfer proteins in healthy subjects. *American Journal of Clinical Nutrition, 65*(5), 1419-1426.

Avrami, M. (1939). Kinetics of phase change. I General theory. *The Journal of Chemical Physics, 7*(12), 1103-1112.

Avrami, M. (1940). Kinetics of Phase Change. II Transformation Time Relations for Random Distribution of Nuclei. *The Journal of Chemical Physics, 8*(2), 212-224.

Avrami, M. (1941). Kinetics of Phase Change. III Granulation, Phase Change and Microstructure. . *J. Chem. Phys, 9*(2), 177-184.

Berger, K. G., Jewell, G. G., & Pollitt, R. J. M. (1979). Oils and fats. In J. G. Vaughan (Ed.), *Food Microscopy*, (pp. 445-497). London: Academic Press.

Bianco, A., Kostarelos, K., & Prato, M. (2005). Applications of carbon nanotubes in drug delivery. *Current Opinion in Chemical Biology, 9*(6), 674-679.

Boner, K. D. (1958). Manufacture and Use of Lubricating Greases. *Gostoptekhizdat*.

Boodhoo, M. V., Bouzidi, L., & Narine, S. S. (2009). The binary phase behavior of 1, 3-dipalmitoyl-2-stearoyl-sn-glycerol and 1, 2-dipalmitoyl-3-stearoyl-sn-glycerol. *Chemistry and Physics of Lipids, 160*(1), 11-32.

Bot, A., & Agterof, W. G. M. (2006). Structuring of edible oils by mixtures of gamma-oryzanol with beta-sitosterol or related phytosterols. *Journal of the American Oil Chemists Society, 83*(6), 513-521.

Bot, A., den Adel, R., & Roijers, E. C. (2008). Fibrils of gamma-Oryzanol plus beta-Sitosterol in Edible Oil Organogels. *Journal of the American Oil Chemists Society, 85*(12), 1127-1134.

Bouzidi, L., & Narine, S. S. (2010). Evidence of Critical Cooling Rates in the Nonisothermal Crystallization of Triacylglycerols: A Case for the Existence and Selection of Growth Modes of a Lipid Crystal Network. *Langmuir, 26*(6), 4311-4319.

Bruchez, M., Moronne, M., Gin, P., Weiss, S., & Alivisatos, A. P. (1998). Semiconductor nanocrystals as fluorescent biological labels. *Science, 281*(5385), 2013-2016.

Campos, R. (2005). Experimental Methodology. In A. G. Marangoni (Ed.), *Fat Crystal Networks* (pp. 267-348). New York, NY: Marcel Dekker.

Campos, R., Ollivon, M., & Marangoni, A. G. (2010). Molecular Composition Dynamics and Structure of Cocoa Butter. *Crystal Growth & Design, 10*(1), 205-217.

Chaleepa, K., Szepes, A., & Ulrich, J. (2010). Effect of additives on isothermal crystallization kinetics and physical characteristics of coconut oil. *Chemistry and Physics of Lipids, 163*(4-5), 390-396.

Chapman, D. (1962). The Polymorphism of Glycerides. *Chemical Reviews, 62*(5), 433-456.

Cornel, J., & Mazzotti, M. (2009). Estimating Crystal Growth Rates Using in situ ATR-FTIR and Raman Spectroscopy in a Calibration-Free Manner. *Industrial & Engineering Chemistry Research, 48*(23), 10740-10745.

Daniel, J., & Rajasekharan, R. (2003). Organogelation of plant oils and hydrocarbons by long-chain saturated FA, fatty alcohols, wax esters, and dicarboxylic acids. *Journal of the American Oil Chemists' Society, 80*(5), 417-421.

deMan, J. M., & deMan, L. (2002). Texture of Fats. In A. G. Marangoni & S. S. Narine (Eds.), *Physical Properties of Lipids*, (pp. 191-218). New York: Marcel Dekker, Inc.

Duncan, R. (2007). Designing polymer conjugates as lysosomotropic nanomedicines. *Biochemical Society Transactions, 35*, 56-60.

Elliger, C. A., Dunlap, C. E., & Guadagni, D. G. (1972). Thickening Action of Hydroxystearates in Peanut Butter. *Journal of the American Oil Chemists Society, 49*(9), 536-537.

Fernandez-Moya, V., Martinez-Force, E., & Garces, R. (2005). Oils from improved high stearic acid sunflower seeds. *Journal of Agricultural and Food Chemistry, 53*(13), 5326-5330.

Fuhrhop, J. H., Schnieder, P., Rosenberg, J., & Boekema, E. (1987). The Chiral Bilayer Effect Stabilizes Micellar Fibers. *Journal of the American Chemical Society, 109*(11), 3387-3390.

Gandolfo, F. G., Bot, A., & Floter, E. (2004). Structuring of edible oils by long-chain FA, fatty alcohols, and their mixtures. *Journal of the American Oil Chemists Society, 81*(1), 1-6.

Gioielli, L. A., Simoes, I. S., & Rodrigues, J. N. (2003). Crystal morphology and interactions of binary and ternary mixtures of hydrogenated fats. *Journal of Food Engineering, 57*(4), 347-355.

Grompone, M. A., Correa-Cabrera, R., & Irigaray, B. (1999). Differential scanning calorimetry: A modern method for characterization of fatty materials. *Ingenieria Quimica*(16), 45-55.

Hackeng, C. M., de Bruijn, L. A. M., Douw, C. M., & van Dieijen-Visser, M. P. (2000). Presence of birefringent, maltese-cross-appearing spherules in synovial fluid in a case of acute monoarthritis. *Clinical Chemistry, 46*(11), 1861-1863.

Hanabusa, K., Miki, T., Taguchi, Y., Koyama, T., & Shirai, H. (1993). 2-Component, small-molecule gelling agents. *Journal of the Chemical Society-Chemical Communications*, (18), 1382-1384.

Hartel, R. W. (2001). *Crystallization in Foods*. Gaithersburg, MD: Aspen Publishers, Inc.

Holland, B. T., Blanford, C. F., Do, T., & Stein, A. (1999). Synthesis of highly ordered, three-dimensional, macroporous structures of amorphous or crystalline inorganic oxides, phosphates, and hybrid composites. *Chemistry of Materials, 11*(3), 795-805.

Hosono, E., Fujihara, S., Honna, I., & Zhou, H. S. (2005). The fabrication of an upright-standing zinc oxide nanosheet for use in dye-sensitized solar cells. *Advanced Materials, 17*(17), 2091-2094.

Hu, J. T., Odom, T. W., & Lieber, C. M. (1999). Chemistry and physics in one dimension: Synthesis and properties of nanowires and nanotubes. *Accounts of Chemical Research, 32*(5), 435-445.

Huang, H., Gu, L. X., & Ozaki, Y. (2006). Non-isothermal crystallization and thermal transitions of a biodegradable, partially hydrolyzed poly(vinyl alcohol). *Polymer, 47*(11), 3935-3945.

Huang, X., & Weiss, R. G. (2007). Molecular organogels of the sodium salt of (R)-12-hydroxystearic acid and their templated syntheses of inorganic oxides. *Tetrahedron, 63*(31), 7375-7385.

Huo, Z., Dai, S., Zhang, C., Kong, F., Fang, X., Guo, L., Liu, W., Hu, L., Pan, X., & Wang, K. (2008). Low Molecular Mass Organogelator Based Gel Electrolyte with Effective Charge Transport Property for Long-Term Stable Quasi-Solid-State Dye-Sensitized Solar Cells. *The Journal of Physical Chemistry B, 112*(41), 12927-12933.

Isomaa, B., Almgren, P., Tuomi, T., Forsen, B., Lahti, K., Nissen, M., Taskinen, M. R., & Groop, L. (2001). Cardiovascular morbidity and mortality associated with the metabolic syndrome. *Diabetes Care, 24*(4), 683-689.

Iwanaga, K., Sumizawa, T., Miyazaki, M., & Kakemi, M. (2010). Characterization of organogel as a novel oral controlled release formulation for lipophilic compounds. *International Journal of Pharmaceutics, 388*(1-2), 123-128.

Jin, J., Song, M., & Pan, F. (2007). A DSC study of effect of carbon nanotubes on crystallisation behaviour of poly(ethylene oxide). *Thermochimica Acta, 456*(1), 25-31.

Johnson, W. (2000). Final report on the safety assessment of Trihydroxystearin. *International Journal of Toxicology, 19*, 89-94.

Kang, L., Liu, X. Y., Sawant, P. D., Ho, P. C., Chan, Y. W., & Chan, S. Y. (2005). SMGA gels for the skin permeation of haloperidol. *Journal of Controlled Release, 106*(1-2), 88-98.

Lam, R., Quaroni, L., Pederson, T., & Rogers, M. A. (2010). A molecular insight into the nature of crystallographic mismatches in self-assembled fibrillar networks under non-isothermal crystallization conditions. *Soft Matter, 6*(2), 404-408.

Lam, R. S. H., & Rogers, M. A. (2010). Experimental Validation of the Modified Avrami Model for Non-Isothermal Crystallization Conditions. *CrystEngComm, 13*(3), 866-875.

Li, D., & Xia, Y. N. (2004). Direct fabrication of composite and ceramic hollow nanofibers by electrospinning. *Nano Letters, 4*(5), 933-938.

Li, J.-L., Wang, R.-Y., Liu, X.-Y., & Pan, H.-H. (2009). Nanoengineering of a Biocompatible Organogel by Thermal Processing. *The Journal of Physical Chemistry B, 113*(15), 5011-5015.

Li, J. L., Liu, X. Y., Wang, R. Y., & Xiong, J. Y. (2005). Architecture of a biocompatible supramolecular material by supersaturation-driven fabrication of its fiber network. *Journal of Physical Chemistry B, 109*(51), 24231-24235.

Liang, G., Yang, Z., Zhang, R., Li, L., Fan, Y., Kuang, Y., Gao, Y., Wang, T., Lu, W. W., & Xu, B. (2009). Supramolecular Hydrogel of a δ-Amino Acid Dipeptide for Controlled Drug Release in Vivoâ€ *Langmuir, 25*(15), 8419-8422.

Lin-Vien, D., Colthup, N. B., Fateley, W. G., & Grasselli, H. G. (1991). *The Handbook of Infrared and Raman Characteristic Frequencies of Organic Molecules*. New York: Academic Press.

Liu, T. Y., Chen, S. Y., Liu, D. M., & Liou, S. C. (2005). On the study of BSA-loaded calcium-deficient hydroxyapatite nano-carriers for controlled drug delivery. *Journal of Controlled Release, 107*(1), 112-121.

Liu, X. Y. (2005). Gelation with Small Molecules: from Formation Mechanism to Nanostructure Architecture. *Top. Curr. Chem., 256*, 1-37.

Liu, X. Y., & Sawant, P. D. (2001). Formation kinetics of fractal nanofiber networks in organogels. *Applied Physics Letters, 79*(21), 3518-3520.

Liu, X. Y., & Sawant, P. D. (2002a). Determination of the fractal characteristic of nanofiber-network formation in supramolecular materials. *Chemphyschem, 3*(4), 374-377.

Liu, X. Y., & Sawant, P. D. (2002b). Mechanism of the formation of self-organized microstructures in soft functional materials. *Advanced Materials, 14*(6), 421-426.

Liu, Y. F., Meng, Z., Zhang, F. Q., Shan, L., & Wang, X. G. (2010). Influence of lipid composition, crystallization behavior and microstructure on hardness of palm oil-based margarines. *European Food Research and Technology, 230*(5), 759-767.

Livesey, G. (2000). The absorption of stearic acid from triacylglycerols: an inquiry and analysis. *Nutrition Research Reviews, 13*(2), 185-214.

Mallia, A. V., George, M., Blair, D. L., & Weiss, R. G. (2009). Robust Organogels from Nitrogen-Containing Derivatives of (R)-12-Hydroxystearic Acid as Gelators: Comparisons with Gels from Stearic Acid Derivatives. *Langmuir, 25*(15), 8615-8625.

Marangoni, A. G. (1998). On the use and misuse of the avrami equation in characterization of the kinetics of fat crystallization. *Journal of the American Oil Chemists Society, 75*(10), 1465-1467.

Marangoni, A. G. (2005a). Crystallization Kinetics. In A. G. Marangoni (Ed.), *Fat Crystal Networks*, (pp. 21-82). New York: Marcel Dekker.

Marangoni, A. G. (2005b). Crystallography. In A. G. Marangoni (Ed.), *Fat Crystal Networks*, (pp. 1-20). New York: Marcel Dekker.

Marangoni, A. G., Aurand, T. C., Martini, S., & Ollivon, M. (2006). A probabilistic approach to model the nonisothermal nucleation of triacylglycerol melts. *Crystal Growth & Design, 6*(5), 1199-1205.

Marangoni, A. G., & McGauley, S. E. (2003). Relationship between crystallization behavior and structure in cocoa butter. *Crystal Growth & Design, 3*(1), 95-108.

Marangoni, A. G., & Tang, D. M. (2008). Modeling the rheological properties of fats: A perspective and recent advances. *Food Biophysics, 3*(2), 113-119.

Marangoni, A. G., Tang, D. M., & Singh, A. P. (2006). Non-isothermal nucleation of triacylglycerol melts. *Chemical Physics Letters, 419*(1-3), 259-264.

Maskaev, A. K., Man'Kovskaya, N. K., Lend'el, I. V., Fedorvskii, V. T., Simurova, E. I., & Terent'eva, V. N. (1971). Preparation of 12-Hydroxystearic Acid, the Raw Material for Plastic Greases. *Chemistry and Technology of Fuels and OIl, 7*(2), 109-112.

McClements, D. J., & Decker, E. A. (2008). Lipids. In S. Damodaran, K. L. Parkin & O. R. Fennema (Eds.), *Fennema's Food Chemistry* 4th ed., (pp. 155-216). Boca Raton, FL: CRC Press.

Meara, M. L. (1980). Problems of fats in food industry. In R. J. Hamilton & A. Bhati (Eds.), *Fats and oils: chemistry and technology*, (pp. 193-213). London: Applied Science.

Metin, S., & Hartel, R. W. (1998). Thermal analysis of isothermal crystallization kinetics in blends of cocoa butter with milk fat or milk fat fractions. *Journal of the American Oil Chemists Society, 75*(11), 1617-1624.

Moghimi, S. M., Hunter, A. C., & Murray, J. C. (2005). Nanomedicine: current status and future prospects. *Faseb Journal, 19*(3), 311-330.

Morales-Rueda, J. A., Dibildox-Alvarado, E., Charo-Alonso, M. A., & Toro-Vazquez, J. F. (2009). Rheological Properties of Candelilla Wax and Dotriacontane Organogels Measured with a True-Gap System. *Journal of the American Oil Chemists Society, 86*(8), 765-772.

Pernetti, M., van Malssen, K. F., Flöter, E., & Bot, A. (2007). Structuring of edible oils by alternatives to crystalline fat. *Current Opinion in Colloid & Interface Science, 12*(4-5), 221-231.

Piorkowska, E., Galeski, A., & Haudin, J. M. (2006). Critical assessment of overall crystallization kinetics theories and predictions. *Progress in Polymer Science, 31*(6), 549-575.

Qian, F., Tao, J., Desikan, S., Hussain, M., & Smith, R. L. (2007). Mechanistic investigation of Pluronic (R) based nano-crystalline drug-polymer solid dispersions. *Pharmaceutical Research, 24*(8), 1551-1560.

Roche, H. M. (2005). Fatty acids and the metabolic syndrome. *Proceedings of the Nutrition Society, 64*(1), 23-29.

Rogers, M. A. (2009). Novel structuring strategies for unsaturated fats - Meeting the zero-trans, zero-saturated fat challenge: A review. *Food Research International, 42*(7), 747-753.

Rogers, M. A., & Marangoni, A. G. (2008). Non-Isothermal Nucleation and Crystallization of 12-Hydroxystearic Acid in Vegetable Oils. *Crystal Growth & Design, 8*(12), 4596-4601.

Rogers, M. A., & Marangoni, A. G. (2009). Solvent-Modulated Nucleation and Crystallization Kinetics of 12-Hydroxystearic Acid: A Nonisothermal Approach. *Langmuir, 25*(15), 8556-8566.

Rogers, M. A., Wright, A. J., & Marangoni, A. G. (2008a). Crystalline stability of self-assembled fibrillar networks of 12-hydroxystearic acid in edible oils. *Food Research International, 41*(10), 1026-1034.

Rogers, M. A., Wright, A. J., & Marangoni, A. G. (2008b). Engineering the oil binding capacity and crystallinity of self-assembled fibrillar networks of 12-hydroxystearic acid in edible oils. *Soft Matter, 4*(7), 1483-1490.

Rogers, M. A., Wright, A. J., & Marangoni, A. G. (2009a). Nanostructuring fiber morphology and solvent inclusions in 12-hydroxystearic acid/canola oil organogels. *Current Opinion in Colloid & Interface Science, 14*(1), 33-42.

Rogers, M. A., Wright, A. J., & Marangoni, A. G. (2009b). Oil organogels: the fat of the future? *Soft Matter, 5*(8), 1594-1596.

Rosenflanz, A., Frey, M., Endres, B., Anderson, T., Richards, E., & Schardt, C. (2004). Bulk glasses and ultrahard nanoceramics based on alumina and rare-earth oxides. *Nature, 430*(7001), 761-764.

Ross, R. (1999). Mechanisms of disease - Atherosclerosis - An inflammatory disease. *New England Journal of Medicine, 340*(2), 115-126.

Rousset, P. (2002). Modeling Crystallization Kinetics of Triacylglycerols. In A. G. Marangoni & S. S. Narine (Eds.), *Physical Properties of Lipids,* (pp. 1-36). New York: Marcel Dekker.

Sato, K. (1999). Solidification and phase transformation behaviour of food fats - a review. *Lipid - Fett, 101*(12), 467-474.

Sato, K. (2001). Crystallization behaviour of fats and lipids - a review. *Chemical Engineering Science, 56*(7), 2255-2265.

Sato, K., Ueno, S., & Yano, J. (1999). Molecular interactions and kinetic properties of fats. *Progress in Lipid Research, 38*(1), 91-116.

Schaink, H. M., van Malssen, K. F., Morgado-Alves, S., Kalnin, D., & van der Linden, E. (2007). Crystal network for edible oil organogels: Possibilities and limitations of the fatty acid and fatty alcohol systems. *Food Research International, 40*(9), 1185-1193.

Schwittay, C., Mours, M., & Winter, H. H. (1995). Rheological expression of physical gelation in polymers. *Faraday Discussions, 101*, 93-104.

Sharples, A. (1966). *Introduction to polymer crystallization*. London: Edward Arnold, Ltd.

Singh, R. P., & Heldman, D. R. (2001). *Introduction to Food Engineering* (3 ed.). Oxford, UK: Academic Press.

Smith, K. W., Cain, F. W., & Talbot, G. (2005). Kinetic analysis of nonisothermal differential scanning calorimetry of 1,3-dipalmitoyl-2-oleoylglycerol. *Journal of Agricultural and Food Chemistry, 53*(8), 3031-3040.

Suzuki, M., Nakajima, Y., Yumoto, M., Kimura, M., Shirai, H., & Hanabusa, K. (2003). Effects of hydrogen bonding and van der Waals interactions on organogelation using designed low-molecular-weight gelators and gel formation at room temperature. *Langmuir, 19*(21), 8622-8624.

Swamy, R. S. N., Prasad, P. B. V., & Raju, I. (1985). Growth Micromorphology of stearic-acid crystals. *Crystal Research and Technology, 20*(6), 803-807.

Tachiban, T., & Kambara, H. (1968). Sense of Twist in Fibrous Aggregates from 12-Hydroxystearic Acid and its Alkali Metal Soaps. *Journal of Colloid and Interface Science, 28*(1), 173-174.

Terech, P. (2009). Metastability and Sol Phases: Two Keys for the Future of Molecular Gels? *Langmuir, 25*(15), 8370-8372.

Terech, P., Rodriguez, V., Barnes, J. D., & McKenna, G. B. (1994). Organogels and aerogels of racemic and chiral 12-hydroxyoctadeanoic acid. *Langmuir, 10*(10), 3406-3418.

Terech, P., & Weiss, R. G. (1997). Low Molecular Mass Gelators of Organic Liquids and the Properties of Their Gels. *Chemical Reviews, 97*(8), 3133-3160.

Tiberg, F., & Johnsson, M. (2011). Drug delivery applications of non-lamellar liquid crystalline phases and nanoparticles. *Journal of Drug Delivery Science and Technology, 21*(1), 101-109.

Timms, R. E. (1984). Phase behaviour of fats and their mixtures. *Progress in Lipid Research, 23*(1), 1-38.

Uzu, Y., & Sugiura, T. (1975). Electron-microscope and thermal studies of optically-active 12-hydroxystearic acids in soap formation. *Journal of Colloid and Interface Science, 51*(2), 346-349.

Walstra, P. (2003). *Physical Chemistry of Foods*. New York: Marcel Dekker, Inc.

Wang, B. J., Li, C. Y., Hanzlicek, J., Cheng, S. Z. D., Geil, P. H., Grebowicz, J., & Ho, R. M. (2001). Poly(trimethylene teraphthalate) crystal structure and morphology in different length scales. *Polymer, 42*(16), 7171-7180.

Wang, R., Liu, X.-Y., Xiong, J., & Li, J. (2006). Real-Time Observation of Fiber Network Formation in Molecular Organogel: Supersaturation-Dependent Microstructure and Its Related Rheological Property. *The Journal of Physical Chemistry B, 110*(14), 7275-7280.

Weiss, R. G., & Terech, P. (2006). Introduction. In R. G. Weiss & P. Terech (Eds.), *Molecular Gels: Materials with Self-Assembled Fibrillar Networks*, (pp. 1-13). Dordrecht: Springer.

Winter, H. H. (1999). Soft Polymeric Materials Near the Transition from Liquid to Solid State. *Korea-Australia Rheology Journal, 11*(4), 275-278.

Xu, B. (2009). Gels as Functional Nanomaterials for Biology and Medicine. *Langmuir, 25*(15), 8375-8377.